UNIVERSIDAD DE CONCEPCIÓN
FACULTAD DE CIENCIAS FÍSICAS Y MATEMÁTICAS

EMERGENCE, ENGINEERING, AND CHARACTERIZATION OF NONCLASSICAL STATES OF LIGHT

Por: Mariano Uria Valencia

Tesis presentada a la Facultad de Ciencias Físicas y Matemáticas de la Universidad de Concepción para optar al grado académico de Doctor en Ciencias con Mención en Óptica Cuántica

Agosto 2026
Concepción, Chile

Profesor Guía: Dr. Pablo Andrés Solano Palma
Co-Guía: Dra. Carla Andrea Hermann Avigliano

En memoria de Tita, Lucy y César

Agradecimientos

Hay muchas personas a quienes agradecer en estas líneas, y aunque seguramente no logre expresar todo lo que quisiera, trataré de ser conciso.

En primer lugar, quiero agradecer a mi familia, especialmente a mi madre, Vilma, y a mi hermano, Jorge, quienes son mi motor y la razón por la que me levanto cada mañana para seguir adelante.

En segundo lugar, y no por ello menos importante, quiero agradecer a mis asesores de tesis, Carla Hermann y Pablo Solano, por haber sido un apoyo constante antes y durante el doctorado. Valoro profundamente la confianza que depositaron en mí. Llegaron a mi vida en un momento crucial y, de alguna manera, cayeron del cielo. Gracias a su apoyo y confianza, pude seguir en mi camino ninja de la física. También quisiera agradecer a Rodrigo Vicencio, quien fue el nexo que me permitió el tsaheylu y al profesor Aldo Delgado quien también hizo posible toda investigación que haya hecho aquí. También quisiera agradecer a todos los docentes que tuve durante estos años, tanto dentro como fuera de los cursos.

Asimismo, quiero agradecer a los amigos que hice durante esta etapa. A quienes conocí apenas llegué a Chile: Nico, Felipe, Seba, Rodrigo, Toño y Leti; a los miembros de LAMPcito (actualmente ya perdí la cuenta del número de miembros xD) y a los amigos que hice por parte de otros grupos en la institución y fuera de esta, de quienes siempre he recibido una cálida acogida. Todos ellos hicieron que me sintiera uno más en este país que me abrió las puertas y me permitió vivir una etapa muy importante de mi vida.

Finalmente, agradezco a la Agencia Nacional de Investigación y Desarrollo (ANID) y al Millennium Institute for Research in Optics (MIRO) por el financiamiento brindado.

Resumen

Los estados no-clásicos de la luz constituyen un recuros fundamental para las tecnologías cuánticas. Entender como emergen, como pueden ser generados de manera controlada y como pueden ser caracterizados de manera eficiente es aún un desafío central en el área de la óptica cuántica de variable contínua. Esta tesis trata estos aspectos dentro de un marco teórico unificado.

Primeramente estudiamos la emergencia de la no-clasicalidad inducida por un Hamiltoniano no lineal en el número de fotones. Considerando la evolución de estados coherentes bajo esta interacción no-lineal, demostramos la aparición universal de características no Gausianas y caracterizamos los estados cuánticos resultantes a través de medidas de no-clasicalidad complementarias, incluyendo la negatividad de la función de Wigner y la información cuántica de Fisher.

A continuación, nos enfocamos en la generación controlada de estados no-clásicos por medio de un Hamiltoniano tipo Kerr forzado por un campo coherente. En este contexto, evidenciamos la generación determinista de los *photon added coherent states*. Para caracterizar este proceso de caracterización, introducimos la cantidad de número de fotones remanente, la cual identifica la formación de estos estados durante la evolución y a la vez revela sus características no clásicas.

Finalmente, proponemos protocolos de tomografía de estados cuánticos para campos propagantes basados en metasuperficies cuánticas o *espejos cuánticos*, interfaces ópticas cuya reflectividad está controlada por el estado cuántico de un átomo auxiliar. Al explotar la respuesta óptica condicional de estas interfaces luz–materia, los esquemas propuestos permiten reconstruir funciones de onda y distribuciones de cuasiprobabilidad en el espacio de fases mediante mediciones indirectas sobre un sistema auxiliar de variables discretas. Estos protocolos proporcionan alternativas experimentalmente viables a la tomografía homodina convencional y, a la vez, presentan robustez frente a fluctuaciones de fase óptica.

En conjunto, esta tesis establece un enfoque unificado para el estudio de la emergencia, generación y caracterización de estados no clásicos de la luz, combinando la dinámica cuántica no-lineal con nuevos métodos tomográficos para sistemas cuánticos de variables continuas.

Keywords – Quantum metasurfaces, tomography, non-clasicality

Abstract

Nonclassical states of light constitute fundamental resources for quantum technologies. Understanding how they emerge, how they can be generated in a controlled manner, and how they can be efficiently characterized remains a central challenge in continuous-variable quantum optics. This thesis addresses these aspects within a unified theoretical framework.

We first study the emergence of nonclassicality induced by photon-number dependent nonlinear Hamiltonians. Considering the evolution of coherent states under these nonlinear interactions, we demonstrate the universal appearance of non-Gaussian features and characterize the resulting quantum states through complementary measures of nonclassicality, including Wigner-function negativity and quantum Fisher information.

We then focus on the controlled generation of nonclassical states by considering a Kerr Hamiltonian driven by a coherent field. Within this framework, we demonstrate the deterministic generation of photon added coherent states. To characterize this generation process, we introduce the remnant photon number witness, which identifies the formation of these states during the evolution while simultaneously revealing their nonclassical character.

Finally, we develop quantum state tomography protocols for propagating continuous-variable states based on quantum metasurfaces or *quantum mirrors*–optical interfaces with switchable reflectivity controlled by the quantum state of an ancillary atom. Exploiting the conditional optical response of these light-matter interfaces, the proposed schemes enable the reconstruction of wavefunctions and phase-space quasiprobability distributions through indirect measurements on an ancillary discrete-variable system. These protocols provide experimentally feasible alternatives to conventional homodyne tomography while exhibiting robustness against optical phase fluctuations.

Overall, this thesis establishes a unified approach to the emergence, generation, and characterization of nonclassical states of light, combining nonlinear quantum dynamics with novel tomographic methods for continuous-variable quantum systems.

Keywords – Quantum metasurfaces, tomography, non-clasicality

Contents

List of Figures

Chapter 1

Introduction

1.1 Quantum Technologies

The ability to prepare, manipulate, and measure quantum systems has transformed quantum mechanics from a fundamental physical theory into the basis of emerging quantum technologies. By exploiting uniquely quantum phenomena, such as superposition and entanglement, these technologies promise capabilities beyond those achievable with classical devices in computing, communication, sensing, and simulation [1, 2, 3, 4, 5, 6, 7].

Several physical platforms are currently being explored to realize these technologies, including superconducting circuits, trapped ions, neutral atoms, solid-state defects, and photonic systems. Among these, photonic systems and light-matter interfaces play a particularly important role owing to the low decoherence of photons, the breakthrough in optical technologies, and their natural compatibility with long-distance quantum communication. They also enable the coherent transfer of quantum information between stationary and flying qubits, making them fundamental building blocks for quantum networks and distributed quantum computing.

Within photonic quantum technologies, quantum information can be encoded using either discrete-variable (DV) or continuous-variable (CV) approaches. DV protocols employ finite-dimensional Hilbert spaces, such as the polarization or path of single photons, whereas CV protocols exploit the infinite-dimensional Hilbert space of bosonic modes, typically through the quadratures of the electromagnetic field. Continuous-variable systems offer several attractive features, including deterministic Gaussian state preparation and operations, compatibility with integrated photonic architectures, and hardware-efficient implementations of bosonic quantum error correction [8, 9, 10, 11, 12]. As a result, they have emerged as a leading framework for quantum communication [8, 9], quantum metrology [13, 14, 15], and fault-tolerant quantum information processing.

The performance of photonic CV quantum technologies ultimately relies on the preparation, manipulation, and characterization of suitable quantum states of light. Among these, nonclassical states constitute essential resources because they exhibit statistical and phase-space properties that cannot be reproduced by classical mixtures of coherent states, including quantum fluctuations and phase-space structures, which enable capabilities beyond those achievable with classical optical fields. Understanding how such states emerge from light-matter interactions, how they can be engineered, and how they can be efficiently characterized, therefore, remains a central challenge in modern quantum optics.

This thesis addresses these challenges through three complementary contributions. First, it explores the universal emergence of nonclassicality from coherent states under nonlinear evolution. It then develops a protocol for generating multi-photon added coherent states in driven Kerr resonators. Finally, it introduces a family of quantum mirror-based protocols for CV quantum state tomography, enabling the efficient reconstruction of propagating quantum states of light. Together, these contributions establish a unified framework for understanding, engineering, and characterizing nonclassical states of light in CV quantum technologies.

1.2 Nonclassical States of Light

1.2.1 Optical classicality and nonclassicality

In classical optics, improving the precision of a measurement requires increasing the energy of the probing field [13, 16], leading to the standard quantum limit. Quantum mechanics fundamentally changes this paradigm: suitably prepared quantum states of light can surpass this classical scaling and, in principle, approach the Heisenberg limit. This quantum enhancement underlies applications ranging from quantum metrology to communication and information processing, making nonclassical states of light indispensable resources for modern quantum technologies.

To understand what distinguishes a nonclassical optical state, it is first necessary to establish the notion of optical classicality. A classical electromagnetic field is characterized by its spatial and temporal mode structure, including its frequency, wavevector, polarization, and spatial profile, together with its field amplitude. Once a single optical mode is selected, these degrees of freedom are fixed, and the amplitude is fully described by the complex number

$$\alpha = \frac{1}{\sqrt{2}}(X + iP), \tag{1.2.1}$$

where X and P are the two field quadratures. In the phase space representation, the state of this classical mode is therefore associated with a well-defined point (X, P), whose position can, in principle, be determined with arbitrary precision.

The quantum description replaces these phase-space variables by the quadrature operators

$$\hat{X} = \frac{\hat{a} + \hat{a}^\dagger}{\sqrt{2}}, \qquad \hat{P} = \frac{\hat{a} - \hat{a}^\dagger}{i\sqrt{2}}, \tag{1.2.2}$$

which satisfy the canonical commutation relation

$$[\hat{X}, \hat{P}] = i. \tag{1.2.3}$$

Consequently, the Heisenberg uncertainty principle imposes the bound

$$\Delta X \, \Delta P \geq \frac{1}{2}, \tag{1.2.4}$$

preventing any quantum state from being localized at a single point in phase space. Instead, every quantum state necessarily occupies a finite phase-space area determined by its quantum fluctuations.

The quantum states that most closely resemble classical electromagnetic fields are therefore those occupying the minimum area allowed by the uncertainty principle while distributing the fluctuations equally between both quadratures,

$$\Delta X = \Delta P = \frac{1}{\sqrt{2}}. \tag{1.2.5}$$

The unique pure states satisfying these conditions are the coherent states introduced by Glauber [17, 18]. They are defined as the eigenstates of the annihilation operator,

$$\hat{a}\,|\alpha\rangle = \alpha\,|\alpha\rangle\,, \tag{1.2.6}$$

where the eigenvalue α coincides with the classical complex field amplitude and $|\alpha|^2$ represents its number of photons.

Coherent states possess several properties that support them as the closest quantum analog to classical light. Besides minimizing the uncertainty relation, they preserve their shape under harmonic evolution, their expectation values follow the classical equations of motion, and they exhibit Poissonian photon-number statistics,

$$p_n = e^{-|\alpha|^2}\frac{|\alpha|^{2n}}{n!}. \tag{1.2.7}$$

Moreover, coherent states provide an excellent approximation to the output field of a laser operating sufficiently above threshold [19], where stimulated emission dominates over spontaneous emission.

Up to this point, only pure states have been considered. Since coherent states constitute the unique pure states with the strongest classical correspondence, a classical mixed state is naturally defined as a statistical mixture of coherent states,

$$\hat{\rho} = \int p(\alpha)\,|\alpha\rangle\langle\alpha|\;d^2\alpha, \tag{1.2.8}$$

where $p(\alpha)$ is a normalized, non-negative probability density. Such states admit a straightforward classical interpretation: the optical field is prepared in the coherent state $|\alpha\rangle$ with probability $p(\alpha)$.

Coherent states form an overcomplete basis of the Hilbert space. Consequently, every density operator can be expanded in the same form,

$$\hat{\rho} = \int P(\alpha)\,|\alpha\rangle\langle\alpha|\;d^2\alpha, \tag{1.2.9}$$

where $P(\alpha)$ is the Glauber–Sudarshan P quasiprobability distribution [17, 20]. In contrast to the classical probability density $p(\alpha)$, the function $P(\alpha)$ is not required to be positive or even regular. It may become negative or more singular than a Dirac delta distribution [18].

This observation leads to the Glauber–Sudarshan criterion of nonclassicality: a quantum state is regarded as classical if its P function is a well-behaved positive probability distribution, whereas states whose P function fails to satisfy these conditions are classified as nonclassical. Owing to its necessary and sufficient character, this criterion provides the fundamental definition of nonclassicality, while the various definitions discussed in the next subsection can be understood as particular manifestations of it.

1.2.2 Characterization of nonclassical states

The Glauber–Sudarshan representation provides a clear method to determine whether a state is classical or not. However, reconstructing the P function in practice is a major experimental challenge due to its highly singular nature. This limitation has motivated the development of numerous criteria and quantitative measures that identify or quantify nonclassicality through experimentally measurable observables or mathematically well-behaved state functionals.

Mandel Q parameter

One of the earliest quantitative signatures of nonclassicality is provided by the photon-number statistics. We recall that a coherent state exhibits a Poissonian photon-number distribution,

$$p_n = e^{-|\alpha|^2} \frac{|\alpha|^{2n}}{n!}, \tag{1.2.10}$$

for which

$$(\Delta n)^2 = \langle \hat{n} \rangle. \tag{1.2.11}$$

For an arbitrary classical state, namely a statistical mixture of coherent states as in Eq. 1.2.8, it can be shown that

$$(\Delta n)^2 \geq \langle \hat{n} \rangle. \tag{1.2.12}$$

This motivates the definition of Mandel's parameter [21],

$$Q = \frac{(\Delta n)^2}{\langle \hat{n} \rangle} - 1. \tag{1.2.13}$$

States with

$$Q < 0 \tag{1.2.14}$$

possess sub-Poissonian statistics and are necessarily nonclassical. Conversely, $Q > 0$ does not imply classicality, since many nonclassical states, such as squeezed states, exhibit super-Poissonian photon statistics.

Nonclassical Distance

An alternative approach to quantifying nonclassicality is based on the geometric distance between a quantum state and the set of classical states. Given a suitable distance measure $d(\rho, \sigma)$ between two density operators, the corresponding nonclassical distance measurement is defined as [22]

$$d_{\mathrm{NC}}(\rho) = \inf_{\sigma \in \mathcal{C}} d(\rho, \sigma), \tag{1.2.15}$$

where $\mathcal{C}$ denotes the set of classical states,

$$\mathcal{C} = \left\{ \rho \;\middle|\; \rho = \int d^2\alpha \, P(\alpha) \, |\alpha\rangle\langle\alpha| \, , \; P(\alpha) \geq 0 \right\}. \tag{1.2.16}$$

This construction assigns to each quantum state the minimum distance to the classical set, thereby providing a quantitative measure of its nonclassicality.

The first proposal used the trace distance, defined through the trace norm

$$\|A\|_1 = \mathrm{Tr}\sqrt{A^\dagger A}, \tag{1.2.17}$$

leading to

$$d_{\mathrm{NC}}^{\mathrm{Tr}}(\rho) = \inf_{\sigma \in \mathcal{C}} \|\rho - \sigma\|_1. \tag{1.2.18}$$

The trace distance possesses a clear operational interpretation, as it quantifies the maximum probability of distinguishing two quantum states by an optimal measurement. More generally, other distance measures may also be employed, such as the Hilbert–Schmidt distance [23]

$$d_{\mathrm{HS}}(\rho, \sigma) = \sqrt{\mathrm{Tr}[(\rho - \sigma)^2]}, \tag{1.2.19}$$

or the Bures distance [23],

$$d_{\mathrm{B}}(\rho,\sigma)=\sqrt{2-2F(\rho,\sigma)}, \tag{1.2.20}$$

where $F(\rho,\sigma)=\mathrm{Tr}\left\{\sqrt{\rho}\,\sigma\sqrt{\rho}\right\}$ is the quantum fidelity.

Different choices of the distance function lead to different geometric measures of nonclassicality. The trace and Bures distances are contractive under completely positive trace preserving maps, meaning that they cannot increase under physical operations. Consequently, they induce monotonic measures of nonclassicality. By contrast, the Hilbert–Schmidt distance is not contractive and therefore does not, in general, define a monotone nonclassicality measure.

Nonclassical Depth

A particularly intuitive measure of nonclassicality is based on the amount of Gaussian noise that must be added to the Glauber–Sudarshan P function to transform it into a non-negative probability distribution. To this end, consider the family of Cahill–Glauber quasiprobability distributions,

$$W(\alpha;s), \qquad -1\leq s\leq 1, \tag{1.2.21}$$

defined as the Fourier transform of the s-ordered characteristic function

$$\chi(\beta;s)=\mathrm{Tr}[\rho D(\beta)]\,e^{s|\beta|^2/2}, \tag{1.2.22}$$

where $D(\beta)$ is the displacement operator and the parameter s continuously interpolates between the Glauber–Sudarshan P function ($s=1$) to the Husimi Q function ($s=-1$).

Equivalently, the family $W(\alpha;s)$ can be obtained by progressively smoothing the P function by making a convolution with a Gaussian distribution,

$$W(\alpha;s)=\frac{2}{\pi(1-s)}\int d^2\beta\,\exp\left[-\frac{2|\alpha-\beta|^2}{1-s}\right]P(\beta), \tag{1.2.23}$$

the shorter the value of s, the stronger and more aggressive the smoothing.

The nonclassical depth is then defined as

$$\tau = \frac{1 - s_0}{2}, \tag{1.2.24}$$

where s_0 is the largest value of s for which the corresponding quasiprobability distribution $W(\alpha; s)$ becomes a positive distribution. Equivalently, τ quantifies the minimum amount of Gaussian smoothing required to remove all signatures of nonclassicality from the Glauber–Sudarshan P function. Consequently, classical states satisfy $\tau = 0$, while states requiring the maximum amount of smoothing possess $\tau = 1$.

Entanglement Potential

An operational characterization of nonclassicality is provided by the entanglement potential [24]. The central idea is that only nonclassical states can generate entanglement through linear optics [25].

Consider an arbitrary single-mode state ρ entering one input port of a balanced beam splitter, while the second input is in the vacuum state. The output state is

$$\rho_{\text{out}} = U_{\text{BS}} \left(\rho \otimes |0\rangle\langle 0|\right) U_{\text{BS}}^{\dagger}. \tag{1.2.25}$$

The entanglement potential is then defined as the amount of bipartite entanglement generated in the output,

$$EP(\rho) = E(\rho_{\text{out}}), \tag{1.2.26}$$

where E denotes any suitable measurement of entanglement, such as *logarithmic negativity* or *relative entropy* of entanglement. Classical states satisfy

$$EP(\rho) = 0, \tag{1.2.27}$$

whereas every nonclassical state necessarily produces entanglement after the beam splitter. This establishes a direct operational connection between nonclassicality and quantum entanglement.

Negative Volume of Quasiprobability Distributions

The negativity of phase-space quasiprobability distributions constitutes one of the most direct signatures of nonclassicality. Since classical states are characterized by a non-negative Glauber–Sudarshan P function, the appearance of negative regions in a quasiprobability distribution immediately reveals the absence of a classical probabilistic description.

For the Wigner function, this signature is commonly quantified through the negative volume introduced by Kenfack and Życzkowski [26],

$$\delta_W = \int |W(\alpha)| \, d^2\alpha - 1, \tag{1.2.28}$$

which vanishes whenever the Wigner function is everywhere non-negative and increases with the total volume of its negative regions.

This quantity can be directly computed from experimentally reconstructed Wigner functions. However, it provides only a sufficient criterion for nonclassicality, since many nonclassical states like squeezed states possess a non-negative Wigner function. Consequently, it is complemented by operational measures such as the metrological power, which quantify the metrological advantage enabled by nonclassical states.

Requirements for nonclassicality measures

The existence of numerous nonclassicality measures naturally raises the question of what properties a satisfactory quantifier should possess. Although different measures capture different manifestations of nonclassicality, an ideal measure is generally expected to satisfy a number of fundamental requirements.

Mathematically, a nonclassicality measure is a map

$$\mathcal{N} : \mathcal{S}(H) \to [0, \infty), \tag{1.2.29}$$

that assigns a non-negative real number to each quantum state ρ, where $\mathcal{S}(H)$ denotes the set of density operators on the optical Hilbert space H.

The first requirement is *faithfulness*. A measure must identify exactly the set of classical states,

$$\mathcal{N}(\rho) = 0 \quad \Longleftrightarrow \quad \rho \in \mathcal{C}, \tag{1.2.30}$$

while assigning a strictly positive value to every nonclassical state. In this way, the measure remains fully consistent with the Glauber–Sudarshan criterion of negativity.

The second desirable property is *monotonicity.* Let $\mathcal{O}$ be the set of operations that preserve classicality, namely physical transformations that map every classical state onto another classical state. A valid nonclassicality measure should not increase under the action of any operation $\Phi \in \mathcal{O}$, that is,

$$\mathcal{N}(\Phi(\rho)) \leq \mathcal{N}(\rho). \tag{1.2.31}$$

This requirement reflects the physically intuitive principle that operations incapable of generating nonclassicality should not increase the amount of nonclassicality present in a quantum state. The precise characterization of the set $\mathcal{O}$ depends on the theoretical framework adopted.

A third desirable property is *convexity.* Since classical randomness cannot create quantum resources, a convex combination of quantum states should not increase the amount of nonclassicality,

$$\mathcal{N}\left(\sum_i p_i\rho_i\right) \leq \sum_i p_i\mathcal{N}(\rho_i), \qquad \sum_i p_i = 1. \tag{1.2.32}$$

This condition guarantees that classical uncertainty is not mistakenly interpreted as genuine quantum nonclassicality.

> *An ideal measure should possess a clear operational interpretation. Beyond merely identifying nonclassical states, it should quantify a physical advantage that can be exploited in quantum-information tasks.*

Recent developments have established close connections between nonclassicality, quantum coherence, entanglement generation, and quantum metrology, leading to operational measures such as the entanglement potential, coherence-based monotones, and the metrological power of nonclassical states.

Although no single measure simultaneously optimizes all these properties, the numerous quantifiers proposed in the literature can be broadly classified according to the physical quantities they employ. The most prominent families are based on photon-number statistics, geometric distances from the set of classical states, phase-space quasiprobability distributions, and operational quantities associated with quantum-information protocols. Rather than competing definitions, these approaches provide complementary perspectives on the same underlying property: the impossibility of representing the optical field as a classical statistical mixture of coherent states.

1.2.3 Families of nonclassical states

Fock States

Fock, or photon-number, states constitute the most fundamental family of nonclassical states and form a complete orthonormal basis for the Hilbert space of a single bosonic mode. They are defined as the eigenstates of the number operator,

$$\hat{n}\,|n\rangle = \hat{a}^{\dagger}\hat{a}\,|n\rangle = n\,|n\rangle\,, \qquad n = 0, 1, 2, \ldots, \tag{1.2.33}$$

and can be generated from the vacuum through repeated application of the creation operator,

$$|n\rangle = \frac{(\hat{a}^{\dagger})^n}{\sqrt{n!}}\,|0\rangle\,. \tag{1.2.34}$$

Unlike coherent states, Fock states possess a well-defined energy but completely undefined optical phase, leading to a vanishing field expectation value,

$$\langle n|\hat{a}|n\rangle = 0. \tag{1.2.35}$$

Except for the vacuum state, all Fock states are intrinsically nonclassical. Their Glauber–Sudarshan P function is highly singular, while their Wigner function exhibits oscillations and negative regions in phase space for $n \geq 1$, providing a direct manifestation of their nonclassical nature.

Squeezed States

Squeezed states are minimum-uncertainty states in which the quantum fluctuations are redistributed between the two field quadratures while preserving the Heisenberg uncertainty relation,

$$\Delta X\, \Delta P \geq \frac{1}{2}. \tag{1.2.36}$$

They are generated by the squeezing operator

$$\hat{S}(\xi) = \exp\left[\frac{1}{2}\left(\xi^* \hat{a}^2 - \xi \hat{a}^{\dagger 2}\right)\right], \tag{1.2.37}$$

where $\xi = re^{i\phi}$ is the squeezing parameter. Acting on the vacuum, this operator produces the squeezed vacuum state,

$$|\xi\rangle = \hat{S}(\xi)|0\rangle. \tag{1.2.38}$$

Unlike coherent states, squeezed states reduce the noise of one quadrature below the vacuum level at the expense of increased fluctuations in the conjugate quadrature,

$$(\Delta X)^2 < \frac{1}{2}, \tag{1.2.39}$$

while remaining minimum-uncertainty states. Although their Wigner function is Gaussian and everywhere positive, their Glauber–Sudarshan P function is highly singular, establishing them as genuinely nonclassical states. Owing to their reduced quantum noise, squeezed states constitute essential resources for continuous-variable quantum information, quantum communication, and quantum-enhanced metrology [27].

Schrödinger Cat States

Schrödinger cat states are coherent superpositions of two coherent states with opposite phases, and constitute one of the most representative examples of quantum superposition at the mesoscopic scale. They are defined as

$$|\mathcal{C}_\pm\rangle = \mathcal{N}_\pm \left(|\alpha\rangle \pm |-\alpha\rangle\right), \tag{1.2.40}$$

where $\mathcal{N}_\pm$ is a normalization constant given by

$$\mathcal{N}_{\pm} = \left[2\left(1 \pm e^{-2|\alpha|^2}\right)\right]^{-1/2}. \tag{1.2.41}$$

The states $|\mathcal{C}_+\rangle$ and $|\mathcal{C}_-\rangle$ correspond to the even and odd Schrödinger cat states, respectively, since they contain only even or odd photon-number components in their Fock-state expansion. Their Wigner functions exhibit pronounced interference fringes with negative regions in phase space, providing a direct signature of quantum coherence between the two coherent-state components.

Schrödinger cat states can be generated through nonlinear optical interactions, cavity quantum electrodynamics, circuit QED, or conditional photon subtraction from squeezed states. Owing to their robustness against certain loss mechanisms and their non-Gaussian character, they have become valuable resources for bosonic quantum error correction, continuous-variable quantum computation, and quantum-enhanced metrology.

Gottesman–Kitaev–Preskill States

The Gottesman–Kitaev–Preskill (GKP) states constitute one of the most remarkable families of nonclassical states owing to their ability to encode a logical qubit into a single bosonic mode while protecting it against small displacement errors in phase space. Unlike coherent or squeezed states, GKP states consist of periodic superpositions of infinitely squeezed states arranged on a lattice in phase space. Ideally, the logical basis states can be written as

$$|0_L\rangle \propto \sum_{s=-\infty}^{\infty} |X = 2s\sqrt{\pi}\rangle, \tag{1.2.42}$$

$$|1_L\rangle \propto \sum_{s=-\infty}^{\infty} |X = (2s+1)\sqrt{\pi}\rangle, \tag{1.2.43}$$

where $|X\rangle$ denotes the eigenstate of the position quadrature. Equivalent representations can be constructed in the momentum basis, leading to a lattice structure in both quadratures.

Ideal GKP states are unphysical because they require infinite squeezing and therefore infinite energy. Practical realizations rely on finite-energy approximations, in which each peak acquires a finite width and the overall lattice is modulated by a Gaussian envelope. Despite these approximations, GKP states retain their error-correcting capabilities provided the squeezing is sufficiently large.

The highly oscillatory phase-space structure of GKP states gives rise to strongly non-Gaussian Wigner functions with multiple negative regions, reflecting their intrinsically nonclassical character. Their lattice symmetry allows small displacement errors to be detected and corrected through syndrome measurements, making them one of the leading bosonic encodings for fault-tolerant quantum computation.

The preparation of approximate GKP states remains experimentally challenging, requiring a combination of squeezing, nonlinear interactions, and conditional measurements. Nevertheless, remarkable progress has recently been achieved in trapped-ion systems, superconducting microwave cavities, and photonic platforms, establishing GKP states as a central resource for continuous-variable quantum information processing.

Binomial States

Binomial states constitute a finite-dimensional family of nonclassical states that continuously interpolate between number states and coherent states. Introduced by Stoler *et al.* [28], they are defined as finite superpositions of Fock states,

$$|N,p\rangle = \sum_{n=0}^{N} \left[\binom{N}{n} p^n (1-p)^{N-n} \right]^{1/2} |n\rangle, \tag{1.2.44}$$

where N is a positive integer and $0 \leq p \leq 1$. The photon-number distribution therefore follows a binomial law, with mean photon number

$$\langle \hat{n} \rangle = Np, \tag{1.2.45}$$

and variance

$$(\Delta n)^2 = Np(1-p). \tag{1.2.46}$$

Depending on the values of N and p, binomial states interpolate between several important families of quantum states. In the limit $p \to 1$, they reduce to the Fock state $|N\rangle$, whereas for $N \to \infty$ with $Np = |\alpha|^2$ fixed, they converge to the coherent state $|\alpha\rangle$. This interpolation makes them a useful framework for investigating the transition between classical and nonclassical optical fields.

More recently, generalized binomial states have found renewed interest through their connection with bosonic quantum error correction [29, 30]. In particular, the binomial code encodes a logical qubit into finite superpositions of Fock states chosen to suppress photon-loss, photon-gain, and dephasing errors up to a prescribed order. Unlike cat codes, which rely on coherent-state superpositions, binomial codes employ finite photon-number support, making them particularly attractive for implementations in superconducting microwave cavities and other cavity-QED platforms. These developments have established binomial states as an important resource for fault-tolerant bosonic quantum information processing.

The families of states discussed above represent some of the most prominent examples of nonclassical states employed in continuous-variable quantum technologies. Their diverse statistical and phase-space properties enable applications ranging from quantum-enhanced metrology to fault-tolerant quantum computation. Chapter 3 focuses on the generation of one particular family of nonclassical states, namely photon added coherent states, using driven Kerr resonators.

1.3 Outline of the thesis

This thesis is organized into five chapters. Following the present introduction, the remaining chapters develop a unified perspective on the emergence, engineering, and characterization of nonclassical states of light through light–matter interactions.

Chapter 2 establishes the theoretical framework for the light–matter interactions and nonlinear quantum dynamics considered throughout the thesis. It begins with the quantization of the electromagnetic field and the derivation of the electric dipole interaction. The discussion then introduces the Jaynes–Cummings model and the dispersive regime, showing how effective photon-number-dependent interactions arise from off-resonant light–matter coupling.

Chapter 3 investigates the emergence of nonclassicality from coherent states undergoing nonlinear optical evolution. A theoretical framework is developed to demonstrate that photon-number nonlinearities universally give rise to highly non-Gaussian states while preserving the characteristic Poissonian photon statistics of the initial coherent field. The resulting states are analyzed in terms of their nonclassicality and metrological properties.

Chapter 4 addresses the deterministic engineering of nonclassical states. Specifically, it introduces a protocol for the post-selection-free generation of high fidelity multi-photon added coherent states in a driven Kerr resonator. The chapter also analyzes the robustness of the protocol under realistic dissipation using experimentally accessible circuit-QED parameters.

Chapter 5 focuses on the efficient characterization of continuous-variable states. It presents a family of quantum state tomography protocols based on quantum mirrors, enabling the direct reconstruction of propagating states through measurements performed exclusively on an ancillary atom. These protocols provide access to the wavefunction and a broad class of quasiprobability distributions while overcoming several limitations of conventional homodyne tomography.

Finally, Chapter 6 summarizes the main conclusions of this thesis, discusses the broader implications of the presented results, and outlines several directions for future research.

Publications Underlying the Thesis

The following publications constitute the main research contributions underlying this thesis:

- **Chapter 3**

  Emergence of non-Gaussian coherent states through nonlinear interactions, M. Uria, A. Maldonado-Trapp, C. Hermann-Avigliano, and P. Solano, *Physical Review Research* **5**, 013165 (2023). [31]

- **Chapter 4**

  Post-Selection Free Generation of Multi-Photon Added Coherent States, M. Uria, R. Gutiérrez-Jáuregui, C. Hermann-Avigliano, and P. Solano, arXiv:2606.03167 [quant-ph] (2026), under peer review. [32]

- **Chapter 5**

  Continuous-Variable Quantum State Tomography Enabled by Quantum Mirrors, M. Uria, A. Moya, C. Hermann-Avigliano, P. Solano, and A. Delgado, arXiv:2606.04277 [quant-ph] (2026), under peer review. [33]

Chapter 2

Fundamentals of Light–Matter Interactions

2.1 Quantization of the electromagnetic field

The theoretical foundation of quantum optics is the quantization of the electromagnetic field. This procedure begins from Maxwell's equations in the presence of charge and current densities,

$$\nabla \cdot \mathbf{E} = \frac{\rho}{\epsilon_0}, \qquad \nabla \cdot \mathbf{B} = 0, \tag{2.1.1}$$

$$\nabla \times \mathbf{E} = -\frac{\partial \mathbf{B}}{\partial t}, \qquad \nabla \times \mathbf{B} = \mu_0 \mathbf{J} + \mu_0 \epsilon_0 \frac{\partial \mathbf{E}}{\partial t}. \tag{2.1.2}$$

Introducing the scalar and vector potentials,

$$\mathbf{B} = \nabla \times \mathbf{A}, \qquad \mathbf{E} = -\nabla \Phi - \frac{\partial \mathbf{A}}{\partial t}, \tag{2.1.3}$$

the electromagnetic field exhibits a gauge freedom under transformations that leave the electric and magnetic fields unchanged. Throughout this thesis we adopt the Coulomb gauge,

$$\nabla \cdot \mathbf{A} = 0, \tag{2.1.4}$$

which separates the longitudinal and transverse components of the electromagnetic field. Since our interest is restricted to the quantization of the free electromagnetic field, we consider the absence of charges and currents, $\rho = \mathbf{J} = 0$. In this case, the equation for Φ reduces to

$$\nabla^2\Phi = 0. \tag{2.1.5}$$

Under the usual boundary conditions employed in the quantization procedure, the scalar potential is spatially constant and therefore does not contribute to the electromagnetic fields. Consequently,

$$\mathbf{E} = -\frac{\partial \mathbf{A}}{\partial t}, \qquad \mathbf{B} = \nabla \times \mathbf{A}, \tag{2.1.6}$$

so that the transverse vector potential contains the only independent dynamical degrees of freedom of the free electromagnetic field. Substituting these expressions into Maxwell's equations yields the wave equation

$$\nabla^2\mathbf{A} - \frac{1}{c^2}\frac{\partial^2 \mathbf{A}}{\partial t^2} = 0. \tag{2.1.7}$$

The solutions of this equation form a complete set of orthogonal transverse normal modes. Imposing periodic boundary conditions within a square volume V, the classical vector potential can be expanded as

$$\mathbf{A}(\mathbf{r}, t) = \sum_{\mathbf{k},\lambda} q_{\mathbf{k},\lambda}(t)\, \boldsymbol{\epsilon}_{\mathbf{k},\lambda} e^{i\mathbf{k}\cdot\mathbf{r}}, \tag{2.1.8}$$

where $\mathbf{k}$ is the wave vector, $\lambda = 1, 2$ labels the two transverse polarizations, and

$$\mathbf{k} \cdot \boldsymbol{\epsilon}_{\mathbf{k},\lambda} = 0. \tag{2.1.9}$$

Substituting this expansion into the classical field Hamiltonian,

$$H = \frac{1}{2}\int d^3r \left(\epsilon_0\mathbf{E}^2 + \frac{1}{\mu_0}\mathbf{B}^2\right), \tag{2.1.10}$$

one finds that the electromagnetic field is equivalent to an infinite collection of independent harmonic oscillators,

$$H = \frac{1}{2}\sum_{\mathbf{k},\lambda}\left(p_{\mathbf{k},\lambda}^2 + \omega_k^2 q_{\mathbf{k},\lambda}^2\right), \tag{2.1.11}$$

where $q_{\mathbf{k},\lambda}$ and $p_{\mathbf{k},\lambda}$ are canonically conjugate variables associated with each normal mode. Canonical quantization promotes these variables to operators satisfying

$$[\hat{q}_{\mathbf{k},\lambda}, \hat{p}_{\mathbf{k}',\lambda'}] = i\hbar\delta_{\mathbf{k},\mathbf{k}'}\delta_{\lambda,\lambda'}. \tag{2.1.12}$$

It is then convenient to introduce the bosonic annihilation and creation operators,

$$\hat{a}_{\mathbf{k},\lambda} = \sqrt{\frac{\omega_k}{2\hbar}}\left(\hat{q}_{\mathbf{k},\lambda} + \frac{i}{\omega_k}\hat{p}_{\mathbf{k},\lambda}\right), \tag{2.1.13}$$

$$\hat{a}^{\dagger}_{\mathbf{k},\lambda} = \sqrt{\frac{\omega_k}{2\hbar}}\left(\hat{q}_{\mathbf{k},\lambda} - \frac{i}{\omega_k}\hat{p}_{\mathbf{k},\lambda}\right), \tag{2.1.14}$$

which satisfy the commutation relations

$$[\hat{a}_{\mathbf{k},\lambda}, \hat{a}^{\dagger}_{\mathbf{k}',\lambda'}] = \delta_{\mathbf{k},\mathbf{k}'}\delta_{\lambda,\lambda'}. \tag{2.1.15}$$

Expressed in terms of these operators, the vector potential becomes

$$\hat{\mathbf{A}}(\mathbf{r}, t) = \sum_{\mathbf{k},\lambda}\sqrt{\frac{\hbar}{2\epsilon_0\omega_k V}}\left[\hat{a}_{\mathbf{k},\lambda}\boldsymbol{\epsilon}_{\mathbf{k},\lambda}e^{i(\mathbf{k}\cdot\mathbf{r}-\omega_k t)} + \hat{a}^{\dagger}_{\mathbf{k},\lambda}\boldsymbol{\epsilon}^{*}_{\mathbf{k},\lambda}e^{-i(\mathbf{k}\cdot\mathbf{r}-\omega_k t)}\right], \tag{2.1.16}$$

from which the electric and magnetic field operators follow directly from Eq. 2.1.6.

The Hamiltonian of the quantized electromagnetic field assumes the familiar diagonal form

$$\hat{H}_F = \sum_{\mathbf{k},\lambda}\hbar\omega_k\left(\hat{a}^{\dagger}_{\mathbf{k},\lambda}\hat{a}_{\mathbf{k},\lambda} + \frac{1}{2}\right), \tag{2.1.17}$$

revealing that each normal mode behaves as an independent quantum harmonic oscillator. The first term corresponds to the energy carried by the photons occupying each mode, while the second term represents the vacuum zero-point energy.

The eigenstates of the field Hamiltonian are the number (Fock) states,

$$|n_{\mathbf{k},\lambda}\rangle = \frac{(\hat{a}^{\dagger}_{\mathbf{k},\lambda})^n}{\sqrt{n!}}|0\rangle, \tag{2.1.18}$$

which satisfy

$$\hat{a}^{\dagger}_{\mathbf{k},\lambda}\hat{a}_{\mathbf{k},\lambda}|n_{\mathbf{k},\lambda}\rangle = n|n_{\mathbf{k},\lambda}\rangle. \tag{2.1.19}$$

The ladder operators act according to

$$\hat{a}_{\mathbf{k},\lambda}|n_{\mathbf{k},\lambda}\rangle = \sqrt{n}\,|n_{\mathbf{k},\lambda} - 1\rangle, \tag{2.1.20}$$

$$\hat{a}^{\dagger}_{\mathbf{k},\lambda}|n_{\mathbf{k},\lambda}\rangle = \sqrt{n+1}\,|n_{\mathbf{k},\lambda} + 1\rangle, \tag{2.1.21}$$

demonstrating that photons are the elementary excitations of the quantized electromagnetic field.

Although the electromagnetic field possesses infinitely many degrees of freedom, many quantum-optical systems involve only a single resonant mode interacting with matter. Under this approximation, the field Hamiltonian reduces to

$$\hat{H}_F = \hbar\omega \left(\hat{a}^{\dagger}\hat{a} + \frac{1}{2} \right), \tag{2.1.22}$$

which will constitute the starting point for the theoretical developments presented throughout this thesis.

2.2 The electric dipole interaction

The interaction between an atom and the electromagnetic field can be introduced through the principle of minimal coupling, according to which the canonical momentum of a particle with charge q and mass m is replaced as

$$\mathbf{p} \to \mathbf{p} - q\mathbf{A}, \tag{2.2.1}$$

leading to the Hamiltonian

$$\hat{H} = \frac{1}{2m}\left[\hat{\mathbf{p}} - q\hat{\mathbf{A}}(\hat{\mathbf{r}})\right]^2 + q\hat{\Phi}(\hat{\mathbf{r}}) + V(\hat{\mathbf{r}}), \tag{2.2.2}$$

where $\hat{\mathbf{A}}$ and $\hat{\Phi}$ are the electromagnetic vector and scalar potentials, $V(\hat{\mathbf{r}})$ denotes the binding potential.

Expanding the kinetic term yields

$$\hat{H} = \frac{\hat{\mathbf{p}}^2}{2m} - \frac{q}{2m}\left[\hat{\mathbf{p}} \cdot \hat{\mathbf{A}} + \hat{\mathbf{A}} \cdot \hat{\mathbf{p}}\right] + \frac{q^2}{2m}\hat{\mathbf{A}}^2 + q\hat{\Phi} + V(\hat{\mathbf{r}}). \tag{2.2.3}$$

In the Coulomb gauge,

$$\nabla \cdot \hat{\mathbf{A}} = 0, \tag{2.2.4}$$

the symmetrized interaction term can be simplified. Indeed,

$$\hat{\mathbf{p}} \cdot \hat{\mathbf{A}} - \hat{\mathbf{A}} \cdot \hat{\mathbf{p}} = -i\hbar\nabla \cdot \hat{\mathbf{A}} = 0, \tag{2.2.5}$$

so that the interaction Hamiltonian becomes

$$\hat{H}_I = -\frac{q}{m}\hat{\mathbf{A}}(\hat{\mathbf{r}}) \cdot \hat{\mathbf{p}} + \frac{q^2}{2m}\hat{\mathbf{A}}^2(\hat{\mathbf{r}}). \tag{2.2.6}$$

Although the minimal-coupling Hamiltonian provides a complete description of light–matter interactions, it is often convenient to express the interaction in terms of the electric field. To establish this connection, we first invoke the electric dipole approximation. For an electromagnetic field with characteristic wavevector $\mathbf{k}$, the spatial dependence of a plane-wave component of the vector potential is of the form

$$\hat{\mathbf{A}}(\mathbf{r}) \propto e^{i\mathbf{k}\cdot\mathbf{r}}. \tag{2.2.7}$$

When the characteristic size of the atom (≈ 0.25nm) is much smaller than the wavelength of the field (≈ 500nm),

$$kr = \frac{2\pi r}{\lambda} \ll 1, \tag{2.2.8}$$

the phase factor varies negligibly across the atomic dimensions. Therefore,

$$e^{i\mathbf{k}\cdot\mathbf{r}} \simeq 1, \tag{2.2.9}$$

and the vector potential may be approximated as spatially uniform over the atom,

$$\hat{\mathbf{A}}(\hat{\mathbf{r}}) \simeq \hat{\mathbf{A}}(\mathbf{0}), \tag{2.2.10}$$

where the origin is taken at the atomic nucleus.

Within this approximation, the minimal-coupling and electric-dipole forms of the interaction are related by a unitary transformation. We introduce

$$\hat{U} = \exp\left[-\frac{i}{\hbar}\hat{\mathbf{d}} \cdot \hat{\mathbf{A}}(\mathbf{0})\right], \tag{2.2.11}$$

where

$$\hat{\mathbf{d}} = q\hat{\mathbf{r}} \tag{2.2.12}$$

is the electric dipole operator. The quantum state is then transformed as

$$|\psi'\rangle = \hat{U}|\psi\rangle. \tag{2.2.13}$$

Since $\hat{U}$ depends on time through the field operator, the transformed state satisfies the Schrödinger equation

$$i\hbar\frac{\partial}{\partial t}|\psi'\rangle = \hat{H}'|\psi'\rangle, \tag{2.2.14}$$

with

$$\hat{H}' = \hat{U}\hat{H}\hat{U}^\dagger + i\hbar\frac{\partial\hat{U}}{\partial t}\hat{U}^\dagger. \tag{2.2.15}$$

The transformation shifts the canonical momentum. Using the Baker–Campbell–Hausdorff expansion and the commutation relation

$$[\hat{r}_i, \hat{p}_j] = i\hbar\delta_{ij}, \tag{2.2.16}$$

we find

$$\begin{aligned}\hat{U}\hat{\mathbf{p}}\hat{U}^\dagger &= \hat{\mathbf{p}} + \left[-\frac{i}{\hbar}q\hat{\mathbf{r}}\cdot\hat{\mathbf{A}}(\mathbf{0}), \hat{\mathbf{p}}\right] \\ &= \hat{\mathbf{p}} + q\hat{\mathbf{A}}(\mathbf{0}).\end{aligned} \tag{2.2.17}$$

Here, higher-order commutators vanish because the atomic position operators commute with the field operators. Consequently, using the dipole approximation,

$$\begin{aligned}\hat{U}\left[\hat{\mathbf{p}} - q\hat{\mathbf{A}}(\hat{\mathbf{r}})\right]\hat{U}^\dagger &\simeq \hat{\mathbf{p}} + q\hat{\mathbf{A}}(\mathbf{0}) - q\hat{\mathbf{A}}(\mathbf{0}) \\ &= \hat{\mathbf{p}}.\end{aligned} \tag{2.2.18}$$

Thus, within the electric dipole approximation, the light–matter coupling is removed from the kinetic-energy term and reappears in the transformed Hamiltonian through the coupling between the atomic dipole and the electromagnetic field.

The coupling to the electric field arises from the transformation of the field part of the Hamiltonian. Equivalently, in the Coulomb gauge, the electric field is related to the vector potential by

$$\hat{\mathbf{E}}(\mathbf{0}) = -\frac{\partial \hat{\mathbf{A}}(\mathbf{0})}{\partial t}. \tag{2.2.19}$$

The time-dependent contribution to the transformed Hamiltonian is therefore

$$\begin{aligned} i\hbar \frac{\partial \hat{U}}{\partial t} \hat{U}^\dagger &= i\hbar \left[-\frac{i}{\hbar} \hat{\mathbf{d}} \cdot \frac{\partial \hat{\mathbf{A}}(\mathbf{0})}{\partial t} \right] \\ &= \hat{\mathbf{d}} \cdot \frac{\partial \hat{\mathbf{A}}(\mathbf{0})}{\partial t} \\ &= -\hat{\mathbf{d}} \cdot \hat{\mathbf{E}}(\mathbf{0}). \end{aligned} \tag{2.2.20}$$

The resulting leading-order interaction is therefore

$$\hat{H}_I = -\hat{\mathbf{d}} \cdot \hat{\mathbf{E}}(\mathbf{0}). \tag{2.2.21}$$

For a two-level atom, the dipole operator takes the form

$$\hat{\mathbf{d}} = \mathbf{d}_{eg} \hat{\sigma}_+ + \mathbf{d}_{ge} \hat{\sigma}_-, \tag{2.2.22}$$

where $\hat{\sigma}_+ = |e\rangle\langle g|$ and $\hat{\sigma}_- = |g\rangle\langle e|$. Likewise, the electric field can be decomposed into its positive- and negative-frequency components,

$$\hat{\mathbf{E}} = \hat{\mathbf{E}}^{(+)} + \hat{\mathbf{E}}^{(-)}, \tag{2.2.23}$$

with

$$\hat{\mathbf{E}}^{(-)} = \left(\hat{\mathbf{E}}^{(+)} \right)^\dagger. \tag{2.2.24}$$

Substituting these expressions into Eq. (2.2.21) yields four interaction processes,

$$\hat{H}_I = -g \left(\hat{\sigma}_+ + \hat{\sigma}_- \right) \cdot \left(\hat{a} + \hat{a}^\dagger \right), \tag{2.2.25}$$

where g denotes the coupling strength. The first two terms describe the resonant exchange of excitations between the atom and the field, whereas the remaining two correspond to the simultaneous creation or annihilation of both excitations. Under appropriate conditions, these counter-rotating terms can be neglected through the rotating-wave approximation, leading to the Jaynes–Cummings Hamiltonian discussed in the following subsection.

2.3 The Jaynes-Cummings model

The interaction Hamiltonian obtained in the previous section,

$$\hat{H}_I = -g\left(\hat{a}\hat{\sigma}_+ + \hat{a}^\dagger\hat{\sigma}_- + \hat{a}^\dagger\hat{\sigma}_+ + \hat{a}\hat{\sigma}_-\right), \tag{2.3.1}$$

contains four distinct interaction processes. To understand their physical relevance, it is convenient to move to the interaction picture considering the free Hamiltonian

$$\hat{H}_0 = \hbar\omega_c\hat{a}^\dagger\hat{a} + \frac{\hbar\omega_q}{2}\hat{\sigma}_z, \tag{2.3.2}$$

where ω_c denotes the cavity frequency and ω_q the atomic transition frequency.

The interaction-picture Hamiltonian is defined as

$$\hat{H}_I(t) = e^{i\hat{H}_0 t/\hbar}\hat{H}_I e^{-i\hat{H}_0 t/\hbar}. \tag{2.3.3}$$

Using the commutation relations

$$[\hat{a}^\dagger\hat{a}, \hat{a}] = -\hat{a}, \tag{2.3.4}$$

$$[\hat{a}^\dagger\hat{a}, \hat{a}^\dagger] = \hat{a}^\dagger, \tag{2.3.5}$$

$$[\hat{\sigma}_z, \hat{\sigma}_\pm] = \pm 2\hat{\sigma}_\pm, \tag{2.3.6}$$

the operators evolve as

$$\hat{a}(t) = \hat{a}e^{-i\omega_c t}, \tag{2.3.7}$$

$$\hat{a}^\dagger(t) = \hat{a}^\dagger e^{i\omega_c t}, \tag{2.3.8}$$

$$\hat{\sigma}_-(t) = \hat{\sigma}_- e^{-i\omega_q t}, \tag{2.3.9}$$

$$\hat{\sigma}_+(t) = \hat{\sigma}_+ e^{i\omega_q t}. \tag{2.3.10}$$

Substituting these expressions into Eq. (2.3.1) yields

$$\hat{H}_I(t) = -g\Big[\hat{a}\hat{\sigma}_+ e^{-i(\omega_c-\omega_q)t} + \hat{a}^\dagger\hat{\sigma}_- e^{i(\omega_c-\omega_q)t} \\ + \hat{a}^\dagger\hat{\sigma}_+ e^{i(\omega_c+\omega_q)t} + \hat{a}\hat{\sigma}_- e^{-i(\omega_c+\omega_q)t}\Big]. \tag{2.3.11}$$

Equation (2.3.11) clearly separates the interaction into two groups of processes.

The first two terms oscillate with detuning

$$\Delta = \omega_q - \omega_c, \tag{2.3.12}$$

and correspond to the exchange of excitations between the atom and the cavity mode. Physically, the process $\hat{a}\hat{\sigma}_+$corresponds to the absorption of a cavity photon accompanied by the excitation of the atom, whereas $\hat{a}^\dagger\hat{\sigma}_-$describes the reverse process, in which the atom de-excites while emitting a photon into the cavity mode. Together, these two terms conserve the total number of excitations.

In contrast, the remaining terms oscillate at the much higher frequency

$$\omega_c + \omega_q, \tag{2.3.13}$$

and describe processes that simultaneously create or annihilate an atomic excitation and a cavity photon. Unlike the other terms, these counter-rotating processes do not conserve the total number of excitations. Under near-resonant conditions, and provided that

$$g \ll \omega_c, \omega_q, \tag{2.3.14}$$

their rapidly oscillating contributions average to zero over the characteristic timescale of the dynamics, a condition that is satisfied in the vast majority of cavity-QED and circuit-QED experiments. Under this rotating-wave approximation, the interaction Hamiltonian simplifies to

$$\hat{H}_I = \hbar g\left(\hat{a}^\dagger\hat{\sigma}_- + \hat{a}\hat{\sigma}_+\right), \tag{2.3.15}$$

and the total Hamiltonian becomes

$$\boxed{\hat{H}_{\mathrm{JC}} = \hbar\omega_c\hat{a}^\dagger\hat{a} + \frac{\hbar\omega_q}{2}\hat{\sigma}_z + \hbar g\left(\hat{a}^\dagger\hat{\sigma}_- + \hat{a}\hat{\sigma}_+\right),} \tag{2.3.16}$$

which is known as the Jaynes–Cummings Hamiltonian [34].

A remarkable property of Eq. (2.3.16) is that it conserves the total number of excitations,

$$\hat{N} = \hat{a}^\dagger \hat{a} + \hat{\sigma}_+ \hat{\sigma}_-, \tag{2.3.17}$$

since

$$[\hat{H}_{\mathrm{JC}}, \hat{N}] = 0. \tag{2.3.18}$$

Consequently, the Hilbert space decomposes into independent two-dimensional excitation manifolds,

$$\{|g, n+1\rangle, |e, n\rangle\}, \tag{2.3.19}$$

within which the Hamiltonian takes the matrix form

$$H_n = \hbar \begin{pmatrix} (n+1)\omega_c - \omega_q/2 & g\sqrt{n+1} \\ g\sqrt{n+1} & n\omega_c + \omega_q/2 \end{pmatrix}. \tag{2.3.20}$$

Diagonalizing this matrix yields the dressed states

$$|+, n\rangle = \cos\theta_n |e, n\rangle + \sin\theta_n |g, n+1\rangle, \tag{2.3.21}$$

$$|-, n\rangle = -\sin\theta_n |e, n\rangle + \cos\theta_n |g, n+1\rangle, \tag{2.3.22}$$

where the mixing angle satisfies

$$\tan(2\theta_n) = \frac{2g\sqrt{n+1}}{\Delta}. \tag{2.3.23}$$

Their corresponding eigenenergies are

$$E_n^{\pm} = \hbar\omega_c \left(n + \frac{1}{2}\right) \pm \frac{\hbar}{2}\sqrt{\Delta^2 + 4g^2(n+1)}. \tag{2.3.24}$$

On resonance ($\Delta = 0$), the energy splitting becomes

$$E_n^{\pm} = \hbar\omega_c \left(n + \frac{1}{2}\right) \pm \hbar g\sqrt{n+1}, \tag{2.3.25}$$

revealing the characteristic $\sqrt{n+1}$ nonlinearity of the Jaynes–Cummings ladder. This anharmonic spectrum has been experimentally observed in cavity and circuit quantum electrodynamics and constitutes one of the clearest signatures of the quantization of the electromagnetic field.

The Jaynes–Cummings Hamiltonian forms the starting point for numerous effective descriptions of light–matter interactions. Depending on the coupling strength and detuning, it gives rise to dispersive interactions, quantum non-demolition measurements, photon blockade, and effective optical nonlinearities. In the following subsection, we consider the dispersive regime, where the atom and cavity are far detuned, and derive the effective Hamiltonians that ultimately lead to Kerr-type nonlinearities used throughout this thesis.

2.4 Dispersive regime and effective Hamiltonians

The Jaynes–Cummings Hamiltonian provides an exact description of the coherent interaction between a two-level emitter and a single quantized cavity mode. While its resonant regime is characterized by the reversible exchange of excitations between the atom and the field, many cavity- and circuit-QED experiments operate in the opposite limit, where the atomic transition frequency and the cavity resonance are largely detuned. In this regime, the exchange of real excitations is strongly suppressed, and the interaction is instead mediated by virtual photon processes. Eliminating these virtual transitions leads to an effective Hamiltonian that accurately describes the system dynamics while revealing the origin of dispersive frequency shifts and nonlinear optical effects.

The dispersive regime is defined by

$$|\Delta| = |\omega_q - \omega_c| \gg g\sqrt{\langle n \rangle}, \tag{2.4.1}$$

where Δ is the atom–cavity detuning. Under this condition, the probability of exchanging excitations between the atom and the cavity is negligible, allowing the interaction to be treated perturbatively.

The Jaynes–Cummings Hamiltonian can be written as

$$\hat{H} = \hat{H}_0 + \hat{V}, \tag{2.4.2}$$

where

$$\hat{H}_0 = \hbar\omega_c \hat{a}^\dagger \hat{a} + \frac{\hbar\omega_q}{2}\hat{\sigma}_z, \tag{2.4.3}$$

$$\hat{V} = \hbar g \left(\hat{a}^\dagger \hat{\sigma}_- + \hat{a}\hat{\sigma}_+\right). \tag{2.4.4}$$

Since the interaction is weak compared with the detuning, it is convenient to eliminate it perturbatively through a Schrieffer–Wolff transformation. This procedure consists of performing a unitary transformation generated by an anti-Hermitian operator $\hat{S}$,

$$\hat{H}_{\text{eff}} = e^{\hat{S}} \hat{H} e^{-\hat{S}}, \tag{2.4.5}$$

whose purpose is to remove the interaction to first order in the small parameter g/Δ. Expanding Eq. (2.4.5) through the Baker–Campbell–Hausdorff formula yields

$$\hat{H}_{\text{eff}} = \hat{H} + [\hat{S}, \hat{H}] + \frac{1}{2}[\hat{S}, [\hat{S}, \hat{H}]] + \cdots. \tag{2.4.6}$$

Substituting $\hat{H} = \hat{H}_0 + \hat{V}$ gives

$$\hat{H}_{\text{eff}} = \hat{H}_0 + \hat{V} + [\hat{S}, \hat{H}_0] + [\hat{S}, \hat{V}] + \frac{1}{2}[\hat{S}, [\hat{S}, \hat{H}_0]] + \cdots. \tag{2.4.7}$$

The generator is chosen such that

$$[\hat{H}_0, \hat{S}] = -\hat{V}, \tag{2.4.8}$$

which cancels the interaction term to first order, leaving only second-order corrections associated with virtual transitions. A convenient solution of Eq. (2.4.8) is

$$\boxed{\hat{S} = \frac{g}{\Delta}\left(\hat{a}^\dagger \hat{\sigma}_- - \hat{a}\hat{\sigma}_+\right),} \tag{2.4.9}$$

which satisfies $\hat{S}^\dagger = -\hat{S}$, ensuring that the transformation remains unitary.

Keeping terms up to second order in g/Δ, the effective Hamiltonian becomes

$$\hat{H}_{\text{eff}} = \hat{H}_0 + \frac{1}{2}[\hat{S}, \hat{V}] + \mathcal{O}\left(\frac{g^3}{\Delta^2}\right). \tag{2.4.10}$$

Evaluating the commutator gives

$$[\hat{S}, \hat{V}] = \frac{2g^2}{\Delta}\left[\left(\hat{a}^\dagger\hat{a} + \frac{1}{2}\right)\hat{\sigma}_z + \frac{1}{2}\right], \tag{2.4.11}$$

where the last term corresponds only to a constant energy shift and can therefore be omitted. The resulting effective Hamiltonian is

$$\boxed{\hat{H}_{\text{disp}} = \hbar\omega_c\hat{a}^\dagger\hat{a} + \frac{\hbar}{2}(\omega_q + \chi)\hat{\sigma}_z + \hbar\chi\hat{a}^\dagger\hat{a}\hat{\sigma}_z,} \tag{2.4.12}$$

where

$$\boxed{\chi = \frac{g^2}{\Delta}} \tag{2.4.13}$$

is the dispersive coupling strength.

Equation (2.4.12) shows that the exchange of real excitations has been eliminated. The atom and the cavity no longer exchange photons, but the virtual transitions induce state-dependent frequency shifts. From the cavity perspective, the resonance frequency becomes

$$\omega_c \to \omega_c \pm \chi, \tag{2.4.14}$$

depending on whether the atom occupies its ground or excited state. Conversely, the atomic transition acquires the photon-number-dependent ac Stark shift

$$\omega_q \to \omega_q + 2\chi n, \tag{2.4.15}$$

where

$$n = \hat{a}^\dagger\hat{a}. \tag{2.4.16}$$

Thus, the presence of photons modifies the atomic transition frequency without changing the photon number stored inside the cavity.

Since

$$[\hat{H}_{\text{disp}}, \hat{n}] = 0, \tag{2.4.17}$$

the photon number remains conserved throughout the evolution. This property constitutes the basis of quantum non-demolition (QND) measurements, allowing information about the cavity field to be extracted without destroying the stored photons. Likewise, the atom accumulates a phase proportional to the intracavity photon number, while the cavity field acquires a phase conditioned on the internal atomic state. Such conditional phase shifts are fundamental resources for quantum logic gates, quantum state engineering, and quantum state tomography.

Although the Schrieffer–Wolff transformation modifies both the Hamiltonian and the quantum states according to

$$|\psi_{\text{eff}}\rangle = e^{\hat{S}}|\psi\rangle, \tag{2.4.18}$$

the generator $\hat{S}$ is proportional to the small parameter g/Δ. Consequently, the transformed (dressed) eigenstates differ from the bare product states only by corrections of order g/Δ,

$$|\widetilde{\psi}\rangle = |\psi\rangle + \mathcal{O}\left(\frac{g}{\Delta}\right). \tag{2.4.19}$$

To the same order of approximation employed in deriving Eq. (2.4.12), it is therefore sufficient to work in the bare basis $\{|g,n\rangle, |e,n\rangle\}$, while the effects of virtual photon exchange are entirely incorporated into the effective Hamiltonian. Physically, the atom and cavity become weakly dressed by one another, but the photon-number basis remains an excellent approximation in the dispersive regime.

The Schrieffer–Wolff procedure can be systematically extended by retaining higher-order terms in the Baker–Campbell–Hausdorff expansion. While the second-order contribution produces the dispersive interaction, the leading nonlinear correction appears at fourth order in the perturbative parameter g/Δ. The effective Hamiltonian then acquires the form

$$\hat{H}_{\text{eff}} = \hat{H}_{\text{disp}} + \hbar K(\hat{a}^\dagger\hat{a})^2 + \mathcal{O}\left(\frac{g^6}{\Delta^5}\right), \tag{2.4.20}$$

where

$$K \sim \frac{g^4}{\Delta^3}. \tag{2.4.21}$$

Unlike the dispersive interaction, which produces a frequency shift proportional to the photon number, the Kerr term makes the cavity frequency itself depend on the intracavity population. Indeed,

$$E_n = \hbar\omega_c n + \hbar K n^2, \tag{2.4.22}$$

so that the transition frequency between adjacent Fock states becomes

$$\omega_{n\to n+1} = \omega_c + (2n+1)K. \tag{2.4.23}$$

Therefore, the cavity no longer behaves as a harmonic oscillator with equally spaced energy levels, but instead becomes anharmonic. As a consequence, different photon-number components accumulate different dynamical phases during the evolution, providing the microscopic origin of self-phase modulation, photon blockade, Schrödinger-cat generation, and a wide variety of non-Gaussian state engineering protocols.

More generally, higher-order perturbative corrections naturally give rise to effective Hamiltonians that depend only on the photon-number operator,

$$\hat{H} = f(\hat{n}), \tag{2.4.24}$$

which form an important class of nonlinear interactions in quantum optics. These Hamiltonians constitute the theoretical framework employed in Chapter 2, where we demonstrate that arbitrary photon-number nonlinearities universally transform coherent states into highly non-Gaussian quantum states.

Chapter 3

Emergence of Non-Gaussian Coherent States

Chapter 1 highlighted the importance of nonclassical states as key resources for quantum technologies and continuous-variable quantum information. At the same time, coherent states remain the most accessible and widely used states of the electromagnetic field, owing to their robustness, ease of generation, and broad applicability across quantum optical platforms [17, 35]. An important question therefore arises: under what conditions can useful quantum properties be extracted from these seemingly classical, yet inherently quantum, states of light [36, 37]?

This chapter addresses this question by considering the evolution of coherent states under a broad class of nonlinear Hamiltonians. Using a general theoretical framework, we identify the minimal physical ingredients required for coherent states to develop genuinely nonclassical features.

Within this framework, we introduce a family of electromagnetic-field states describing the evolution of an initially coherent state under nonlinear interactions. We show that photon-number nonlinearities provide a general mechanism for the emergence of nonclassicality, independently of the microscopic origin of the interaction and regardless of whether the associated matter subsystem is initially in a pure or mixed state. As a consequence of this nonlinear evolution, the resulting states generally develop non-Gaussian features that evokes nonclassicality. We characterize their nonclassicality through the negativity of the Wigner function [26, 38] and the quantum Fisher information [39], revealing their nonclassicality and metrological potential.

These results establish a general connection between nonlinear optical evolution, the emergence of nonclassicality, and the generation of non-Gaussian states from initially coherent light. This provides the conceptual foundation for the subsequent chapters, where we move beyond the question of how nonclassical states emerge to address how they can be deterministically engineered and efficiently characterized.

3.1 Model

The light-matter interaction Hamiltonian in the dipole approximation is given by $\hat{H}_{\text{int}} = -\hat{\mathbf{P}}_{\text{a}} \cdot \hat{\mathbf{E}}$, where $\hat{\mathbf{E}}$ is the electric field and $\hat{\mathbf{P}}_{\text{a}}$ is the total atomic dipole moment. Depending on the atomic susceptibility, the interactions are generally nonlinear in the electric field, as $\hat{P}_{\text{a}} \propto \sum_i \chi^{(i)} \hat{E}^i$, where the i-th order susceptibility $\chi^{(i)}$ characterizes the i-th order nonlinear response of the medium [40]. For an initial coherent state of the field in the large intensity limit, atoms and field evolve almost as separable states [41, 42, 43, 44]. In such case, the interaction Hamiltonian in the interaction picture and rotating wave approximation can be approximated by a product of the atomic operator and a field operator proportional to the square-root of the photon number, $\hat{E} \sim \sqrt{\hat{n}}$, as $\hat{H}_{int} = \hbar g_i \hat{S}_x \hat{n}^{\frac{i+1}{2}}$, where g_i includes the information of the i-th order susceptibility, $\hat{S}_{(x,y,z)}$ is the collective atomic spin operator, and we have assumed the atomic frequency to be $i+1$ times the field frequency[1].

To study a range of nonlinear light-matter interactions for single-mode macroscopic states of the EM field, independently of the details of the matter subsystem, we consider the following interaction Hamiltonian in the interaction picture

$$\hat{H}_{\text{int}} = \hbar g \hat{n}^{\epsilon} \hat{O}_a, \tag{3.1.1}$$

where $\hbar$ is the reduced Planck constant, g is the coupling frequency, $\hat{O}_a$ is an atomic operator, and ϵ is the nonlinear parameter , determined by the type of interaction.

Although Eq. (3.1.1) excludes some nonlinear interactions, such as the squeezing

[1] This particular condition is equivalent to a degenerate parametric amplification of an arbitrary order, which could be selected by imposing the resonant condition of the field in a cavity.

Hamiltonian, it represents the simplest form of nonlinearities and provides a useful representation of a range of physical interactions. For example: the Jaynes-Cummings Hamiltonian in the dispersive limit, when $\epsilon = 1$ and $\hat{O}_a = \hat{S}_z$[45]; the Kerr Hamiltonian, when $\epsilon = 2$ and $\hat{O}_a$ is a non-zero constant number [46]; and the Jaynes-Cummings Hamiltonian in the resonant intense field limit, when $\epsilon = 1/2$ and $\hat{O}_a = \hat{S}_x$ [37, 41, 42, 43, 44]. Particularly, $\epsilon = (i+1)/2$ is related to a resonant i-th order susceptibility when $\hat{O}_a = \hat{S}_x$, and its definition helps to show that non-classical light emerges for nonlinearities in the photon number operator.

We assume that the initial state of the light-matter system $|\psi(0)\rangle$ is the outer product of the field in a coherent state $|\alpha\rangle$ and an arbitrary atomic pure state $\sum_j c_j |\lambda_j\rangle$, where $|\lambda_j\rangle$ are the eigenstates of $\hat{O}_a$. The Schrödinger equation for the evolution of $|\psi(t)\rangle$ leads to the state [2]

$$|\psi(t)\rangle = \sum_j c_j \left|\alpha_{\theta_j,\epsilon}(t)\right\rangle \otimes |\lambda_j\rangle\,, \tag{3.1.2}$$

where

$$|\alpha_{\theta,\epsilon}(t)\rangle = \sum_n \frac{\alpha^n e^{-|\alpha|^2/2}}{\sqrt{n!}} \mathrm{Exp}\left\{-\mathrm{i}\theta \mathrm{n}^{\epsilon}\mathrm{t}\right\}|\mathrm{n}\rangle\,, \tag{3.1.3}$$

and $\theta_j = g\lambda_j$ is a function of the light-matter coupling strength and the eigenvalues of the atomic operator.

The states $|\alpha_{\theta,\epsilon}(t)\rangle$ constitute a subset of the previously called generalized coherent states (GCS) [47, 48, 49, 50], and in this work we refer to them as such. As we will show next, they represent the evolution of the EM field from a Gaussian (standard) to a non-Gaussian coherent state, maintaining the photon statistics while offering a metrological quantum advantage.

3.2 Generalized coherent states

The GCS represent a family of states that fully characterizes the evolution of a coherent state under nonlinear light-matter interactions of the form of Eq. (3.1.1). They reduce to well-known states depending on the details of the interaction. For example: $|\alpha_{0,\epsilon}(t)\rangle = |\alpha\rangle$, $|\alpha_{\theta,0}(t)\rangle = e^{-i\theta t}|\alpha\rangle$, $|\alpha_{\theta,1}(t)\rangle = \left|\alpha e^{-i\theta t}\right\rangle$, and $|\alpha_{\theta,2}(t)\rangle$

[2] The overall approximation of the interaction Hamiltonian in Eq. (3.1.1) and the separable atom-field evolution at any time t for some atomic initial states ($|\lambda_j\rangle$), are valid as long as $gt < \bar{n}$ [41, 42], equivalent to the intense field limit we are studying.

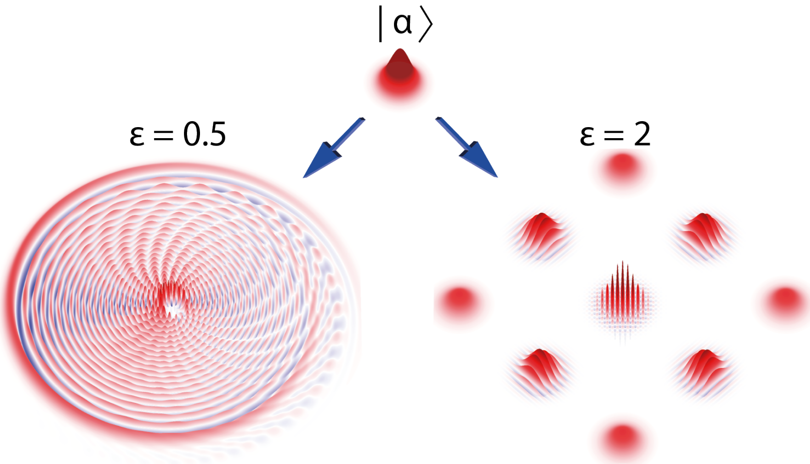

Figure 3.1.1: Examples of possible evolutions of an intense, macroscopic, coherent state of the electromagnetic field upon nonlinear interaction with matter. The Wigner functions represent the state of the field $|\alpha\rangle$, with $|\alpha|^2 = 50$, that evolves from a coherent to a highly quantum non-Gaussian coherent state, depending on the nonlinear parameter ϵ given in Eq. 3.1.1. The color red (blue) represents positive (negative) values of the Wigner function.

represents Kerr states [46], which have been largely studied for their potential applications in quantum metrology. Fig. 3.1.1 exemplifies two possible evolutions of the Wigner function of GCS for $\epsilon = 0.5$ and 2. The figures share the same scale, which exemplifies how a minimum-uncertainty, nearly localized, state can spread over the quadrature space creating a, evidently quantum, non-Gaussian field.

GCS are non-orthogonal and they form an overcomplete basis, with $\int d\alpha \, |\alpha_{\theta,\epsilon}(t)\rangle \langle\alpha_{\theta,\epsilon}(t)| = \pi\mathbb{1}$, where $\mathbb{1}$ is the identity operator. Their mean photon number is constant throughout the evolution, $\langle\alpha_{\theta,\epsilon}(t)| \, \hat{n} \, |\alpha_{\theta,\epsilon}(t)\rangle = |\alpha|^2$. In general, the expectation value of any power of the photon number operator respect to the GCS is the same as the one respect to a coherent state, meaning $\langle\alpha_{\theta,\epsilon}(t)| \, \hat{n}^m \, |\alpha_{\theta,\epsilon}(t)\rangle = \langle\alpha| \, \hat{n}^m \, |\alpha\rangle$[51]. In particular, their Mandel Q parameter [21] and its generalization to higher order statistics [52, 53] corresponds to the same photon statistics of a coherent state. More properly defined, given the n-order correlation function of the field $G^{(n)}$, a state is said to have coherence of the m-order if $|G^{(n)}|^2 = \Pi_{j=1}^{2n} G^{(1)}$ for $n \leq m$ [17, 54], equivalent to say that the n-th order normalized correlation function is equal to one. Such condition is satisfied to all orders for the GCS, earning them the name coherent. Furthermore, GCS do not show minimum-uncertainty or squeezing in any quadrature [49, 51]. This means that any non-Gaussianity or quantum advantage that they might present does not come from removing or adding a quanta of light to the field or changing its Poissonian photon statistics. It rather comes from the evolution of the quantum fluctuations of the electric field.

The underlying physical mechanism can be easily interpreted using the Wigner function representation of the field: While a linear evolution simply rotates a coherent state in quadrature space, a nonlinear evolution (in the radial direction) unevenly spreads the minimal uncertainty region of a coherent state throughout the quadrature space [3]. Since all radial components of the field evolve periodically circling the phase space, periodic structures emerge (see Fig. 3.1.1). The unitary evolution preserves the phase coherence among the EM field components, producing high visibility fringes in the Wigner representation, and therefore its negative values. The metrological advantage is related to the size of such fringes, since small displacement of the fields lead to a noticeable displacement of fringe pattern.

3.3 Non-Gaussianity of generalized coherent states

We characterize the non-Gaussianity of the EM field by the condition of a negative value in its Wigner function [26, 38], which indicates quantum features. The Wigner negativity is defined as $\mathcal{N}_\phi = \int d\beta \left[|W^{|\phi\rangle\langle\phi|}(\beta)| - W^{|\phi\rangle\langle\phi|}(\beta)\right]$, where $W^{|\phi\rangle\langle\phi|}$ is the Wigner function of $|\phi\rangle$.

The Wigner functions of the GCS, given by Eq. (3.1.3), are:

$$W^{\left|\alpha_{\theta,\epsilon}\right\rangle\left\langle\alpha_{\theta,\epsilon}\right|}(\beta) = \frac{2e^{-\alpha^2-2r^2}}{\pi}\Bigg(e^{-\alpha^2+4\alpha r\cos\delta} - 4\sum_{m,n,m>n}(-1)^n\frac{\alpha^{m+n}}{m!}\sin\left((m-n)\delta+\frac{\theta}{2}(m^\epsilon-n^\epsilon)\right) \sin\left(\frac{\theta}{2}(m^\epsilon-n^\epsilon)\right)(2r)^{m-n}L_n^{m-n}(4r^2)\Bigg), \quad (3.3.1)$$

where L_n^m are the generalized Laguerre polynomial [55] and $\beta = re^{i\delta}$ is a complex number that represents every point in quadrature space.

While a linear evolution leaves the phase space representation of a coherent state unchanged, nonlinearities will create a nontrivial superposition of different components of the probability distribution of the field. The Wigner representation

[3]For a clear visualization of the process, see the video in the Supplemental Material of Ref [37]

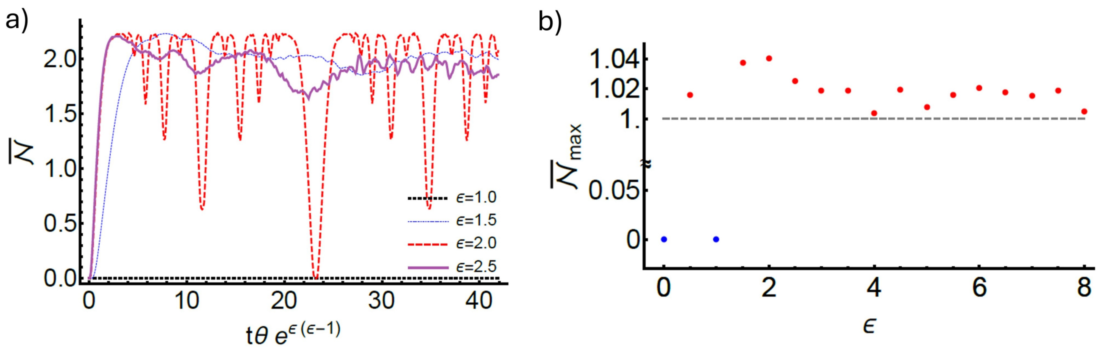

Figure 3.3.1: a) Wigner negativity $\bar{\mathcal{N}}$ as a function of the evolution parameter θ for different nonlinear parameters ϵ considering an initial coherent state with an average photon number of $\bar{n} = 10$. The evolution parameter is re-scaled by $e^{\epsilon(\epsilon-1)}$ for visualization purposes. b) Maximum Wigner negativity as a function of the nonlinear parameter. The red (blue) dots represent non-zero (zero) negativity. $\bar{\mathcal{N}}$ is normalized to that of a Fock state with $n = 10$ for both figures.

of such a superposition of states of the field would then be non-Gaussian, showing fringes and negative values. Fig. 3.3.1 a) shows the evolution of the Wigner negativity $\mathcal{N}$ of GCS for different values of the nonlinear parameter ϵ, numerically calculated from Eq. (3.3.1). We normalize the negativity by that of a Fock state with the same mean photon number. We observe that as long as there is a degree of nonlinearity ($\epsilon \notin \{0, 1\}$), the field will eventually become non-classical [4]. Fig. 3.3.1 b) shows the maximum Wigner negativity reached through the entire evolution for different values of ϵ. For all nonlinear interactions, the negativity of the GCS can surpass that of a Fock state. This result opens a discussion about the interpretation of the negativity of the Wigner function and how, or if, quantumness could be quantified, which is beyond the scope of this paper.

3.4 Quantum advantage of coherent states

The metrological advantage of the GCS can be quantified by their quantum Fisher information $\mathcal{F}^{\mathrm{Q}}$ [39]. It relates to the minimum attainable uncertainty in estimating a parameter δx via the Cramer-Rao bound $\sqrt{\langle \delta x^2 \rangle} \geq 1/\sqrt{\bar{n}\mathcal{F}^{\mathrm{Q}}}$, where $\bar{n}$ is the mean number of photons involved in the measurement. When the quantum Fisher information scales with the average number of photons, one achieves the minimum uncertainty $\sqrt{\langle \delta x^2 \rangle} \propto 1/\bar{n}$, which is the optimum scenario

[4]We point out that the time at which the Wigner negativity for $\epsilon < 1$ is maximum is not shown in the figure for visualization purposes.

for quantum metrology known as the Heisenberg limit [56, 57]. GCS are good candidates to detect small displacements of the field [58, 59]. The quantum Fisher information for displacements in the phase space of a pure state is given by the variance of the quadrature in the direction orthogonal to the displacement, namely $\mathcal{F}^{\mathrm{Q}} = 4\,\langle(\Delta X)^2\rangle$ [57].

The quadrature variance of a GCS is (see Appendix A1)

$$\left\langle(\Delta X)^2\right\rangle_{\alpha_{\theta,\epsilon}}(t) = 4\bar{n}\left(\left\langle \mathrm{Re}[z_{n,2}^{1/2}(t)]^2\right\rangle_\alpha - \langle \mathrm{Re}[z_{n,1}(t)]\rangle_\alpha^2\right) + 1 \qquad (3.4.1)$$

where we define the expectation value $\langle o_n\rangle_\alpha = \sum_n |\langle\alpha|n\rangle|^2 o_n$ and the function $z_{n,j}(t) = \mathrm{Exp}\{-i\theta(t)((n+j)^\epsilon - n^\epsilon)\}$. GCS evolve between states of large and small Fisher information, with $1 \leq \langle(\Delta X)^2\rangle_{\alpha_{\theta,\epsilon}} \leq 4\bar{n}+1$. The $\bar{n}$ dependence in the variance, and consequently $\mathcal{F}^{\mathrm{Q}}$, leads to the Heisenberg limit. We highlight that the maximum Fisher information for GCS is equivalent to that of a squeezed state with a squeezing of $-10\mathrm{Log}_{10}\,[4\bar{\mathrm{n}}+1]$ dB [5], while displaying non-minimum uncertainty and Poissonian photon statistics.

Figure 3.4.1 a) shows the evolution of the quantum Fisher information $\bar{\mathcal{F}}^{\mathrm{Q}}$ for different nonlinear parameters, normalized by its highest value. The quantum Fisher information from the variance of the orthogonal quadrature is equivalent, but with the red-to-blue fringes in the figure completely out of phase. Fig. 3.4.1 b) shows the maximum quantum Fisher information reached through the entire evolution for different nonlinear parameters. We observe a metrological advantage over a coherent state for all nonlinear parameters, reaching an optimum $\bar{\mathcal{F}}^{\mathrm{Q}}_{\mathrm{max}} = 1$.

Both Figs. 3.3.1 and 3.4.1 show the evolution of a coherent state with an average photon number of $\bar{n} = 10$. Nonetheless, the overall behavior of $\bar{\mathcal{N}}$ and $\bar{\mathcal{F}}^{\mathrm{Q}}$ is independent of $\bar{n}$. For the range of numerically tested parameters, $\bar{\mathcal{N}}_{\mathrm{max}} > 1$ for all nonlinear interactions. Similarly, the dynamic behavior of $\bar{\mathcal{F}}^{\mathrm{Q}}_{\mathrm{max}}$ always oscillate between 0 and 1 for even values of ϵ and offers metrological advantage over a coherent state for $\epsilon \neq \{0, 1\}$. This result shows that non-classicality emerges for arbitrarily large, *i.e.* macroscopic, initial coherent states of the EM field.

[5]For $\bar{n} > 8$ one can generate states with metrological advantage beyond what has been experimentally achieved with squeezed light [60, 61]

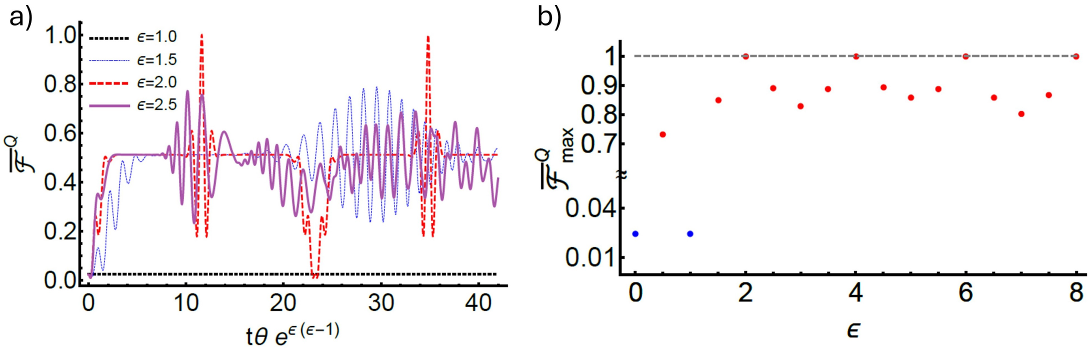

Figure 3.4.1: a) Quantum Fisher information $\bar{\mathcal{F}}^{\mathrm{Q}}$ and as a function of the evolution parameter θ for different nonlinear parameters ϵ considering an initial coherent state with an average photon number of $\bar{n} = 10$. The evolution parameter is re-scaled by $e^{\epsilon(\epsilon-1)}$ for visualization purposes. b) Maximum quantum Fisher information as a function of the nonlinear parameter. The red (blue) dots represent metrological advantage (or lack thereof). $\bar{\mathcal{F}}$ is normalized to its maximum value, $4(4\bar{n}+1)$.

3.5 Role of the atomic subsystem

So far, we have analyzed the case of the EM field interacting with a medium consisting of one or many atoms in a pure state that is the eigenstate of the collective atomic spin operator represented by $\hat{O}_a$ in Eq. (3.1.1). Such description leaves out the effects of the atomic state on the EM field. To address this issue, we consider that the atomic subsystem starts in an arbitrary mixed state $\rho_a(0) = \sum_{i,j} \rho_{ij} |\lambda_i\rangle \langle\lambda_j|$. Then, the state of the EM field evolves to $\rho_f(t) = \sum_j \rho_{jj} \left|\alpha_{\theta_j,\epsilon}(t)\right\rangle \left\langle\alpha_{\theta_j,\epsilon}(t)\right|$, a statistical mixture of the GCS. Such mixed states have diminished quantum properties compared to pure GCS, since the field can get entangled with the atoms upon evolution [45], but they can still be non-classical.

To quantitatively assess the role of quantum correlations in the initial state of the atomic subsystem, we consider it to be a Werner state defined as [62, 63]

$$\rho_a(0) = p\,|\Psi\rangle \langle\Psi| + (1-p)\frac{1 \otimes 1}{d}, \tag{3.5.1}$$

where d is the dimension of the Hilbert space of the atomic subsystem, and $|\Psi\rangle = \sum_j c_j |\lambda_j\rangle$ is an arbitrary pure state written in terms of the eigenstates $|\lambda_j\rangle$ of the collective atomic operator $\hat{O}_a$. The parameter p allows to continuously vary the initial state from fully mixed ($p = 0$) to pure ($p = 1$). Tracing over the atomic subsystem, the state of the EM field after its evolution is

$$\rho_f(t) = \sum_j \left(p|c_j|^2 + \frac{1-p}{d} \right) \left| \alpha_{\theta_j,\epsilon}(t) \right\rangle \left\langle \alpha_{\theta_j,\epsilon}(t) \right| . \tag{3.5.2}$$

Since the Wigner function is a linear transformation, we get that

$$W^{\rho_f}(\beta, t) = \sum_j \left(p|c_j|^2 + \frac{1-p}{d} \right) W^{\left|\alpha_{\theta_j,\epsilon}(t)\right\rangle \left\langle \alpha_{\theta_j,\epsilon}(t)\right|}(\beta). \tag{3.5.3}$$

Figure 3.5.1 shows the maximum normalized Wigner negativity $\bar{\mathcal{N}}_{\max}$ during the EM field evolution as a function of the Werner parameter p. The initial atomic state in the case of highest purity ($p = 1$) corresponds to an eigenstate of the atomic operator, leading to a pure GCS state of the EM field. The Wigner negativity increases monotonically with p, same as the purity of the initial atomic state $P = Tr\{\rho_a(0)^2\}$.

From Eq. (3.5.3) one sees that for $|c_j|^2 = 1/d$ the Wigner function of the EM field does not depend on p. This means that the obtained state of the field is the same whether the initial atomic state is fully mixed or a pure state with an equal superposition of eigenstates of the atomic operator $\hat{O}_a$. Moreover, for $d = 2$, the maximally entangled states are equal superpositions of the eigenstates of the collective atomic operators $\hat{S}_{(x,y,z)}$. This suggests that quantum correlations between the atoms are not just unnecessary but can be detrimental for obtaining a non-classical EM field. Although Werner states, as in Eq. (3.5.1), might not constitute the most general scenario, they serve to prove by counterexample that quantum correlations in the atomic subsystem do not aid the emergence of quantum correlations in the field.

We notice that even for $p = 0$, the resulting mixed state of the EM field still presents a non-zero Wigner negativity for $\epsilon \neq \{0, 1\}$, evidencing the ubiquity of non-classical light emerging from nonlinear interactions. We highlight the universal aspect of the evolution into non-classicality since the maximum negativity of the resultant state of the EM field is relatively insensitive to the nonlinear parameter ϵ, especially towards high purity of the initial atomic state.

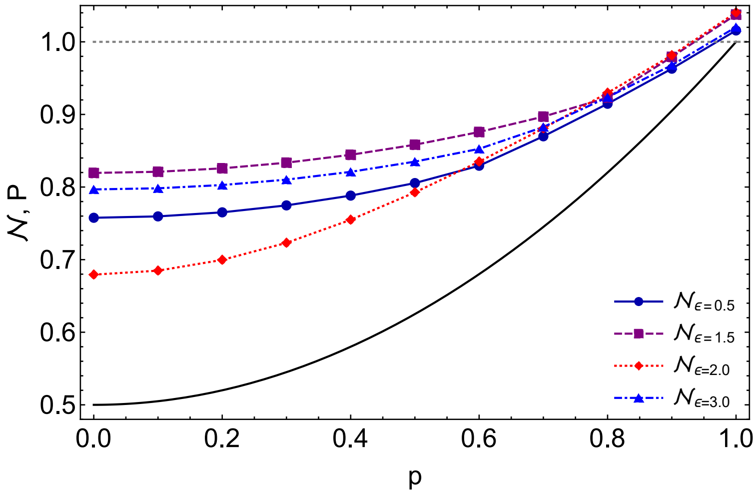

Figure 3.5.1: Maximum Wigner negativity $\bar{\mathcal{N}}_{\text{max}}$ of the EM field and purity P of the initial atomic state (solid black) as a function of the Werner parameter p. The negativity for the nonlinear parameters $\epsilon = \{0.5, 1.5, 2, 3\}$ is shown with circles, triangles, diamonds, and squares, respectively. The Wigner negativity is normalized to that of a Fock state with the same average photon number.

3.6 Discussion and outlook

Macroscopic coherent states of light are commonly considered the most classical ones. However, nonlinear interactions can be used to extract their quantum resources even in a closed system with no initial quantum correlations and unaffected by measurements [64, 65]. Our results are another example of this phenomenon.

This phenomenon offers new possibilities for engineering the EM field. For example, different linear combinations of the GCS can lead to useful states. In particular, combining two GCS with $\epsilon = 1/2$ one could obtain a macroscopic Fock state, as Ref. [37] discusses. On a different approach, one can study the metrological advantage gained by applying a broader class of nonlinear interactions to an initial state beyond a coherent one, for example an squeezed state.

We believe our result have natural applications in quantum metrology based on cavity QED platforms, for example, to precisely measure electromagnetic fields [58, 59]. However, the phenomenon is general enough to be extended to other quantum optics platforms.

3.7 Conclusions

In this chapter, we showed that photon-number nonlinearities provide a universal mechanism for extracting genuinely quantum features from coherent states. We demonstrated that any degree of nonlinearity gives rise to highly non-Gaussian states of light while preserving the characteristic Poissonian photon-number statistics of the initial coherent state. These states exhibit strong nonclassical features, revealed by the negativity of their Wigner function, together with a metrological advantage that can approach the Heisenberg limit.

Furthermore, we showed that this behavior is independent of the microscopic details of the interaction and remains valid regardless of whether the matter subsystem is prepared in a pure or mixed quantum state or initially exhibits correlations. These results establish non-Gaussianity as a universal consequence of nonlinear optical evolution.

This result provides a fundamental understanding of how useful quantum resources naturally emerge from coherent states through nonlinearities. Having established how nonclassical states naturally emerge from coherent states, the next chapter addresses the deterministic engineering of specific quantum states.

Chapter 4

Engineering of Multi-Photon Added Coherent States

Having established how nonclassical states emerge from coherent states, the next question naturally arises: how can specific nonclassical states be engineered using nonlinear interactions?

Among the many families of nonclassical states, photon-added coherent states (PACS) occupy a unique position by continuously interpolating between coherent states and photon-number states [66]. While coherent states are the closest quantum analog of classical electromagnetic fields [17], photon-number states are prototypical examples of nonclassical light [67, 68]. This intermediate character makes PACS valuable resources for quantum information science and fundamental studies [8, 69, 70, 71]. However, their generation has so far been largely restricted to small numbers of added photons and probabilistic protocols [72, 73, 74, 75].

This chapter addresses this question by introducing a protocol for the generation of high-fidelity multi-photon PACS without post-selection. We consider a coherently driven Kerr resonator (Fig. 4.0.1), where the interplay between the Kerr nonlinearity and the external drive naturally gives rise to displaced PACS. Because this displacement hides the target state during the evolution, we introduce a witness that identifies these states independently of phase-space displacements. By monitoring the dynamics of this witness, we identify the evolution time at which a displaced PACS is formed. We then determine the coherent displacement that removes the residual displacement and unveils the underlying N-photon

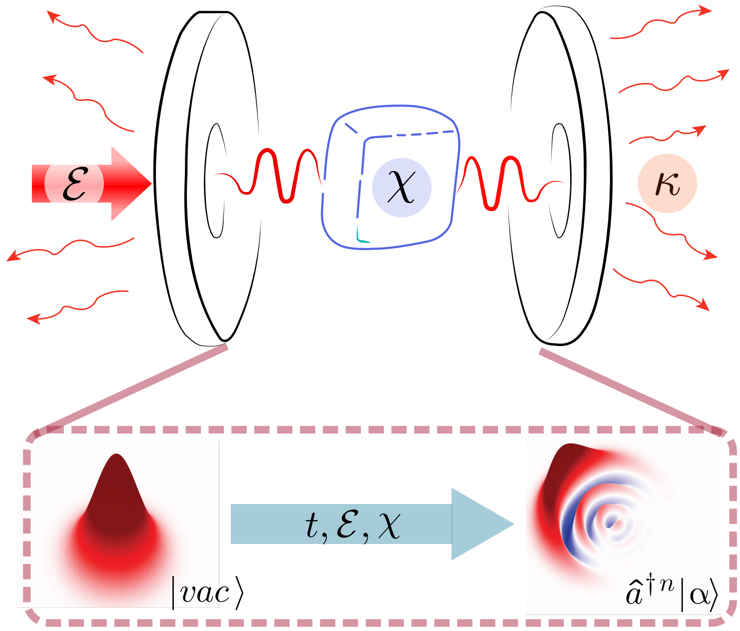

Figure 4.0.1: Schematic of the protocol for high fidelity generation of PACS. A coherent drive of amplitude $\mathcal{E}$ excites a single-mode cavity with Kerr nonlinearity χ and decay rate κ. Starting from the vacuum state $|vac\rangle$, the system reaches a state resembling a displaced multi-photon added coherent state $\hat{a}^{\dagger n}|\alpha\rangle$ at a time t. The lower panel illustrates the transformation in phase space, highlighting the emergence of non-classical features from an initially Gaussian state.

PACS.

Finally, we analyze the robustness of the protocol under realistic conditions using experimentally accessible parameters from recent circuit-QED experiments [76]. These results demonstrate a feasible route toward the post-selection free generation of highly nonclassical states. The following chapter addresses the complementary problem of their efficient characterization.

4.1 PACS definition

Coherent states of light $|\alpha\rangle$ are quantum states characterized by intensity correlations at all orders and a Poissonian photon-number distribution, which makes them nearly classical states [17]. In contrast, photon-number states $|n\rangle$ are the archetypic quantum states with particle-like intensity correlations without classical analogs, such as antibunching [77]. Photon-added coherent states (PACS) smoothly connect both contrasting examples [66]. They are obtained by applying

n times the creation operator, $\hat{a}^\dagger$, to a coherent state as

$$|\alpha, n\rangle = \frac{\hat{a}^{\dagger n} |\alpha\rangle}{\sqrt{N_n}}, \tag{4.1.1}$$

where n is an integer that determines the number of added photons and $N_n = n! L_n(-|\alpha|^2)$ is a normalization constant, with $L_n(x)$ being the Laguerre polynomial of order n [55]. In the limit $\alpha \to 0$, PACS tends to a photon-number state of n photons, while in the limit of large α, adding photons to a coherent state has negligible effects on its statistics, creating a crossover between non-classical to classical states as a function of α.

PACS can also be written in the photon-number basis as [66]

$$\begin{aligned} |\alpha, n\rangle &= \frac{\hat{D}(\alpha)}{\sqrt{N_n}} \sum_{s=0}^{n} \binom{n}{s} \sqrt{s!} (\alpha^*)^{n-s} |s\rangle \\ &= \hat{D}(\alpha) |\Gamma_{\alpha,n}\rangle , \end{aligned} \tag{4.1.2}$$

where $\hat{D}(\alpha)$ is the coherent displacement operator. Because the displacement operator is a linear transformation, $|\Gamma_{\alpha,n}\rangle$ preserves the essential features of the state, such as its non-Gaussian character. This notation allows us to relate PACS to a truncated Hilbert space [78], with an upper bound n, and suggests that systems with strong photon blockade [79, 80] could lead to PACS generation under right conditions.

4.2 Theoretical model

We consider a driven single-mode cavity containing a Kerr nonlinear medium in order to realize photon blockade. The evolution of the electromagnetic field inside the cavity is well described by the Drummond and Walls model [81], given by the Hamiltonian

$$\mathcal{H} = \hbar\omega_0 \hat{a}^\dagger \hat{a} + \hbar\mathcal{E} \left(\hat{a}\ e^{i\omega_d t} + \hat{a}^\dagger e^{-i\omega_d t} \right) + \hbar\chi \hat{a}^{\dagger 2} \hat{a}^2, \tag{4.2.1}$$

where ω_0 (ω_d) is the frequency of the cavity (driving) field, $\mathcal{E}$ the driving amplitude, and χ the nonlinearity strength. Working within a rotating frame with respect to

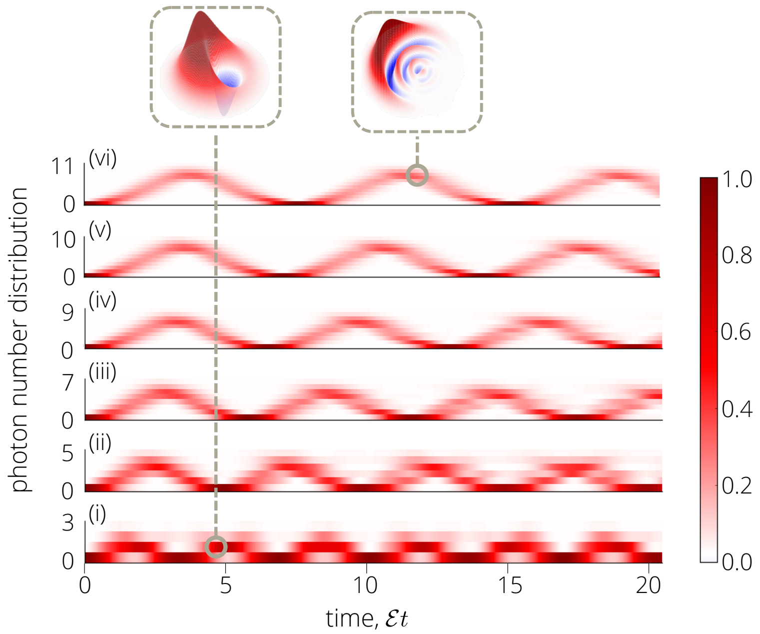

Figure 4.2.1: Photon number distribution as a function of evolution time for different driving values ($\mathcal{E}/\chi = 1.5, 4.5, 7.25, 10, 13, 16$) and fixed $\delta = 2\chi$. The roman numerals represent the number of added photons for the best PACS generated in each driving regime. The insets on the top represent the Wigner function of the best PACS found in the left ($n = 1$) and right ($n = 6$) cases.

the drive frequency ω_d, we obtain

$$\mathcal{H}_R = \hbar\delta\, \hat{a}^\dagger \hat{a} + \hbar\mathcal{E}(\hat{a} + \hat{a}^\dagger) + \hbar\chi\, \hat{a}^{\dagger 2}\hat{a}^2, \tag{4.2.2}$$

with detuning $\delta = \omega_0 - \omega_d$.

This Hamiltonian captures the competition between two mechanisms: the coherent drive increases the number of excitations along a defined phase in the quadrature space within the cavity, while the nonlinearity shifts the cavity out of resonance by activating upper number states, suppressing additional excitations. This competition between the drive and Kerr nonlinearity leads to a photon blockade [82], where the creation of additional photons in the cavity mode is inhibited [79, 83].

We consider the system initialized in the vacuum state $|\psi_{\text{sys}}(0)\rangle = |0\rangle$ and out of resonance ($\omega_0 \neq \omega_d$). Figure 4.2.1 shows the time evolution of the photon-number distribution for different driving amplitudes and fixed detuning $\delta = 2\chi$ (meaning that the field linear evolution frequency coincides with the smallest Kerr evolution frequency; see Appendix B1). The presence of an upper bound in the photon-number distribution evidences the effect of photon blockade. The insets in the upper part correspond to the Wigner function distributions of the states that closely resemble a displaced $|\Gamma_{\alpha,n}\rangle$ and produce PACS with high fidelity. These states emerge almost periodically, appearing at times determined by an interplay of drive amplitude and nonlinearity, suggesting the creation of dressed states connecting ground and fully blockaded states. They emerge almost when the photon number $\langle\hat{n}\rangle$ is maximum, or more precisely when the remnant photon number (defined bellow) is maximized.

4.3 Remnant photon number

As discussed above, the cavity field periodically evolves into a blockaded state that resembles $\hat{D}(\beta)\,|\Gamma_{\alpha,n}\rangle$. This state retains the fundamental non-classicality of a PACS [Eq. (4.1.2)] but follows a complex trajectory in the phase space due to the nonlinear dynamics. The followed trajectory creates a moving-target, whose fidelity respect to a PACS is difficult to compute, since there is no analytical solution for $\beta(t)$.

To bypass this limitation, we define the *remnant photon number* as a frame-independent witness of state formation, given by

$$n_r = \langle(\Delta\hat{x}_\theta)^2\rangle + \langle(\Delta\hat{x}_{\theta+\pi/2})^2\rangle - 1/2. \tag{4.3.1}$$

Here, $\hat{x}_\theta = (\hat{a}e^{-i\theta} + \hat{a}^\dagger e^{i\theta})/2$ is an arbitrary quadrature of the field, and $\langle(\Delta\cdot)^2\rangle$ represents the variance. Crucially, n_r measures the total fluctuations of the amplitude and depends only on the shape of the Wigner function, rendering it invariant under both rotation and coherent displacement [84]. This quantity corresponds to subtracting a constant of $1/2$ from the *total noise* [85], but it also illustrates another physical aspect. Physically, n_r represents the remnant photon number: the minimum mean photon number remaining in the field after an optimal displacement operation effectively centers the state at the origin of the phase space (see Appendix B1). For example, $n_r = 0$ for any coherent state $|\alpha\rangle$ and $n_r = n$ for the Fock state $|n\rangle$. As such, n_r can thus be regarded as a measure of non-classicality for pure states [85], related to its quantum Fisher information [18].

Consequently, we can use n_r to detect the emergence of the Fock-like structure inherent to PACS, independent of the displacement of the state. By monitoring the evolution, we identify the interaction times where n_r is maximized, signaling the formation of a PACS upon rectifying coherent displacement.

4.4 Parameters optimization and results

The cavity field state $|\psi(t)\rangle$ evolves almost periodically to a state close to displaced $|\Gamma_{\alpha,n}\rangle$. In order to obtain a PACS $|\alpha, n\rangle$, $|\psi(t)\rangle$ must be corrected by a coherent displacement with an unknown amplitude and phase. To find such a displacement, we first center $|\psi(t)\rangle$ in the phase space by applying a displacement $\hat{D}(-\gamma)$, with a measurable quantity $\gamma = \langle \hat{x}_0(t)\rangle + i\left\langle \hat{x}_{\pi/2}(t)\right\rangle$. The resulting state must then be displaced by $\hat{D}(\zeta)$ to approximate the PACS $|\alpha, n\rangle$. This means that we want to compute the fidelity of the state $|\Psi(t)\rangle = \hat{D}(\zeta)\hat{D}(-\gamma)\,|\psi(t)\rangle$ compared to $|\alpha, n\rangle$, defined as $F(t) = |\langle \alpha, n|\Psi(t)\rangle|^2$.

We emphasize that neither the displacement ζ nor the coherent state amplitude α are known, and their values depend on the state evolution. Given a value of $|\psi(t)\rangle$, we can find the values of α and ζ that optimize the PACS generation by maximizing F. Without loss of generality, we define the complex phase of α such that it has the same orientation as the phase space representation of the obtained state $|\Psi(t)\rangle$, so that ζ and α share a common phase $\phi(t)$. Thus, the optimization reduces to the parameters $|\zeta|$, $|\alpha|$, and ϕ.

To reduce the number of optimization parameters, we propose a heuristic model based on the evolution of the Wigner function of the field. We consider an ansatz for the complex phase $\phi(t)$, which is determined by the vector normal to the state trajectory in the phase space. There is an additional physical restriction: the number of photons should be the same for both $|\Psi(t)\rangle$ and $|\alpha, n\rangle$, allowing us to establish a relationship between the magnitudes of ζ and α. This relationship is given by

$$\zeta(\alpha) = \langle \hat{x}_\phi\rangle_{\alpha,n} \pm \sqrt{n_r(|\psi(t)\rangle) - n_r(|\alpha, n\rangle)}, \tag{4.4.1}$$

where $\langle \hat{x}_\phi\rangle_{\alpha,n}$ is the quadrature expectation value of the PACS $|\alpha, n\rangle$ and $n_r(|\alpha, n\rangle) = N_{n+1}/N_n - \langle \hat{x}_\phi\rangle^2 - 1$ is the remnant photon number for the PACS, with N_n being the normalization constant in Eq. (4.1.2). Finally, there is only one free parameter to optimize $|\alpha|$.

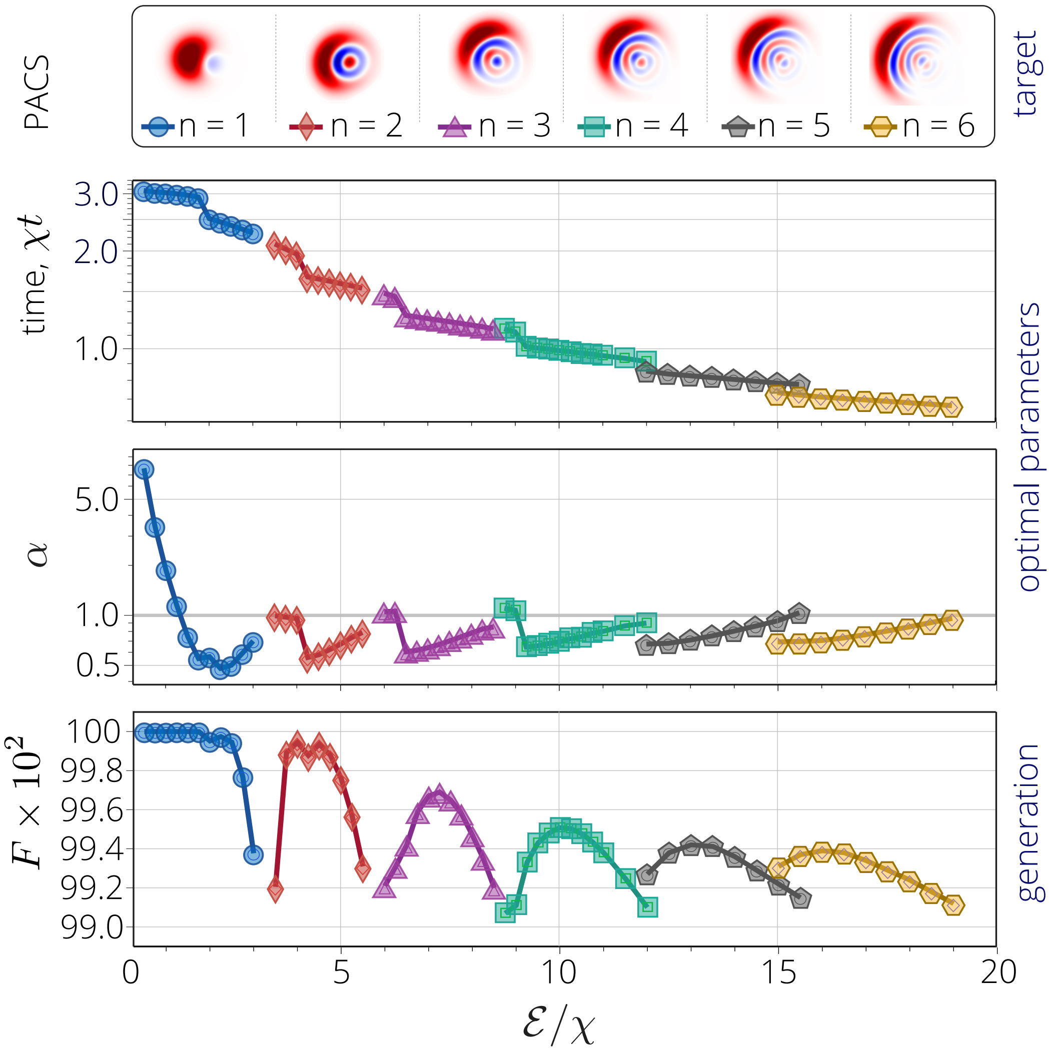

Figure 4.3.1: Fidelities and optimal parameters for PACS generation. The horizontal axis represents the drive amplitude $\mathcal{E}$ normalized by the nonlinear parameter χ. From top to bottom: Wigner function representations, optimal evolution time, amplitude of the coherent component, and optimal fidelity of the obtained PACS. The shapes connected by colored curves represent the different number of photons added n in the obtained PACS. We considered a drive detuning $\delta = 2\chi$ for all the calculations.

The procedure described above is ad first heuristic approximation and may not yield the highest fidelity. Therefore, we refine the result by varying ϕ around the guessed value after optimizing for $|\alpha|$. Our simple optimization procedure already produces PACS with large added photon numbers and fidelities exceeding 99%.

Figure 4.3.1 shows the fidelities and best parameters that optimize the procedure. These parameters were determined for a specific condition $\delta = 2\chi$. Out of this condition, the fidelity decays below 99%. In all cases, the optimization is localized in times around the second maxima of the remnant number of photons $n_r(|\psi\rangle)$. Figure 4.3.1 shows examples of the Wigner function representation of the generated states for increasing photon number, as well as the required evolution time, coherent amplitude $|\alpha|$, and fidelities for the generated PACS with up to 6 photons.

4.5 Experimental feasibility

In a realistic scenario, dissipation must be considered. In the rotating frame, the photonic state ρ of a lossy cavity evolves according to the master equation

$$\frac{d\rho}{dt} = \frac{1}{i\hbar}[\mathcal{H}_R, \rho] + \kappa(n_{\text{th}} + 1)\mathcal{L}_{\hat{a}}[\rho] + \kappa n_{\text{th}}\mathcal{L}_{\hat{a}^\dagger}[\rho] \tag{4.5.1}$$

where $\mathcal{L}_\xi[\bullet] = 2\xi \bullet \xi^\dagger - \bullet\xi^\dagger\xi - \xi^\dagger\xi\bullet$ is the Lindblad superoperator that describes incoherent processes. The parameter κ characterizes the cavity loss rate, while n_{th} is the mean thermal photon number, which accounts for finite-temperature effects.

Cavity losses degrade the purity of the evolving state. To assess the experimental feasibility of generating PACS, we numerically solve Eq. (4.5.1), apply the necessary coherent displacement to generate a PACS, and compute its infidelity $(1 - F)$ from the target state. Figure 4.5.1 shows the infidelity as a function of the cavity decay rate κ for different driving amplitudes $\mathcal{E}$. A vertical gray line indicates the experimental parameters for state-of-the-art experimental realizations [76]. We conclude that generating useful PACS with fidelities around 99%, is currently feasible.

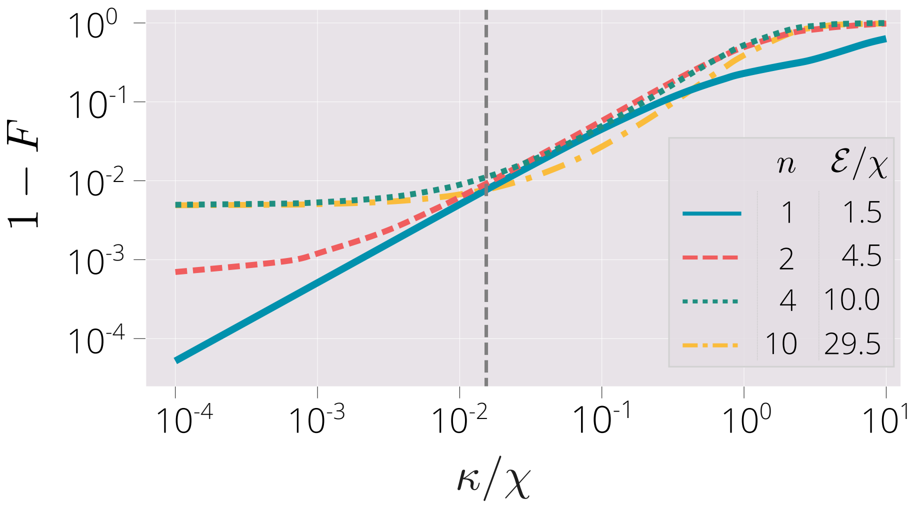

Figure 4.5.1: Infidelity for the optimal cases under decoherence for different driving amplitudes $\mathcal{E}$, with optimized numbers of added photons n. The vertical dashed gray line indicates the experimental state-of-the-art relation between the decoherence rate κ and the nonlinearity χ, as reported in Ref. [76].

4.6 Analysis and discussion

The deterministic generation of PACS relies on the interplay between photon blockade and the phase-space dynamics. The detuned drive creates an effective rotation around a displaced origin in the phase space, while the Kerr nonlinearity induces amplitude-dependent phase shifts (shearing). The emergent blockade effect acts as a rigorous constraint on the photon number distribution, preventing the st ate from spreading indefinitely. It is precisely this dynamical balance—confinement via blockade against shearing via nonlinearity—that sculpts the target non-classical state, in close analogy with the dynamic discussed in Ref. [86].

Owing to the quasi-periodic nature of these dynamics, the system approaches the target state at multiple interaction times, resulting in distinct solution branches. We find that the highest fidelities are achieved in the regime $|\alpha| < 1$ (see Fig. 4.3.1(c)).

Although the nonlinear nature of the system prevents a complete analytical solution, we find analytic results for the PACS generations in the weak drive limit using a perturbative method (see Appendix B1).

Finally, although we employed the remnant photon number n_r, specifically for PACS recognition, its utility extends to the characterization of general non-Gaussian resources. Because n_r quantifies non-classicality independent of the quadrature definition, it is superior to fixed-phase metrics for analyzing dynamic systems.

4.7 Conclusions

In this chapter, we showed that nonlinear interactions can be exploited to deterministically engineer specific nonclassical states of light. In particular, we introduced a post-selection-free protocol for the generation of high-fidelity multi-photon PACS using a coherently driven Kerr resonator, a well-established quantum-optical platform.

The protocol relies on the natural emergence of displaced PACS during the system dynamics. Because these states remain hidden by the coherent displacement, we introduced a displacement-independent witness that identifies the evolution time at which they appear. Once this time is determined, the corresponding coherent displacement can be found to recover the underlying PACS.

Our numerical simulations demonstrate the deterministic generation of PACS with at least ten added photons and fidelities exceeding 99% under unitary evolution. Moreover, the short timescale of the protocol naturally reduces the effects of environmental decoherence, allowing high-fidelity multi-photon PACS to remain accessible under realistic dissipation using state-of-the-art circuit-QED parameters.

By overcoming the probabilistic limitations of previous approaches, this protocol establishes a practical route toward the deterministic generation of highly non-Gaussian states for continuous-variable quantum information processing, quantum metrology, and fundamental studies. Having established how specific nonclassical states can be engineered, the following chapter addresses the complementary problem of their efficient characterization.

Chapter 5

Characterization of Continuous-Variable Quantum States

The previous chapters established how nonlinear interactions give rise to nonclassical states of light and how they can be harnessed to engineer specific quantum states. The next question naturally arises: how can continuous-variable quantum states be characterized beyond the limitations of conventional tomography?

The characterization of quantum states is essential for benchmarking, verification, and optimization across quantum technologies [2, 3, 4, 5, 6, 7]. In continuous-variable (CV) systems, however, tomography remains particularly demanding [87]. Compared with discrete-variable systems, its sample complexity increases rapidly with the energy of the field [88, 89, 90], while recovering quasiprobability distributions typically requires prior knowledge together with computationally intensive numerical methods [87, 91, 92, 93, 94, 95, 96, 97, 98, 99, 100]. Given the central role of CV platforms in quantum communication, sensing, and fault-tolerant quantum information processing [9, 10, 11, 12, 13, 14, 15], more efficient tomographic approaches are highly desirable.

This chapter addresses these challenges by introducing a family of CV tomography protocols based on quantum mirrors—light matter interfaces whose optical response is coherently controlled by an ancillary atom [101] (Fig. 5.0.1).

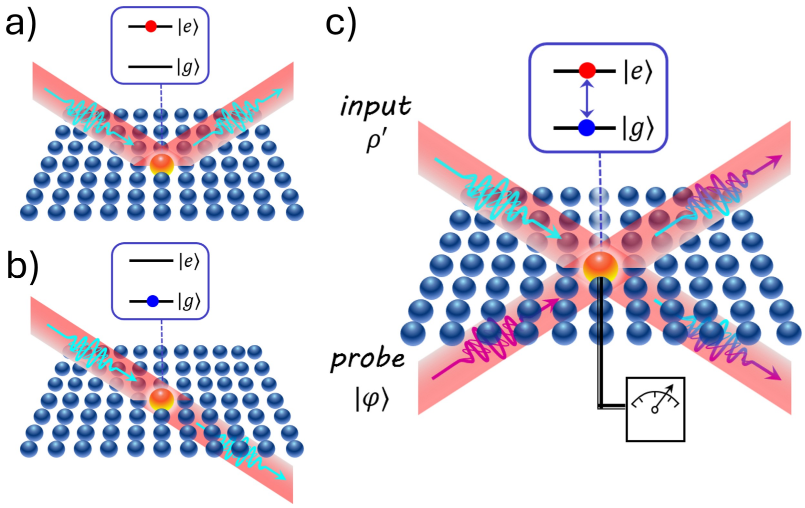

Figure 5.0.1: (a) The control atom in state $|e\rangle$ changes the optical response of the bulk, which generates a complete reflection, thus "gaining" a phase shift. (b) The control atom in state $|g\rangle$ generates complete transmission of the modes going through the mirror. (c) Representation of the quantum mirror in a superposition state and its effect on the input photonic modes.

By exploiting the entangling interaction between propagating optical modes and the control atom, these protocols reconstruct arbitrary unknown traveling states through measurements performed exclusively on the atomic system. They enable the direct determination of the wavefunction and a broad class of quasiprobability distributions, in several cases without prior information or numerical reconstruction.

Finally, we show that these protocols overcome several limitations of conventional homodyne tomography for propagating optical fields, including photodetection inefficiency, mode mismatch, bandwidth limitations, and electronic noise, by transferring the measurement task to the well-developed toolbox of two-level atom tomography. Together, these results establish quantum mirrors as a powerful platform for the efficient characterization of propagating CV states.

5.1 Quantum Mirrors

Atomic ensembles coupled to a control two-level atom, whose state induces perfect reflection or complete transparency for incoming electromagnetic modes [101], are usually referred to as quantum metasurfaces or *quantum mirrors* (QM). Coherent light-matter interaction enables the generation of entanglement between electromagnetic modes and the control two-level atom. These devices exhibit complex transmission and reflection coefficients [102], t and r, related by

$$t = e^{i\phi} + r, \tag{5.1.1}$$

where ϕ is the scattering phase acquired by each mode upon interaction. Although ϕ is often considered a global phase that can be neglected, it plays a central role in quantum mirrors by defining the relative phase in the quantum superposition between the transmitted and reflected fields (see Appendix C1).

The action of a mirror over two arbitrary incoming photonic states $\{|\psi\rangle, |\varphi\rangle\}$ is given by $\hat{U}_M$, under appropriate parameterization (see Appendix C1)

$$\hat{U}_M |\psi\rangle_0 |\varphi\rangle_1 = e^{-i\phi\hat{n}_0}\hat{\Pi}_0 |\varphi\rangle_0 e^{-i\phi\hat{n}_1}\hat{\Pi}_1 |\psi\rangle_1, \tag{5.1.2}$$

where $\hat{n}_k$ and $\hat{\Pi}_k = e^{i\pi\hat{n}_k}$ denote the photon-number and photon-parity operators for mode k, respectively. Owing to the coherent nature of the atom controlling the QM, the optical response of the medium can be modified such that an excited atom $|e\rangle$ leads to complete reflection, whereas its ground state $|g\rangle$ leads to transmission [103, 101]. In this case, the action of a QM is described by

$$\hat{U}_{QM} = \hat{\pi}_g \otimes \mathbf{1} \otimes \mathbf{1} + \hat{\pi}_e \otimes \hat{U}_M, \tag{5.1.3}$$

where $\hat{\pi}_k = |k\rangle\langle k|$ denotes the projector onto the atomic basis $\{|g\rangle, |e\rangle\}$. Here, the phase ϕ acquires physical relevance because it governs the superposition between the transmitted and reflected fields.

5.2 Measurement of the quantum states of light

To reconstruct the quantum state of light, we consider a single QM supplemented by controllable path-dependent phase shifts. Specifically, we apply a phase shift generated by $\hat{L}_3 = (\hat{a}_0^\dagger\hat{a}_0 - \hat{a}_1^\dagger\hat{a}_1)/2$ [102], as illustrated in Fig. 5.2.1.

One can engineer a photon-parity operator in the second mode by choosing $\phi = \pi/2$, such that the unitary operator of the complete setup $\hat{U}_S$ is given by (see

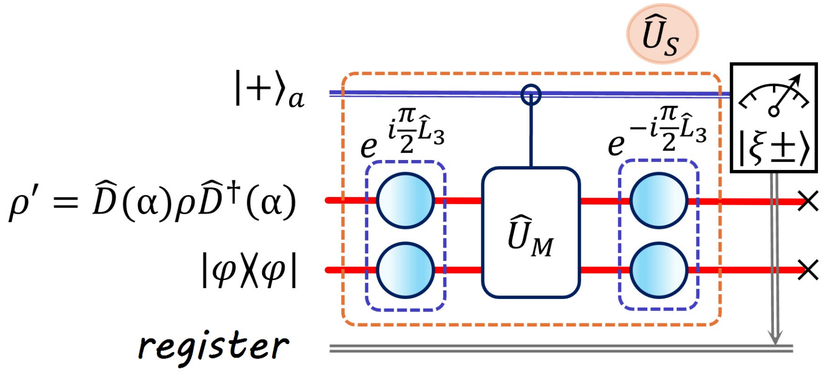

Figure 5.2.1: Quantum circuit implementing the unitary operation defined in Eq. (5.1.3). The system is initialized as an unknown input state ρ, coherently displaced by α, and a pure probe state $|\varphi\rangle$ in the photonic modes, while the control atom is in a superposition state $|+\rangle$. Finally, the control atom is measured. a measurement is taken onto the atom.

Appendix C1)

$$\begin{aligned}\hat{U}_S \left|g\right\rangle_a \left|\psi\right\rangle_0 \left|\varphi\right\rangle_1 &= \left|g\right\rangle_a \left|\psi\right\rangle_0 \left|\varphi\right\rangle_1 \\ \hat{U}_S \left|e\right\rangle_a \left|\psi\right\rangle_0 \left|\varphi\right\rangle_1 &= \left|e\right\rangle_a \left|\varphi\right\rangle_0 \hat{\Pi}_1 \left|\psi\right\rangle_1 .\end{aligned} \tag{5.2.1}$$

The platform initializes the control atom in $\left|+\right\rangle_a = (\left|g\right\rangle_a + \left|e\right\rangle_a)/\sqrt{2}$, coherently displaces an input state ρ by α, obtaining $\rho' = \hat{D}(\alpha)\rho\hat{D}^\dagger(\alpha)$, and injects a pure state $|\varphi\rangle$ as the probe. The system entangles the control atom and photonic modes via Eq. (5.2.1). Then, measuring the control atom in the convenient superposition states $\left|\xi_\pm\right\rangle_a = (\left|g\right\rangle_a \pm e^{i\delta}\left|e\right\rangle_a)/\sqrt{2}$ maps the interference between the incident fields onto the probabilities (see Appendix C1)

$$p_\pm(\delta) = \frac{1}{2}(1 \pm \mathrm{Re}[e^{i\delta}\left\langle\varphi\right| \hat{\Pi}\, \hat{D}(\alpha)\rho\hat{D}^\dagger(\alpha) \left|\varphi\right\rangle]). \tag{5.2.2}$$

Here, the photonic modes are traced out, and $\hat{\Pi}$ acts as the photon parity operator. Acknowledging the unusual expression, we note that it relates atomic coherences to the complex value overlap of the photonic states, that can be expressed as

$$\left\langle\varphi\right| \hat{\Pi}\, \hat{D}(\alpha)\rho\hat{D}^\dagger(\alpha) \left|\varphi\right\rangle = \langle\hat{\sigma}_x\rangle - i\,\langle\hat{\sigma}_y\rangle\,, \tag{5.2.3}$$

which is determined exclusively from measurements of the control atom. Phase δ provides access to the *real* and *imaginary* components of this quantity. As we shall see, this expression contains all the information about the state ρ.

5.3 P and Q quasiprobability measurements

Now, we outline protocols that provide direct access to phase-space representations of ρ via suitable choices of the displacement parameter α and probe states. The Husimi Q function [77], one of the most widely used quasiprobability distributions due to its favorable analytical and experimental properties [94, 95, 99, 104, 105], can be measured by choosing the probe state $|\varphi\rangle = |0\rangle$ and the coherent displacement $\alpha = -\gamma$, yielding

$$\langle\gamma|\,\rho\,|\gamma\rangle = p_+(0) - p_-(0), \tag{5.3.1}$$

which is the Q function, multiplied by $\pi/2$, at the phase space point γ. This protocol is analogous to the well-known *swap* test [106, 107, 108].

Similarly, the Glauber–Sudarshan P function is the Fourier transform of the matrix element $\langle-\gamma|\,\rho\,|\gamma\rangle$ [109]. Its negativities or singular features constitute clear signatures of nonclassicality, while its robustness against detection losses [110] makes it a useful witness of quantumness. Simultaneously, its potentially singular character makes experimental reconstruction notoriously challenging [111, 112]. Within our protocol, setting the displacement $\alpha = 0$ and the probe state $|\varphi\rangle = |\gamma\rangle$ yields the kernel

$$\langle-\gamma|\,\rho\,|\gamma\rangle = \langle\hat{\sigma}_x\rangle - i\,\langle\hat{\sigma}_y\rangle\,. \tag{5.3.2}$$

In contrast to the Husimi Q-function case, the parity operator here plays a crucial role, since it provides the π-rotation of γ in $\langle-\gamma|$.

5.4 Wavefunction measurements

With minor modifications, we can define a protocol for the direct measurement of the wavefunction of an unknown input pure state $|\psi\rangle$. The protocol starts by choosing a coherent probe state $|\beta/2\rangle$ and coherently displacing the input state by $\beta/2-\gamma$, with γ phase-aligned with respect to β, to simplify the implementation.

By measuring the control atom according to Eq. (5.2.2), one can estimate

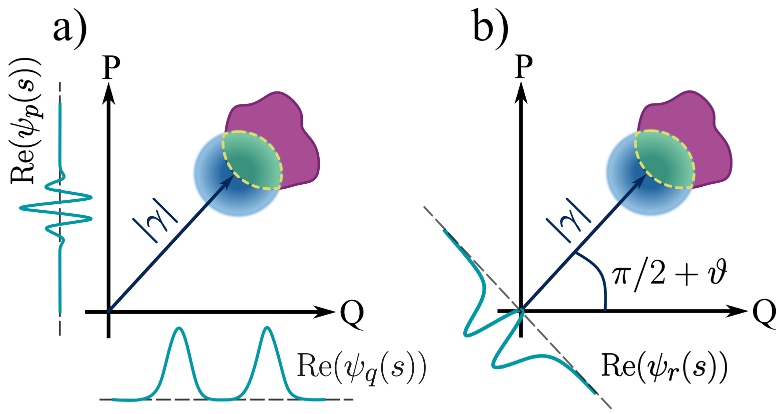

Figure 5.4.1: (a) Real part of the projection of the probe state (coherent state in blue) and unknown input state (purple) in the q and p representation. The imaginary part can also be obtained (not shown). (b) Real part of the projection of the probe state (coherent state in blue) and unknown input state (purple) in representation r.

the value $Z_\beta = \langle\gamma|\,\hat{D}(\beta)\,|\psi\rangle\,\langle\psi|\gamma\rangle$ (see Appendix C1). Performing the estimation twice, once for $\beta = 0$ and $\beta \neq 0$ one finds

$$\langle\gamma|\,\hat{D}(\beta)\,|\psi\rangle = \frac{Z_\beta}{\sqrt{Z_0}}e^{-i\phi_0}. \tag{5.4.1}$$

The wavefunction of $|\psi\rangle$ can be obtained by tuning the parameter $\beta = it\,e^{i\vartheta}/\sqrt{2}$, with t being a real scanning parameter and ϑ being a conveniently fixed parameter. This quantity can be expressed as the overlap

$$\langle\gamma|\,\hat{D}(it\,e^{i\vartheta}/\sqrt{2})\,|\psi\rangle = \int \gamma_r^*(s)e^{its}\psi_r(s)ds, \tag{5.4.2}$$

where $\psi_r(s) = \langle r_\vartheta|\psi\rangle$ and $\gamma_r(s) = \langle r_\vartheta|\gamma\rangle$ denote the wavefunctions of the input and probe states, respectively, in the rotated quadrature representation $|r_\vartheta\rangle = e^{i\vartheta\hat{n}}\,|q\rangle$ which is the eigenstate of $\hat{R}_\vartheta = \hat{Q}\cos\vartheta + \hat{P}\sin\vartheta$, with the canonical quadrature operators $\hat{Q} = (\hat{a}+\hat{a}^\dagger)/\sqrt{2}$ and $\hat{P} = i(\hat{a}^\dagger - \hat{a})/\sqrt{2}$.

Equation (5.4.2) is the inverse Fourier transform [113, 114, 115] of the product of wavefunctions with respect to variable t. Upon applying a Fourier transform to the measurement in t, we obtain (see Appendix C1)

$$F[\langle\gamma|\,\hat{D}(ite^{i\vartheta}/\sqrt{2})\,|\psi\rangle](\omega) = \sqrt{2\pi}\gamma_r^*(\omega)\psi_r(\omega), \tag{5.4.3}$$

which directly provides $\psi_r(\omega)$, as $\gamma_r(\omega)$ is known.

By scanning β and applying Eq. (5.4.3), the wavefunction is reconstructed up to the global phase ϕ_0. A schematic representation of the protocol is shown in Fig. 5.4.1, which enables full state characterization directly at the wavefunction level.

5.5 Wigner function measurement

By adding a second QM, we propose a protocol that enables the direct measurement of the Wigner function for an arbitrary mixed input state ρ.

The protocol starts by coherently displacing the input state by a known quantity α, which defines a given point in the phase space, while the probe field remains in the vacuum state. As before, the control atom is initialized in the state $|+\rangle_a$, as shown in Fig. 5.5.1. Both quantum mirrors should be controlled using the same atomic state. This can be achieved with a single atom controlling both mirrors, two entangled atoms each controlling a separate mirror, or a single control atom in a single QM upon reinjecting the same photonic modes back into the system. Finally, a measurement is performed on the state $|\pm\rangle_a$, yielding the probabilities

$$p_{\pm} = \frac{1}{2}\left(1 \pm \mathrm{Tr}\left[\rho \hat{D}^{\dagger}(\alpha)\hat{\Pi}\hat{D}(\alpha)\right]\right). \tag{5.5.1}$$

Thus, the Wigner function [116] is explicitly obtained as

$$W(\alpha) = \frac{2}{\pi}\Big(p_{+}(\alpha) - p_{-}(\alpha)\Big). \tag{5.5.2}$$

This expression has also been obtained in the reconstruction of a field contained in a cavity [95]. In our case, the expression above applies to a propagating field and, unlike other approaches, does not require photon counting [117].

It is worth noting that the Wigner function of a pure state $\rho = |\psi\rangle\langle\psi|$ can also be measured using only a single QM, provided that a copy of the state is introduced as a probe into the setup in Fig. 5.2.1. The probe state must be $|\varphi\rangle = \hat{D}(\alpha)\,|\psi\rangle$, allowing the measurement of the quantity $\langle\psi|\,\hat{D}(\alpha)\hat{\Pi}\hat{D}^{\dagger}(\alpha)\,|\psi\rangle$, which is proportional to the Wigner function of $|\psi\rangle$.

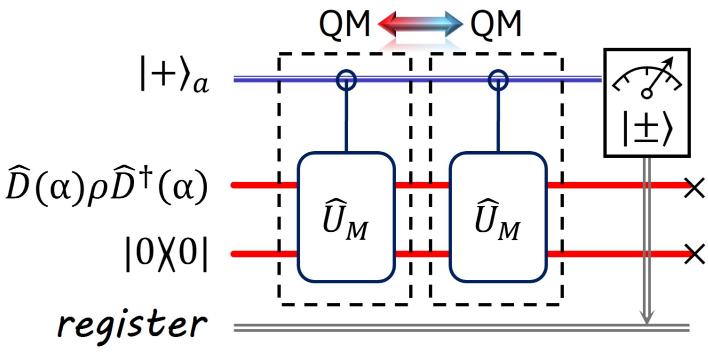

Figure 5.5.1: Direct measurement of the Wigner function of the unknown input state ρ at phase space point α, represented as a quantum circuit. The setup incorporates a second quantum mirror, which may equivalently be realized by re-injecting the modes into the same QM.

5.6 Experimental feasibility

A quantum mirror has been recently demonstrated [118], where tunable reflectivity was enabled by strong dipolar Rydberg interactions. This provided validation for the theoretical proposals [101, 119].

To the best of our knowledge, there are no studies on the relative phase ϕ between the reflected and transmitted output fields. This is the last key ingredient for implementing any of the previously mentioned protocols, as detailed in the Appendix C1. Previous studies have shown that the phase of the transmission and reflection coefficients can be modified by engineering the susceptibility of the medium [120], controlling the population of the relevant atomic levels [121], considering different geometries [122, 123], or alternatively, by adjusting the polarization and angle of incidence [124], which allows for phase modulation while preserving the magnitude of t and r. These works provide a direct route to the experimental control of ϕ by tuning the phase of either coefficient. Moreover, this phase can be measured using homodyne detection [125]. Together, these considerations place our proposal within the reach of current experimental capabilities.

Notably, the protocols presented here are not exclusive to atomically thin metamaterials but can also be realized in nanofibers [126, 127], conducting nanowires [128], and cavity-atom systems [129, 130, 131].

5.7 Analysis and discussion

QMs offer several significant advantages for CV-QST applications. The interference between the input photonic modes is mapped onto the coherences of the atom, which notably enables the measurement of freely propagating photonic states. Moreover, these protocols are robust against phase mismatches between the probe and input photonic fields, as shown in Fig. 5.2.1. In addition, the ability to obtain all the information of a field confirms the ability to directly measure the wavefunction, along with the formerly discussed known quasiprobability functions, but is not limited to those [132].

From a technical standpoint, these protocols offer a major advancement in measuring propagating states, comparable to weak measurement protocols [100, 133], allowing the characterization of quantum states through the measurement of the control atom. A thorough robustness analysis of the presented protocols is beyond the scope of this study, as it would require details of platform-specific experimental parameters and errors. Furthermore, this advancement shows promise for characterizing intense/macroscopic quantum fields, which are known for their rapidly scalable complexity in QST protocols, thus opening a unique window for metrology at the Heisenberg limit and for robust quantum information processing.

5.8 Conclusions

In this chapter, we developed a family of quantum state tomography protocols based on quantum mirrors for propagating continuous-variable quantum states. By mapping the interference between two optical modes onto the coherences of a control atom, these protocols reconstruct arbitrary unknown states while providing direct access to the wavefunction and a broad class of quasiprobability distributions, in several cases without requiring prior information or numerical reconstruction.

By transferring the characterization of propagating optical fields to the well-established toolbox of two-level atom tomography, this approach overcomes several limitations of conventional homodyne detection, including photodetection inefficiency, mode mismatch, bandwidth limitations, and electronic noise, while remaining robust against phase mismatches between the probe and the unknown field.

More generally, these results extend the scope of continuous-variable tomography beyond standard quasiprobability distributions to more general phase-space representations. Their applicability to highly nonclassical and high-energy optical states establishes quantum mirrors as a promising platform for benchmarking, verification, and quantum metrology, with concepts that may also be extended to other interfaces, such as superconducting quantum circuits.

Chapter 6

Conclusions and outlook

Taken together, the results presented in this thesis provide a unified perspective on the role of light–matter interactions in continuous-variable quantum information science. We first showed that photon-number nonlinearities constitute a universal mechanism through which coherent states naturally evolve into highly non-Gaussian states, establishing the emergence of nonclassicality as a general consequence of nonlinear optical evolution. Building upon this understanding, we demonstrated how nonlinear interactions can be harnessed to deterministically engineer specific nonclassical resources, namely high-fidelity multi-photon-added coherent states, using a driven Kerr resonator. Finally, we introduced a family of quantum mirror-based tomography protocols that enable the efficient characterization of propagating continuous-variable quantum states through atomic measurements, overcoming several limitations of conventional approaches.

Beyond their individual contributions, these studies illustrate how nonlinear light–matter interactions can be exploited throughout the entire lifecycle of nonclassical optical states: from understanding their physical origin, to engineering them in a controlled manner, and ultimately to their efficient characterization. In this way, the work presented in this thesis advances the understanding of the emergence, engineering, and efficient characterization of nonclassical states of light, providing new tools for continuous-variable quantum information, quantum metrology, and future quantum technologies.

Appendix A

A1 Variance of generalized coherent states

To obtain the variance of a GCS, we first calculate the following expectation values of the creation and annihilation operators:

$$
\begin{aligned}
\langle \hat{a} \rangle &= \langle \alpha | \, e^{i\theta t \hat{n}^{\epsilon}} \hat{a} e^{-i\theta t \hat{n}^{\epsilon}} \, | \alpha \rangle = \alpha \, \langle \alpha | \, e^{-i\theta t \{(\hat{n}+1)^{\epsilon} - \hat{n}^{\epsilon}\}} \, | \alpha \rangle \\
&= \alpha \sum_n C_n^2 e^{-i\theta t \{(n+1)^{\epsilon} - n^{\epsilon}\}}, \\
\left\langle \hat{a}^{\dagger} \right\rangle &= \alpha^* \sum_n C_n^2 e^{i\theta t \{(n+1)^{\epsilon} - n^{\epsilon}\}}, \\
\left\langle \hat{a}^2 \right\rangle &= \langle \alpha | \, e^{i\theta t \hat{n}^{\epsilon}} \hat{a}^2 e^{-i\theta t \hat{n}^{\epsilon}} \, | \alpha \rangle = \alpha^2 \, \langle \alpha | \, e^{-i\theta t \{(\hat{n}+2)^{\epsilon} - \hat{n}^{\epsilon}\}} \, | \alpha \rangle \\
&= \alpha^2 \sum_n C_n^2 e^{-i\theta t \{(n+2)^{\epsilon} - n^{\epsilon}\}}, \\
\left\langle \hat{a}^{\dagger 2} \right\rangle &= \alpha^{*2} \sum_n C_n^2 e^{i\theta t \{(n+2)^{\epsilon} - n^{\epsilon}\}},
\end{aligned}
$$

with $C_n^2 = |\langle \alpha | n \rangle|^2$, and where we used the relation $\hat{a} f(\hat{n}) = f(\hat{n}+1)\hat{a}$, with $f(\hat{n})$ an arbitrary function of the number operator [134].

Considering the generalized quadrature operator and its square

$$
\begin{aligned}
\hat{X}_{\phi} &= \hat{a} e^{-i\phi} + \hat{a}^{\dagger} e^{i\phi}, \\
\hat{X}_{\phi}^2 &= \hat{a}^2 e^{-2i\phi} + \hat{a}^{\dagger 2} e^{2i\phi} + 2\hat{n} + 1,
\end{aligned}
$$

we compute their expectation values as

$$
\begin{aligned}
\left\langle \hat{X}_{\phi} \right\rangle &= 2Re \left[\alpha \sum_n C_n^2 e^{-i\theta t \{(n+1)^{\epsilon} - n^{\epsilon}\}} e^{-i\phi} \right] \\
&= 2 \sum_n C_n^2 Re \left[\alpha e^{-i\theta t \{(n+1)^{\epsilon} - n^{\epsilon}\}} e^{-i\phi} \right], \qquad \text{(A1.1)} \\
\left\langle \hat{X}_{\phi}^2 \right\rangle &= 2 \sum_n C_n^2 Re \left[\alpha^2 e^{-i\theta t \{(n+2)^{\epsilon} - n^{\epsilon}\}} e^{-2i\phi} \right] + 2|\alpha|^2 + 1. \qquad \text{(A1.2)}
\end{aligned}
$$

Defining $z_{n,j}(t) = e^{-i\theta t \{(n+j)^{\epsilon} - n^{\epsilon}\}}$ we can write the expectations values of $\hat{X}_{\phi}$

and $\hat{X}_\phi^2$ as

$$\left\langle \hat{X}_\phi \right\rangle = 2\sum_n C_n^2 \mathrm{Re}\left[\alpha z_{n,1}(t) e^{-i\phi}\right], \tag{A1.3}$$

$$\begin{aligned}\left\langle \hat{X}_\phi^2 \right\rangle &= 2\sum_n C_n^2 \mathrm{Re}\left[\alpha^2 z_{n,2}(t) e^{-2i\phi}\right] + 2|\alpha|^2 + 1 \\ &= 4\sum_n C_n^2 \mathrm{Re}[\alpha z_{n,2}^{1/2}(t) e^{-i\phi}]^2 + 1. \end{aligned} \tag{A1.4}$$

Combining both terms, the variance is given by

$$\left\langle (\Delta \hat{X}_\phi)^2 \right\rangle = 4\left\langle \mathrm{Re}[\alpha z_{n,2}^{1/2}(t) e^{-i\phi}]^2 \right\rangle_\alpha - 4\left\langle \mathrm{Re}\left[\alpha z_{n,1}(t) e^{-i\phi}\right]\right\rangle_\alpha^2 + 1. \tag{A1.5}$$

In the particular case we analyze in the main text, we consider α real and $\phi = 0$, obtaining

$$\left\langle (\Delta \hat{X})^2 \right\rangle = 4\alpha^2 \left\{ \left\langle \mathrm{Re}[z_{n,2}^{1/2}(t)]^2 \right\rangle_\alpha - \left\langle \mathrm{Re}\left[z_{n,1}(t)\right]\right\rangle_\alpha^2 \right\} + 1. \tag{A1.6}$$

Appendix B

B1 Remnant photon number

In this section, we provide the derivation of the *remnant photon number*. Consider a general bosonic state $|\psi\rangle$ and a complex displacement parameter $z = x + iy$. The mean photon number after applying the displacement $\hat{D}(z)$ is

$$\begin{aligned} n(z) &= \langle\psi| \hat{D}^\dagger(z)\hat{n}\hat{D}(z) |\psi\rangle \\ &= x^2 + y^2 + 2x\langle\hat{x}\rangle + 2y\langle\hat{p}\rangle + \langle\hat{x}^2\rangle + \langle\hat{p}^2\rangle - 1/2, \end{aligned} \tag{B1.1}$$

where $\hat{x} = (\hat{a} + \hat{a}^\dagger)/2$ and $\hat{p} = (\hat{a} - \hat{a}^\dagger)/2i$ are the field quadrature operators. Minimizing $n(z)$ with respect to x and y yields the critical point $x_c = -\langle\hat{x}\rangle, y_c = -\langle\hat{p}\rangle$, corresponding to a displacement that shifts the state to the origin of phase space. Substituting these values back into $n(z)$, we obtain the remnant photon number

$$n_r = \langle\hat{x}^2\rangle - \langle\hat{x}\rangle^2 + \langle\hat{p}^2\rangle - \langle\hat{p}\rangle^2 - 1/2, \tag{B1.2}$$

which quantifies the residual photon number associated with intrinsic quantum fluctuations after optimal displacement.

In the case of a general quadrature $\hat{x}_\theta = \hat{x}\cos\theta + \hat{p}\sin\theta$, one can verify the conserved quantities

$$\langle\hat{x}_\theta^2\rangle + \langle\hat{x}_{\theta+\pi/2}^2\rangle = \langle\hat{x}^2\rangle + \langle\hat{p}^2\rangle, \tag{B1.3}$$

reflecting energy conservation under phase-space rotations, and

$$\langle\hat{x}_\theta\rangle^2 + \langle\hat{x}_{\theta+\pi/2}\rangle^2 = \langle\hat{x}\rangle^2 + \langle\hat{p}\rangle^2, \tag{B1.4}$$

corresponding to the invariance of the mean amplitude under phase-space rotations. Combining these results, the remnant photon number takes the form

$$n_r = \langle\hat{x}_\theta^2\rangle - \langle\hat{x}_\theta\rangle^2 + \langle\hat{x}_{\theta+\pi/2}^2\rangle - \langle\hat{x}_{\theta+\pi/2}\rangle^2 - 1/2, \tag{B1.5}$$

which shows explicitly that n_r is invariant under the phase-space direction in which it is probed, as discussed in the main text. This invariance highlights that n_r is a basis-independent quantity, determined solely by intrinsic quantum fluctuations. Consequently, it provides a physically meaningful ordering of non-classicality.

B2 Photon-number matching condition

As discussed in the main text, the state $|\Psi(t)\rangle = \hat{D}(\zeta)\hat{D}(-\gamma)\,|\psi(t)\rangle$ resembles the photon added coherent state (PACS) $|\alpha, n\rangle$, where $\gamma = \langle\hat{x}\rangle + i\langle\hat{p}\rangle$. We therefore impose, as a physically motivated constraint, that the displaced state $\hat{D}(-\gamma)\,|\psi(t)\rangle$ at the relevant evolution time and the displaced PACS $\hat{D}(-\zeta)\,|\alpha, n\rangle$ should have the same mean number of photons. Writing $\alpha = |\alpha|e^{i\phi}$ and $\zeta = |\zeta|e^{i\phi}$ so that both amplitudes share the same phase ϕ, this condition reads

$$\begin{aligned}\langle\psi(t)|\,\hat{D}(\gamma)\hat{n}\hat{D}^\dagger(\gamma)\,|\psi(t)\rangle &= n_r\big(|\psi(t)\rangle\big)\\ &= \langle\alpha, n|\,\hat{D}(\zeta)\hat{n}\hat{D}^\dagger(\zeta)\,|\alpha, n\rangle\\ &= \langle\alpha, n|\,\hat{a}\hat{a}^\dagger - 1 - |\zeta|(\hat{a}e^{-i\phi} + \hat{a}^\dagger e^{i\phi}) + |\zeta|^2\,|\alpha, n\rangle\\ &= \frac{N_{n+1}}{N_n} - 2|\zeta|\langle\hat{x}_\phi\rangle_{\alpha,n} + |\zeta|^2 - 1\end{aligned} \tag{B2.1}$$

where $\langle\hat{x}_\phi\rangle_{\alpha,n} = |\alpha|L_n^{(1)}(-|\alpha|^2)/L_n(-|\alpha|^2)$ with $L_n^{(1)}(x)$ and $L_n(x)$ denoting the associated and ordinary Laguerre polynomials [55], respectively. This expression follows from the results derived in Ref. [66] under the condition $\arg(\alpha) = \arg(\zeta) = \phi$.

Equation (B2.1) can also be used to determine the remnant photon number of the PACS itself. Minimizing the right-hand side with respect to $|\zeta|$ yields the optimal displacement $|\zeta|_{opt} = \langle\hat{x}_\phi\rangle_{\alpha,n}$, from which we obtain

$$n_r(|\alpha, n\rangle) = \frac{N_{n+1}}{N_n} - \langle\hat{x}_\phi\rangle^2_{\alpha,n} - 1, \tag{B2.2}$$

whose behavior can be seen in Fig. B2.1. Finally, solving Eq. (B2.1) for $|\zeta|$ gives

$$\begin{aligned}|\zeta| &= \langle\hat{x}_\phi\rangle_{\alpha,n} \pm \sqrt{\langle\hat{x}_\phi\rangle^2_{\alpha,n} - \frac{N_{n+1}}{N_n} + 1 + n_r\big(|\psi(t)\rangle\big)}\\ &= \langle\hat{x}_\phi\rangle_{\alpha,n} \pm \sqrt{n_r\big(|\psi(t)\rangle\big) - n_r(|\alpha, n\rangle)}.\end{aligned} \tag{B2.3}$$

This expression establishes the relation between the displacement amplitude $|\zeta|$ and the difference between the remnant photon numbers of the evolved state and the corresponding PACS.

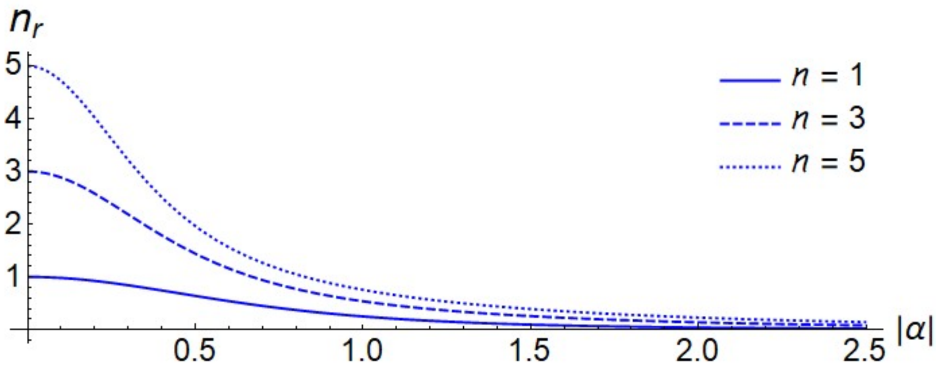

Figure B2.1: Remnant photon number n_r of the photon-added coherent state $|\alpha, n\rangle$ as a function of the coherent amplitude $|\alpha|$ for different photon-addition numbers n. At $|\alpha| = 0$, the remnant photon number coincides with the photon number of the corresponding Fock state. As $|\alpha|$ increases, n_r decreases monotonically and approaches zero in the large amplitude limit, where the state resembles a coherent state. Larger values of n yield higher remnant photon numbers, reflecting the enhanced nonclassicality induced by photon addition.

B3 Physical Interpretation of the Condition $\delta = 2\chi$

The condition $\delta = 2\chi$ plays a central role in the emergence of PACS-like structures as a spectral constraint that preserves the intrinsic phase organization of the Kerr system. This condition is satisfied when the field linear evolution frequency δ coincides with the smallest Kerr evolution frequency 2χ. As a consequence, the periodicity of the linear evolution matches the periodicity of the nonlinear evolution.

The effective Fock-state energies of the driven Kerr Hamiltonian are

$$E_n = \hbar\delta n + \hbar\chi n(n-1), \tag{B3.1}$$

with level spacings

$$E_{n+1} - E_n = \hbar(\delta + 2\chi n). \tag{B3.2}$$

For zero detuning ($\delta = 0$), the states $|0\rangle$ and $|1\rangle$ are degenerate. The condition $\delta = 2\chi$ removes this low-energy degeneracy while preserving the characteristic

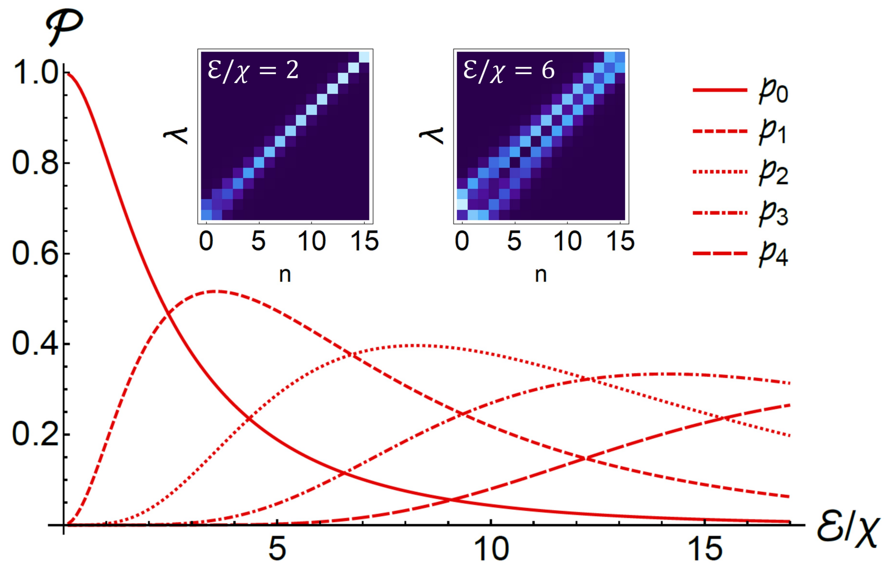

Figure B3.1: Spectral decomposition probabilities $p_n = |\langle\lambda_n|0\rangle|^2$ of the vacuum state projected onto the eigenstates $|\lambda_n\rangle$ of the Hamiltonian $\mathcal{H}_R$ as a function of the ratio $\mathcal{E}/\chi$. In the weak-driving regime, the vacuum state is predominantly composed of the lowest-energy eigenstates. As the ratio $\mathcal{E}/\chi$ increases, a larger number of eigenstates contributes significantly to the decomposition, resulting in a broader spectral distribution. The insets show the Fock-basis representation of the eigenstates for $\mathcal{E}/\chi = 2$ and $\mathcal{E}/\chi = 6$, respectively. For weak driving, the eigenstates remain strongly localized near the diagonal, whereas stronger driving leads to a broader distribution over Fock states, reflecting the increasing complexity of the dressed-state structure.

quadratic Kerr structure, yielding

$$E_n = \hbar\chi n(n+1). \tag{B3.3}$$

The dynamics retains the intrinsic Kerr structure, but with a reordered low-energy ladder free from the $|0\rangle$–$|1\rangle$ degeneracy.

The coherent drive,

$$\hat{H}_{drive} = \hbar\mathcal{E}(\hat{a} + \hat{a}^\dagger), \tag{B3.4}$$

induces sequential transitions between neighboring Fock states with a given phase. The resulting dynamics is therefore governed by the interplay between driven transitions and Kerr-induced phase evolution. Since the condition $\delta = 2\chi$ preserves the monotonic Kerr ladder structure, the driven transitions can interfere constructively over time, favoring partial rephasing of low-lying Fock components and the emergence of structured nonclassical states.

B4 Spectral and Dynamical Properties of the System

In the main text, the Hamiltonian governing the time evolution of the system is given by

$$\mathcal{H} = \hbar\omega_0 \hat{a}^\dagger \hat{a} + \hbar\mathcal{E}\left(\hat{a}\ e^{i\omega_d t} + \hat{a}^\dagger e^{-i\omega_d t}\right) + \hbar\chi \hat{a}^{\dagger 2}\hat{a}^2, \tag{B4.1}$$

where ω_0 is the cavity frequency, ω_d is the driving frequency, $\mathcal{E}$ denotes the driving amplitude and χ characterizes the Kerr nonlinearity. Transforming into the rotating frame defined by $R(t) = e^{-i\omega_d \hat{a}^\dagger \hat{a} t}$, the Hamiltonian becomes

$$\mathcal{H}_R = R\,\mathcal{H}R^{-1} + i\hbar(\partial_t R)R^{-1} = \hbar\delta\, \hat{a}^\dagger \hat{a} + \hbar\mathcal{E}\left(\hat{a} + \hat{a}^\dagger\right) + \hbar\chi\, \hat{a}^{\dagger 2}\hat{a}^2, \tag{B4.2}$$

where $\delta = \omega_0 - \omega_d = 2\chi$ is the selected detuning between the cavity and driving frequencies. Due to the nonlinear nature of the system, analytical expressions for the eigenstates are generally not available. Denoting the eigenstates and eigenvalues of $\mathcal{H}_R$ by $|\lambda_j\rangle$ and λ_j, respectively, the initial vacuum state can be expanded as

$$|\psi(0)\rangle = |0\rangle = \sum_j c_j \,|\lambda_j\rangle\,. \tag{B4.3}$$

As shown in Fig. B3.1, the vacuum state is represented by a finite superposition of these eigenstates with probabilities $p_j = |c_j|^2$. As the ratio $\mathcal{E}/\chi$ increases, a larger number of eigenstates contributes significantly to the decomposition. In the weak-driving regime, the dominant eigenstates themselves involve only a few Fock components, typically no more than three. In contrast, for larger values of $\mathcal{E}/\chi$, the structure of the eigenstates becomes increasingly delocalized in the Fock basis, as illustrated in the insets of Fig. B3.1.

Moreover, since the Hamiltonian $\mathcal{H}_R$ is represented by a real symmetric matrix in the Fock basis, its eigenvalues λ_j are real and its eigenvectors $|\lambda_j\rangle$ can be chosen with purely real coefficients. Consequently, the overlaps $c_j = \langle\lambda_j|0\rangle$ are also real quantities. The state of the system at time t is therefore given by

$$|\psi(t)\rangle = \sum_j \langle\lambda_j|0\rangle\, e^{-i\lambda_j t}\,|\lambda_j\rangle\,. \tag{B4.4}$$

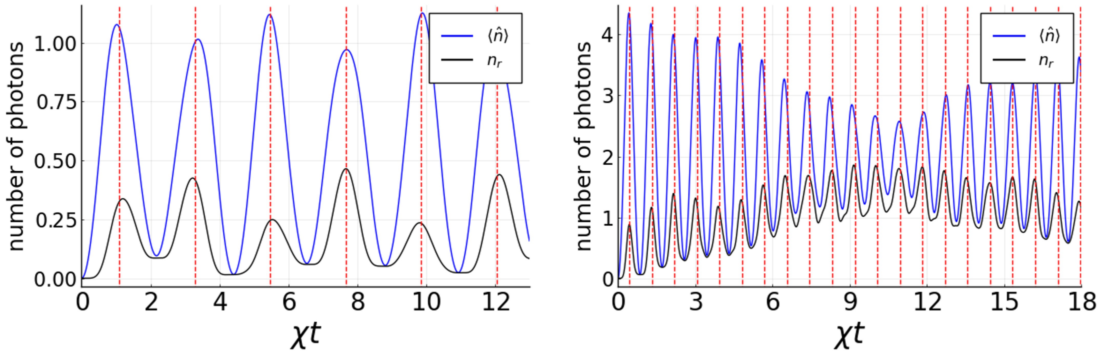

Figure B4.1: Time evolution of the mean photon number $\langle \hat{n}(t) \rangle$ (blue curves) and the remnant photon number n_r (black curves) for two different driving regimes $\mathcal{E}/\chi = \{1.5, 6.5\}$. The vertical dashed red lines indicate the characteristic oscillation period determined by the dominant energy splitting $(\lambda_m - \lambda_n)$ arising from the interference between the two most relevant dressed eigenstates in the spectral decomposition of the initial vacuum state. In the weak-driving regime (left panel), the dynamics are governed by a small number of eigenstates, leading to nearly periodic oscillations with low photon occupation and a comparatively small remnant photon number. In the stronger-driving regime (right panel), a larger number of dressed eigenstates contributes to the dynamics, producing higher photon populations and more complex oscillatory behavior. The remnant photon number remains systematically smaller than $\langle \hat{n}(t) \rangle$, reflecting the removal of the coherent displacement contribution.

The expectation value of the photon number operator then reads

$$\begin{aligned} \langle \hat{n}(t) \rangle &= \sum_{j,k} \langle 0|\lambda_k\rangle \langle \lambda_j|0\rangle \, e^{i(\lambda_k - \lambda_j)t/\hbar} \langle \lambda_k| \, \hat{n} \, |\lambda_j\rangle \\ &= \sum_{j} |\langle 0|\lambda_j\rangle|^2 \langle \lambda_j| \, \hat{n} \, |\lambda_j\rangle + \sum_{j\neq k} \langle 0|\lambda_k\rangle \langle \lambda_j|0\rangle \langle \lambda_k| \, \hat{n} \, |\lambda_j\rangle \cos[(\lambda_k - \lambda_j)t] \, . \end{aligned} \tag{B4.5}$$

Here we have used the fact that the matrix elements $\langle \lambda_k| \, \hat{n} \, |\lambda_j\rangle$ are real. The first term describes the static contribution arising from the populations of the dressed eigenstates, while the second term encodes coherent oscillations generated by quantum interference between different eigenstates. The oscillation frequencies are determined by the energy differences $(\lambda_k - \lambda_j)$, revealing the spectral structure of the driven nonlinear system.

A particularly relevant situation occurs when the dynamics are dominated by two eigenstates, $|\lambda_m\rangle$ and $|\lambda_n\rangle$. In this case, the photon-number mean value can be approximated as

$$\langle \hat{n}(t) \rangle = p_m \langle \lambda_m | \hat{n} | \lambda_m \rangle + p_n \langle \lambda_n | \hat{n} | \lambda_n \rangle + 2 \langle 0 | \lambda_m \rangle \langle \lambda_n | 0 \rangle \langle \lambda_m | \hat{n} | \lambda_n \rangle \cos[(\lambda_m - \lambda_n)t] \,. \tag{B4.6}$$

The dynamics are therefore characterized by a dominant oscillation period $2\pi/(\lambda_m - \lambda_n)$. This characteristic timescale is highlighted by the vertical red lines in Fig. B4.1. Additionally, it is worth to mention that the system is initially prepared in the vacuum state, then one has $\langle \hat{n}(0) \rangle = 0$. Consequently, the interference contribution must compensate the positive diagonal terms at $t = 0$, implying that $\langle 0 | \lambda_m \rangle \langle \lambda_n | 0 \rangle \langle \lambda_m | \hat{n} | \lambda_n \rangle < 0$. As a result, the photon number reaches its maximum value when $(\lambda_m - \lambda_n)t = \pi$.

B5 Weak-Driving Regime Analysis

To gain analytical insight into the generation of PACS, we now focus on the weak-driving regime. In this limit, the dynamics is dominated by a small number of low-excitation Fock states, enabling a perturbative description of both the dressed eigenstates and the resulting time evolution. This regime is particularly relevant because it is precisely where the highest fidelities are obtained, as shown in Fig. B5.1(b), making it especially suitable for analytical treatment.

In order to apply perturbation theory, the driving amplitude must satisfy

$$\mathcal{E} \ll \frac{E_{n+1} - E_n}{\hbar} = \delta + 2\chi n, \tag{B5.1}$$

so that the dressed eigenstates can be approximated as

$$|n'\rangle = |n^{(0)}\rangle + |n^{(1)}\rangle + |n^{(2)}\rangle + \cdots \,. \tag{B5.2}$$

Up to first order, the corrections are given by

$$\begin{aligned} |n^{(0)}\rangle &= |n\rangle \,, \\ |n^{(1)}\rangle &= \mathcal{E} \sum_{k \neq n} \frac{\langle k | \hat{a} + \hat{a}^\dagger | n \rangle}{(\delta + \chi(n + k - 1))(n - k)} |k\rangle \\ &= \mathcal{E} \left(\frac{\sqrt{n}}{\delta + 2\chi(n-1)} |n-1\rangle - \frac{\sqrt{n+1}}{\delta + 2\chi n} |n+1\rangle \right) . \end{aligned} \tag{B5.3}$$

The first two dressed states provide the dominant contribution to the dynamics, since higher-order states do not contain a vacuum component at first order. They are therefore approximated by

$$|0'\rangle = \frac{1}{\sqrt{Z_0}}\left(|0\rangle - \frac{\mathcal{E}}{\delta}|1\rangle\right) \quad \text{and} \quad |1'\rangle = \frac{1}{\sqrt{Z_1}}\left(|1\rangle + \frac{\mathcal{E}}{\delta}|0\rangle - \frac{\mathcal{E}\sqrt{2}}{\delta+2\chi}|2\rangle\right), \tag{B5.4}$$

where Z_0 and Z_1 are their normalization constants. The state of the system at time t can be expanded in the basis $\{|n'\rangle\}$ as $|\psi(t)\rangle = \sum_n \langle n'|0\rangle\, e^{-i\lambda_n t}\, |n'\rangle$. Within the weak-driving approximation, the dynamics is mainly governed by the two lowest dressed states, yielding $|\psi(t)\rangle = \langle 0'|0\rangle\, e^{-i\lambda_0 t}\, |0'\rangle + \langle 1'|0\rangle\, e^{-i\lambda_1 t}\, |1'\rangle$. Substituting the perturbative expressions for $|0'\rangle$ and $|1'\rangle$, the evolved state in the Fock basis becomes

$$\begin{aligned} |\psi(t)\rangle = e^{-i\lambda_0 t}\Bigg[&\left(\frac{1}{Z_0} + \frac{\mathcal{E}^2}{Z_1\delta^2} e^{-i(\lambda_1-\lambda_0)t}\right)|0\rangle \\ &+ \left(\frac{\mathcal{E}}{Z_1\delta} e^{-i(\lambda_1-\lambda_0)t} - \frac{\mathcal{E}}{Z_0\delta}\right)|1\rangle \\ &- \frac{\mathcal{E}^2\sqrt{2}}{Z_1\delta(\delta+2\chi)} e^{-i(\lambda_1-\lambda_0)t}\,|2\rangle \Bigg] \end{aligned} \tag{B5.5}$$

As shown in Fig. B4.1, the remnant photon number is strongly correlated with the total photon number, indicating that the nonclassical behavior becomes maximal approximately when the photon population reaches its maximum value. Within the two dressed state approximation showed in Eq. (B4.6), this occurs when $(\lambda_1 - \lambda_0)t = \pi$. At this time, the evolved state reduces to

$$|\psi_\pi\rangle \propto -\left(\frac{1}{Z_0} - \frac{\mathcal{E}^2}{Z_1\delta^2}\right)|0\rangle + \frac{\mathcal{E}}{\delta}\left(\frac{1}{Z_0} + \frac{1}{Z_1}\right)|1\rangle - \frac{\mathcal{E}^2\sqrt{2}}{Z_1\delta(\delta+2\chi)}|2\rangle\,. \tag{B5.6}$$

We now derive an analytical approximation for the generated state in the weak-driving regime and we will compare it with the previous expression. The single photon added coherent state (SPACS), introduced in Ref. [66], is defined as

$$|\alpha, 1\rangle = \frac{\hat{a}^\dagger|\alpha\rangle}{\sqrt{N_1}}, \qquad N_1 = 1 + |\alpha|^2, \tag{B5.7}$$

where $|\alpha\rangle = \hat{D}(\alpha)|0\rangle$ is a coherent state. Applying an additional small

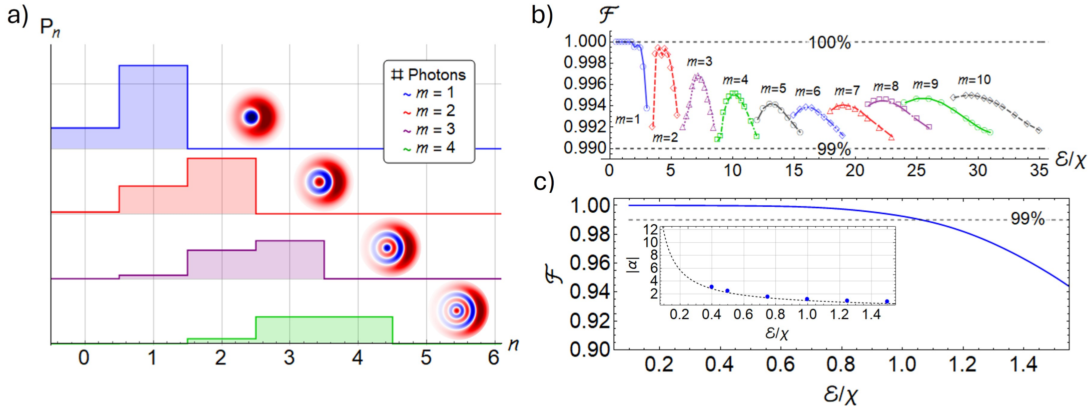

Figure B5.1: (a) Photon-number distribution P_n of the states $|\Gamma_{\alpha,m}\rangle$ for different photon-addition numbers m and coherent amplitude $\alpha = 0.5$. Each distribution is shifted vertically for clarity. As the number of added photons increases, the probability distribution moves toward higher photon-number sectors and becomes strongly concentrated around a characteristic maximum photon number, reflecting the photon-blockade structure induced by the nonlinear excitation process. The insets show the corresponding phase-space structure of the states, highlighting the increasing nonclassical character. (b) Fidelity $\mathcal{F}$ obtained from the numerical optimization between the dynamically generated states and the target photon-added coherent states as a function of the normalized driving strength $\mathcal{E}/\chi$ for photon-addition numbers up to $m = 10$ under the resonance condition $\delta = 2\chi$. Each curve identifies the parameter region where the dynamics most efficiently reproduces a given photon-added coherent state. The dashed horizontal line marks the 99% fidelity threshold. (c) Comparison between numerical and analytical results in the weak-driving regime for the single-photon-added coherent state. The blue curve corresponds to a fitted interpolation of the fidelities obtained between the numerically generated states and the analytical prediction as a function of $\mathcal{E}/\chi$. The inset shows the comparison between the numerically extracted coherent amplitude α (blue points) and the corresponding analytical weak-driving prediction (black dashed line).

displacement $\hat{D}(\gamma)$ gives

$$\hat{D}(\gamma)\,|\alpha,1\rangle = \frac{\hat{D}(\alpha)}{\sqrt{1+\alpha^2}}\hat{D}(\gamma)\,\overbrace{(\alpha\,|0\rangle + |1\rangle)}^{|\Gamma_{\alpha,1}\rangle}, \tag{B5.8}$$

where $|\Gamma_{\alpha,1}\rangle$ is a state only composed of two Fock states, as shown in Fig.B5.1.Expanding the displaced state up to first order in γ yields

$$\hat{D}(\gamma)\,|\Gamma_{\alpha,1}\rangle \approx \frac{1}{\sqrt{1+\alpha^2}}\left[(\alpha-\gamma)\,|0\rangle + (1+\alpha\gamma)\,|1\rangle + \gamma\sqrt{2}\,|2\rangle\right]. \tag{B5.9}$$

Comparing Eq. (B5.6) with the displaced SPACS expansion in Eq. (B5.9), we obtain the system

$$\begin{aligned}
\frac{\alpha-\gamma}{\sqrt{1+\alpha^2}} &= \frac{\mathcal{E}^2}{Z_1\delta^2}-\frac{1}{Z_0},\\
\frac{\gamma}{\sqrt{1+\alpha^2}} &= -\frac{\mathcal{E}^2}{Z_1\delta(\delta+2\chi)},\\
\frac{1+\alpha\gamma}{\sqrt{1+\alpha^2}} &= \frac{\mathcal{E}}{\delta}\left(\frac{1}{Z_0}+\frac{1}{Z_1}\right).
\end{aligned} \tag{B5.10}$$

Assuming $Z_1 \simeq Z_0$ and $\delta = 2\chi$, the system can be easily solved, yielding

$$\boxed{\alpha = -\frac{1-s}{\sqrt{3s(s+2)}}} \quad \text{and} \quad \boxed{\gamma = \frac{\alpha s}{1-s}}, \tag{B5.11}$$

where $s = (\mathcal{E}/\chi)^2/8$. These relations establish a direct correspondence between the driving strength and the effective PACS parameters, showing that the weak-driving regime reproduces a displaced SPACS structure. This accounts for the high fidelities in Fig. B5.1(b) and is quantitatively confirmed by the agreement with numerics in Fig. B5.1(c).

B6 Experimental robustness

In realistic experimental implementations, imperfections in the control parameters may affect the quality of the generated states. In particular, deviations in the evolution time and in the coherent displacement applied to reconstruct the target PACS can reduce the final fidelity. To quantify the robustness of the protocol, we analyze the fidelity landscape around the optimal preparation parameters.

Figure B6.1 shows the fidelity $\mathcal{F}$ between the generated state and the target photon-added coherent state as a function of relative variations in the displacement parameter, $\Delta\zeta$, and in the evolution time, Δt. As the photon-addition number increases, the high-fidelity region becomes progressively narrower. This behavior reflects the enhanced sensitivity of higher-order PACS to small perturbations in the preparation protocol. Since these states involve increasingly structured quantum interference between several Fock components, slight deviations in the accumulated dynamical phases or in the displacement amplitude can noticeably modify the resulting state.

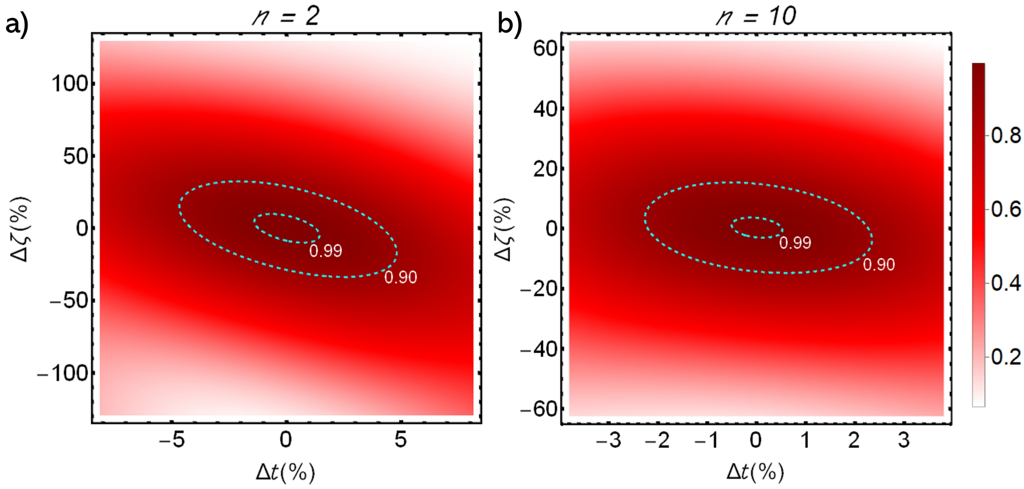

Figure B6.1: Density plots of the fidelity $\mathcal{F}$ as a function of relative deviations in the displacement parameter $\Delta\zeta$ and evolution time Δt for (a) $n = 2$ and (b) $n = 10$. The reference point $(\Delta t, \Delta\zeta) = (0, 0)$ corresponds to the optimal parameters maximizing the fidelity. The dashed cyan contours indicate fidelity thresholds of 0.90 and 0.99. In both cases, the fidelity remains high within a finite parameter region, demonstrating the robustness of the generated states against small deviations in the preparation protocol.

Appendix C

C1 Mode-Independent Beam Splitter Formalism

Consider a device in which the transmission and reflection coefficients are identical for both input ports (or equivalently, for both propagation directions). The relation between the input and output field modes can be expressed in terms of the symmetric transfer matrix

$$M = \begin{pmatrix} t & r \\ r & t \end{pmatrix}, \tag{C1.1}$$

where t and r denote the transmission and reflection coefficients, respectively. For an ideal (lossless) beam splitter, the input and output modes obey the bosonic commutation relations. Consequently, the matrix M is unitary, leading to the following conservation relations:

$$|t|^2 + |r|^2 = 1 \tag{C1.2}$$

$$r^*t + t^*r = 0. \tag{C1.3}$$

In general, these coefficients are complex numbers and can be written as $t = |t|e^{i\phi_t}$ and $r = |r|e^{i\phi_r}$. Using Eq. (C1.2) and Eq. (C1.3), the relation between r and t is often written in the simplified form $t - 1 = r$. However, this expression neglects the presence of a **global phase**, which is commonly considered physically irrelevant but plays a significant role in the present work. With this, the more general relation can be written as

$$t = r + e^{i\phi}. \tag{C1.4}$$

A **phase relation** for r and t can be derived from Eq. (C1.3); solving for the phase component

$$\phi_r - \phi_t = \pm\pi/2. \tag{C1.5}$$

A convenient **parameterization** for r and t can be obtained from $t = e^{i\phi} + |r|e^{i\phi_r}$. Starting from Eq. (C1.2), one arrives to

$$|r|(\cos(\phi - \phi_r) + |r|) = 0,$$

and the solutions for this equation are simply

$$|r| = 0 \quad \text{and} \quad |r| = -\cos(\phi - \phi_r), \tag{C1.6}$$

where $(\phi_r - \phi) \in [\pi/2, \pi]$ to ensure $|r| \geq 0$. Substituting the nontrivial solution into the expression for t, we obtain

$$t = -ie^{i\phi_r} \sin(\phi_r - \phi). \tag{C1.7}$$

Using these parameterized coefficients and introducing the change of variables $\phi_r - \phi = \theta + \frac{\pi}{2}$, $\theta \in [0, \pi/2]$. The transfer matrix M can be written as

$$M = e^{i(\phi+\theta)} \underbrace{\begin{pmatrix} \cos\theta & i\sin\theta \\ i\sin\theta & \cos\theta \end{pmatrix}}_{\in\ \mathrm{SU}(2)}. \tag{C1.8}$$

Since matrix M, without the exponential, belongs to the SU(2) group, we adopt the angular-momentum formalism for beam splitter devices, as introduced in Ref. [102]. Defining the operators

$$\hat{L}_1 = \frac{1}{2}\left(\hat{a}_0^\dagger \hat{a}_1 + \hat{a}_1^\dagger \hat{a}_0\right), \quad \hat{L}_2 = \frac{1}{2i}\left(\hat{a}_0^\dagger \hat{a}_1 - \hat{a}_1^\dagger \hat{a}_0\right), \quad \hat{L}_3 = \frac{1}{2}\left(\hat{a}_0^\dagger \hat{a}_0 - \hat{a}_1^\dagger \hat{a}_1\right), \tag{C1.9}$$

which leads to the unitary evolution corresponding to the lossless beam splitter associated with Eq. (C1.8) as

$$\hat{U}(\theta, \phi) = e^{-i(\theta+\phi)\hat{n}} e^{i\frac{\pi}{2}\hat{L}_3} e^{-2i\theta\hat{L}_2} e^{-i\frac{\pi}{2}\hat{L}_3} = e^{-i(\theta+\phi)\hat{n}} e^{-2i\theta\hat{L}_1} = e^{-i\left\{(\theta+\phi)\hat{n} + 2\theta\hat{L}_1\right\}}, \tag{C1.10}$$

where $\hat{n} = \hat{a}_0^\dagger \hat{a}_0 + \hat{a}_1^\dagger \hat{a}_1$ is the total photon number operator. The corresponding transformation of the field operators is given by

$$\hat{a}_0 \quad \to \hat{U}(\theta, \phi)\, \hat{a}_0\, \hat{U}^\dagger(\theta, \phi) = e^{i(\theta+\phi)}(\hat{a}_0 \cos\theta + i\hat{a}_1 \sin\theta), \tag{C1.11}$$

$$\hat{a}_1 \quad \to \hat{U}(\theta, \phi)\, \hat{a}_1\, \hat{U}^\dagger(\theta, \phi) = e^{i(\theta+\phi)}(i\hat{a}_0 \sin\theta + \hat{a}_1 \cos\theta). \tag{C1.12}$$

A particularly relevant case is obtained for $\theta = \pi/2$, which corresponds to a perfect mirror. Defining the mirror operator $\hat{U}_M = \hat{U}(\theta = \pi/2, \phi)$. Its action on an arbitrary two-mode state is

$$\begin{aligned}
\hat{U}_M |\psi\rangle_0 |\varphi\rangle_1 &= \hat{U}_M \left(\sum_n c_n \frac{\hat{a}_0^{\dagger n}}{\sqrt{n!}} \sum_m d_m \frac{\hat{a}_1^{\dagger m}}{\sqrt{m!}} \right) |0\rangle \\
&= \sum_n c_n \frac{(\hat{U}_M \hat{a}_0^\dagger \hat{U}_M^\dagger)^n}{\sqrt{n!}} \sum_m d_m \frac{(\hat{U}_M \hat{a}_1^\dagger \hat{U}_M^\dagger)^m}{\sqrt{m!}} \hat{U}_M |0\rangle \\
&= \sum_n c_n \frac{(-1)^n (e^{-i\phi n})(\hat{a}_{1'}^\dagger)^n}{\sqrt{n!}} \sum_m d_m \frac{(-1)^m (e^{-i\phi m})(\hat{a}_{0'}^\dagger)^m}{\sqrt{m!}} |0\rangle \\
&= e^{-i\phi \hat{n}_{0'}} \hat{\Pi}_{0'} |\varphi\rangle_{0'} e^{-i\phi \hat{n}_{1'}} \hat{\Pi}_{1'} |\psi\rangle_{1'}
\end{aligned} \tag{C1.13}$$

where $\hat{\Pi}_k = e^{i\pi \hat{n}_k}$ is the photon-parity operator associated with mode k and $|n\rangle$ is the Fock basis. Hence, each reflected field acquires the same phase shift ϕ and a parity operation. At this stage, the factors $e^{-i\phi\hat{n}_k}$ contribute only global phases to the individual modes and are therefore physically irrelevant in the absence of a relative phase.

C2 Parity operator manipulation

We define the unitary operation of the *quantum mirror* (QM) as a perfect mirror coherently controlled by a two-level system

$$\hat{U}_{QM} = \hat{\pi}_g \otimes \mathbf{1} \otimes \mathbf{1} + \hat{\pi}_e \otimes \hat{U}_M, \tag{C2.1}$$

where $\hat{\pi}_k = |k\rangle\langle k|$ denotes the projector onto the atomic basis $\{|g\rangle, |e\rangle\}$ and the operator $\hat{U}_M$ is defined as in Eq. (C1.13). In contrast to the previous situation, the phase factors associated with $\hat{U}_M$ are no longer global, as they appear as relative phases imprinted on the reflected-field modes conditioned on the atomic states $|g\rangle$ and $|e\rangle$. Consequently, these phases become physically observable through interference in the atomic degree of freedom.

Additional control over these phases can be achieved by introducing mode-dependent phase shifts $\{\varphi_0, \varphi_1, \varphi_2, \varphi_3\}$ before and after the QM interaction. These phases can be physically implemented using optical path-length differences or external phase shifters that act independently on each mode. The corresponding unitary operations are

$$e^{i(\varphi_0 \hat{n}_0 + \varphi_1 \hat{n}_1)} \qquad \text{and} \qquad e^{-i(\varphi_2 \hat{n}_0 + \varphi_3 \hat{n}_1)}, \tag{C2.2}$$

respectively. The resulting system operator is therefore

$$\begin{aligned} \hat{U}_S &= e^{-i(\varphi_2 \hat{n}_0 + \varphi_3 \hat{n}_1)}\, \hat{U}_{QM}\, e^{i(\varphi_0 \hat{n}_0 + \varphi_1 \hat{n}_1)}, \\ &= \hat{\pi}_g \otimes e^{i(\varphi_{in} - \varphi_{out})\hat{n}/2} e^{i(\Delta - \Delta')\hat{L}_3} \\ &\quad + \hat{\pi}_e \otimes e^{i(\varphi_{in} - \varphi_{out})\hat{n}/2} e^{-i\Delta' \hat{L}_3} \hat{U}_M\, e^{i\Delta \hat{L}_3}, \end{aligned} \tag{C2.3}$$

where we have introduced the phase sums and differences $\varphi_{in} = \varphi_0 + \varphi_1$, $\varphi_{out} = \varphi_2 + \varphi_3$, $\Delta = \varphi_0 - \varphi_1$ and $\Delta' = \varphi_2 - \varphi_3$. Factorizing the common terms yields

$$\hat{U}_S = \mathbf{1} \otimes e^{i(\varphi_{in} - \varphi_{out})\hat{n}/2} e^{i(\Delta - \Delta')\hat{L}_3} \left(\hat{\pi}_g \otimes \mathbf{1} \otimes \mathbf{1} + \hat{\pi}_e \otimes e^{-i\Delta \hat{L}_3}\, \hat{U}_M\, e^{i\Delta \hat{L}_3} \right). \tag{C2.4}$$

Without loss of generality, we set $\varphi_0 = \varphi_2$ and $\varphi_1 = \varphi_3$, because the factorized term corresponds to a global operation on the field modes and has no physical consequence when only the atomic subsystem is measured (see Fig. C2.1). Then the simplified unitary system operator is given by

$$\hat{U}_S = \hat{\pi}_g \otimes \mathbf{1} \otimes \mathbf{1} + \hat{\pi}_e \otimes e^{-i\Delta \hat{L}_3}\, \hat{U}_M\, e^{i\Delta \hat{L}_3}. \tag{C2.5}$$

Finally, the action of $\hat{U}_S$ on two incoming field modes prepared in arbitrary states $|\psi\rangle$ and $|\varphi\rangle$ and on the atomic state is given by

$$\begin{aligned} \hat{U}_S \,|g\rangle\, |\psi\rangle\, |\varphi\rangle &= |g\rangle\, |\psi\rangle\, |\varphi\rangle \\ \hat{U}_S \,|e\rangle\, |\psi\rangle\, |\varphi\rangle &= |e\rangle e^{-i(\phi + \Delta)\hat{n}_0} \hat{\Pi}_0 \,|\varphi\rangle \otimes e^{-i(\phi - \Delta)\hat{n}_1} \hat{\Pi}_1 \,|\psi\rangle\,. \end{aligned} \tag{C2.6}$$

Then, by appropriately tuning the phases ϕ and Δ one can choose the mode in which a parity operator is applied.

The platform consists of initializing the control atom in $|+\rangle_a = (|g\rangle_a + |e\rangle_a)/\sqrt{2}$, an input state ρ displaced by α, obtaining $\rho' = \hat{D}(\alpha)\rho\hat{D}^\dagger(\alpha)$, and a pure state $|\varphi\rangle$ as the probe. As shown in Fig. C2.1, the initial state of the system can be written

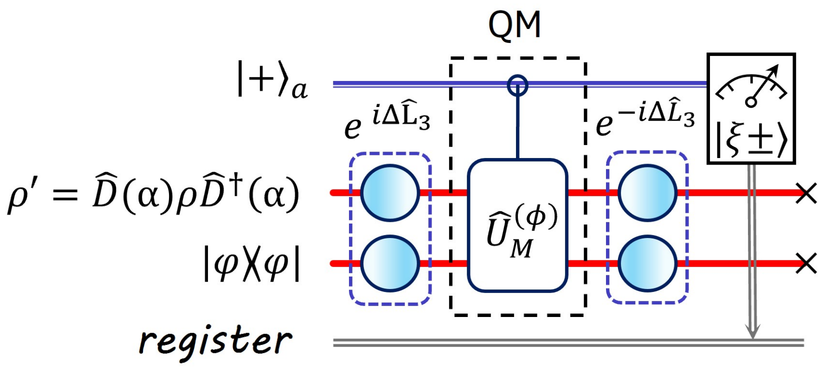

Figure C2.1: Quantum circuit implementing the unitary operator defined in Eq. (C2.5) The phase symmetrical response of the quantum mirror (QM) is modified by introducing relative path-dependent phases Δ before and after the QM, enabling the existence of a photon-parity operator acting on only one of the two modes. The mode in which this parity operator is applied depends on the choice of Δ and ϕ. The operator $\hat{U}_M^{(\phi)}$ becomes $\hat{U}_S$ once the phase $\phi = \pi/2$ is set, as shown in Fig. 5.2.1.

as

$$\rho_{sys}^{(i)} = |+\rangle\langle+| \otimes \rho' \otimes |\varphi\rangle\langle\varphi| = \left(\frac{\hat{\pi}_g + \hat{\pi}_{ge} + \hat{\pi}_{eg} + \hat{\pi}_e}{2}\right) \otimes \left(\sum_i p_i' \, |\psi_i'\rangle\langle\psi_i'|\right) \otimes |\varphi\rangle\langle\varphi| \,. \tag{C2.7}$$

The action of the operator $\hat{U}_S$, defined in Eq. (C2.7), on the initial state is given by

$$\begin{aligned}\hat{U}_S\,\rho_{sys}^{(i)}\,\hat{U}_S^\dagger = \frac{1}{4}\Bigg(&\pi_{gg} \otimes \rho' \otimes |\varphi\rangle\langle\varphi| \\ &+ \pi_{ge} \otimes \sum_i p_i' \, |\psi_i'\rangle\langle\varphi|\,\hat{U}_{\pi+\Delta-\phi}^\dagger \otimes |\varphi\rangle\langle\psi_i'|\,\hat{U}_{\pi-\Delta-\phi}^\dagger \\ &+ \pi_{eg} \otimes \sum_i p_i' \, \hat{U}_{\pi-\Delta-\phi}\,|\varphi\rangle\langle\psi_i'| \otimes \hat{U}_{\pi+\Delta-\phi}\,|\psi_i'\rangle\langle\varphi| \\ &+ \pi_{ee} \otimes \hat{U}_{\pi-\Delta-\phi}\,|\varphi\rangle\langle\varphi|\,\hat{U}_{\pi-\Delta-\phi}^\dagger \otimes \hat{U}_{\pi+\Delta-\phi}\rho'\hat{U}_{\pi+\Delta-\phi}^\dagger\Bigg),\end{aligned} \tag{C2.8}$$

where $\hat{U}_\alpha = e^{i\alpha\hat{n}}$ implements a phase shift α in the corresponding mode. We then apply a partial trace over the photonic modes

$$
\begin{aligned}
\rho_{at}^{(f)} &= \mathrm{Tr}_{0,1}\{\hat{U}_S \rho_{sys} \hat{U}_S^\dagger\} \\
&= \frac{1}{4}\Big(\hat{\pi}_{gg} + \hat{\pi}_{eg} \sum_i p_i' \langle\psi_i'| \hat{\Pi}_0 e^{-i(\phi+\Delta)n_0} |\varphi\rangle \langle\varphi| \hat{\Pi}_1 e^{-i(\phi-\Delta)n_1} |\psi_i'\rangle \\
&\qquad + \hat{\pi}_{ge} \sum_i p_i' \langle\varphi| \hat{\Pi}_0^\dagger e^{i(\Delta+\phi)n_0} |\psi_i'\rangle \langle\psi_i'| \hat{\Pi}_1^\dagger e^{i(\phi-\Delta)n_1} |\varphi\rangle + \hat{\pi}_{ee}\Big) \\
&= \frac{1}{4}\Big(\hat{\pi}_{gg} + \hat{\pi}_{eg} \langle\varphi| \hat{\Pi}\, e^{-i(\phi-\Delta)\hat{n}} \hat{D}(\alpha)\rho\hat{D}^\dagger(\alpha)\hat{\Pi}\, e^{-i(\phi+\Delta)\hat{n}} |\varphi\rangle \\
&\qquad + \hat{\pi}_{ge} \langle\varphi| \hat{\Pi}^\dagger e^{i(\Delta+\phi)\hat{n}} \hat{D}(\alpha)\rho\hat{D}^\dagger(\alpha)\hat{\Pi}^\dagger e^{i(\phi-\Delta)\hat{n}} |\varphi\rangle + \hat{\pi}_{ee}\Big),
\end{aligned}
\tag{C2.9}
$$

which allows us to recognize the interference terms on the final state of the control atom. Measuring them on the superposition basis $|\xi_\pm\rangle_a = (|g\rangle_a \pm e^{i\delta}|e\rangle_a)/\sqrt{2}$, we can write the probabilities as

$$
\boxed{p_\pm(\delta) = \frac{1}{2}\left(1 \pm \mathrm{Re}\left[e^{i\delta} \langle\varphi| \hat{\Pi}^\dagger e^{i(\Delta+\phi)\hat{n}} \hat{D}(\alpha)\rho\hat{D}^\dagger(\alpha)\hat{\Pi}^\dagger e^{i(\phi-\Delta)\hat{n}} |\varphi\rangle\right]\right)}
\tag{C2.10}
$$

In the main manuscript, we have selected the parameters $\phi = \Delta = \pi/2$.

C3 Wavefunction reconstruction

The electromagnetic field can be described as a collection of decoupled harmonic oscillators, each characterized by canonical operators *position* $\hat{q}$ and *momentum* $\hat{p}$ satisfying the commutation relation $[\hat{q}, \hat{p}] = i\hbar$. For each mode of frequency ω, the corresponding bosonic annihilation operator is defined as

$$
\hat{a} = \sqrt{\frac{1}{2\hbar\omega}}(\omega\hat{q} + i\hat{p}).
\tag{C3.1}
$$

It is convenient to introduce the dimensionless quadrature operators $\hat{Q} = \hat{q}\sqrt{\omega/\hbar}$ and $\hat{P} = \hat{p}/\sqrt{\hbar\omega}$, which satisfy the normalized commutation relation $[\hat{Q}, \hat{P}] = i$. Since $\hat{Q}$ is proportional to $\hat{q}$, they both share the same eigenstates in the continuous spectra $|q\rangle$ such that $\hat{Q}|q\rangle = s|q\rangle$ with $s = q\sqrt{\omega/\hbar}$.

On the other hand, one may generate a rotated quadrature by applying the phase-space rotation operator $e^{i\vartheta\hat{n}}$, acting on the eigenvalue equation for $\hat{Q}$

$$\left(\frac{\hat{a}e^{-i\vartheta}+\hat{a}^{\dagger}e^{i\vartheta}}{\sqrt{2}}\right)|r_\vartheta\rangle = \underbrace{(\hat{Q}\cos\vartheta+\hat{P}\sin\vartheta)}_{\hat{R}_\vartheta}|r_\vartheta\rangle = s\,|r_\vartheta\rangle\,, \tag{C3.2}$$

where $|r_\vartheta\rangle = e^{i\vartheta\hat{n}}|q\rangle$ is the eigenstate of the rotated quadrature operator $\hat{R}_\vartheta$, which retains the same eigenvalue s. In the particular case of $\vartheta = \pi/2$, one finds $\left|r_{\pi/2}\right\rangle = e^{i\pi\hat{n}/2}|q\rangle = |p\rangle$ which is the eigenstate of the momentum-like quadrature operator $\hat{P}$.

We now derive the wavefunctions of Fock states in the q-representation. Starting from the eigenvalue equation $\hat{a}^\dagger\hat{a}\,|n\rangle = n\,|n\rangle$ and projecting onto the continuous basis $|q\rangle$, one obtains the differential equation

$$\frac{\partial^2\psi_q^{(n)}(s)}{\partial s^2} + (2n+1-s^2)\psi_q^{(n)}(s) = 0, \tag{C3.3}$$

where $\psi_q^{(n)}(s) = \langle q|n\rangle$. The normalized solutions in s variable are given by

$$\psi_q^{(n)}(s) = \frac{1}{(2^n n!)^{1/2}}\sqrt[4]{\frac{1}{\pi}}e^{-s^2/2}\mathrm{H}_n(s), \tag{C3.4}$$

where $H_n(s)$ denotes the Hermite polynomial of order n.

The wavefunction of a coherent state $|\alpha\rangle$ in the q-representation can be obtained from its expansion in the Fock basis and projecting onto $|q\rangle$. Then, using the generating function of Hermite polynomials, one finds

$$\begin{aligned}\psi_q^{(\alpha)}(s) = \langle q|\alpha\rangle = e^{-|\alpha|^2/2}\sum_{n=0}\frac{\alpha^n}{\sqrt{n!}}\psi_s^{(n)}(s) &= \sqrt[4]{\frac{1}{\pi}}e^{-|\alpha|^2/2}e^{-s^2/2}\sum_{n=0}\frac{(\alpha/\sqrt{2})^n}{n!}\mathrm{H}_n(s)\\ &= \sqrt[4]{\frac{1}{\pi}}e^{-|\alpha|^2/2}e^{-s^2/2}e^{-\alpha^2/2+\sqrt{2}\alpha s}\end{aligned} \tag{C3.5}$$

Since the q-representation and p-representation wavefunctions are related by a Fourier transform, we introduce the following definition [114]:

$$\tilde{f}(k) = \tfrac{1}{\sqrt{2\pi}}\int_{-\infty}^{\infty} f(s)\,\mathrm{e}^{-isk}ds := (\hat{F}f)(k) \tag{C3.6}$$

$$f(s) = \tfrac{1}{\sqrt{2\pi}}\int_{-\infty}^{\infty} \tilde{f}(k)\,\mathrm{e}^{isk}dk := (\hat{F}^{-1}f)(s) \tag{C3.7}$$

where an operator form $\hat{F}$ of this transform is introduced. Applying this operator to the wavefunction of a Fock state in the q-representation yields

$$\underbrace{\psi_p^{(n)}(s)}_{\langle p|n\rangle} = \underbrace{\hat{F}\psi_q^{(n)}(s)}_{\langle q|e^{-i\frac{\pi}{2}\hat{n}}|n\rangle} = e^{-i\pi n/2}\psi_q^{(n)}(s) = (-i)^n\psi_q^{(n)}(s), \tag{C3.8}$$

where the Fourier transform operator can be expressed in terms of the photon number operator as $\hat{F} = e^{-i\frac{\pi}{2}\hat{n}}$.

Because the q-representation wavefunctions belong to the square-integrable space $L^2(\mathbb{R})$, the Fourier transform is a closed operation and maps this space onto itself.

As an example, we determine the wavefunction of a coherent state $|\alpha\rangle$ in the p-representation. Although this result can be obtained in several ways, the most straightforward approach employs the operator representation of the Fourier transform

$$\psi_p^{(\alpha)}(s) = \langle p|\alpha\rangle = \langle q|\, e^{-i\frac{\pi}{2}\hat{n}}\,|\alpha\rangle = \langle q|{-i\alpha}\rangle = \sqrt[4]{\frac{1}{\pi}}e^{-|\alpha|^2/2}e^{-s^2/2}e^{\alpha^2/2-i\alpha s\sqrt{2}}. \tag{C3.9}$$

This result can be independently verified by directly applying the Fourier transform defined in Eq. (C3.6) to the explicit q-representation wavefunction given in Eq. (C3.5).

The above reasoning can be extended beyond the q and p representations to a continuous family of intermediate quadrature representations obtained by an arbitrary phase-space rotation generated by the number operator. Defining the rotated quadrature eigenstates as $|r_\vartheta\rangle = e^{i\vartheta\hat{n}}\,|q\rangle$, the corresponding wavefunction of the coherent state reads as

$$\begin{aligned}\psi_r^{(\alpha)}(s) = \langle r_\vartheta|\alpha\rangle = \langle q|\, e^{-i\vartheta\hat{n}}\,|\alpha\rangle = \left\langle q\middle|\alpha e^{-i\vartheta}\right\rangle = \sqrt[4]{\frac{1}{\pi}}e^{-|\alpha|^2/2}e^{-s^2/2}e^{-\alpha^2e^{-2i\vartheta}/2+\alpha s e^{-i\vartheta}\sqrt{2}} \\ = F_{-\vartheta}[\psi_q^{(\alpha)}(s)],\end{aligned} \tag{C3.10}$$

where the rotation operation corresponds to a fractional Fourier transform (FrFT) that maps the q-representation to an arbitrary quadrature representation. The

FrFT is defined as [115]

$$[F_\xi f](k) = \frac{e^{i(\pi-2\xi)/4}}{\sqrt{2\pi\sin\xi}} e^{-ik^2\cot(\xi)/2} \int_{-\infty}^{\infty} e^{-is^2\cot(\xi)/2+isk/\sin\xi} f(s)ds. \tag{C3.11}$$

For $\xi = -\pi/2$, this expression reduces to the Fourier transform defined in Eq. (C3.6).

C3.1 Cross-correlation procedure

Using an appropriate choice of variables, the displacement operator can be rewritten as a function of quadrature operators

$$\hat{D}\left(\frac{ite^{i\vartheta}}{\sqrt{2}}\right) = e^{it(\hat{Q}\cos\vartheta+\hat{P}\sin\vartheta)} = e^{it\hat{R}_\vartheta}. \tag{C3.12}$$

Using this representation, the wavefunction of the unknown state $|\psi\rangle$ can be reconstructed through a cross-correlation with a reference coherent state $|\alpha\rangle$. Upon applying an appropriate completeness operation, the inverse Fourier transform of the product wavefunctions naturally arises. Subsequently, the bare product of the wavefunctions is recovered by applying the Fourier transform. The details of this procedure are described below for two cases.

Wavefunction product in q-representation ($\vartheta = 0$)

$$\langle\alpha|\,\hat{D}\left(it/\sqrt{2}\right)|\psi\rangle = \int \langle\alpha|\,e^{it\hat{Q}}\,|q\rangle\,\langle q|\psi\rangle\,ds = \int \langle\alpha|q\rangle\,e^{its}\,\langle q|\psi\rangle\,ds = \int \psi_q^{(\alpha)*}(s)e^{its}\psi_q(s) \tag{C3.13}$$

$$\begin{aligned} F\left[\langle\alpha|\,\hat{D}\left(it/\sqrt{2}\right)|\psi\rangle\right](\omega) &= \frac{1}{\sqrt{2\pi}}\iint \psi_q^{(\alpha)*}(s)\psi_q(s)e^{its}e^{-i\omega t}dsdt \\ &= \frac{1}{\sqrt{2\pi}}\int \psi_q^{(\alpha)*}(s)\psi_q(s)\underbrace{\int e^{it(s-\omega)}dt}_{2\pi\delta(s-\omega)}ds \end{aligned} \tag{C3.14}$$

$$F\left[\langle\alpha|\,\hat{D}\left(it/\sqrt{2}\right)|\psi\rangle\right](\omega) = \sqrt{2\pi}\psi_q^{(\alpha)*}(\omega)\psi_q(\omega) \tag{C3.15}$$

Wavefunction product in p-representation ($\vartheta = \pi/2$)

$$\langle\alpha|\,\hat{D}\left(-t/\sqrt{2}\right)|\psi\rangle = \int \langle\alpha|\, e^{it\hat{P}}\,|p\rangle\,\langle p|\psi\rangle\, ds = \int \langle\alpha|p\rangle\, e^{its}\,\langle p|\psi\rangle\, ds = \int \psi_p^{(\alpha)*}(s)e^{its}\psi_p(s) \tag{C3.16}$$

$$F\left[\langle\alpha|\,\hat{D}\left(-t/\sqrt{2}\right)|\psi\rangle\right](\omega) = \sqrt{2\pi}\psi_p^{(\alpha)*}(\omega)\psi_p(\omega) \tag{C3.17}$$

Wavefunction product in r-representation: In this particular case, we choose the phase $\vartheta = \delta - \pi/2$ such that the phase of the displacement operator coincides with the phase δ of the reference coherent state $|\alpha\rangle$, which provides an experimentally convenient implementation due to the shared phase.

$$\langle\alpha|\,\hat{D}\left(te^{i\delta}/\sqrt{2}\right)|\psi\rangle = \int \langle\alpha|\, e^{it\hat{R}_\vartheta}\,|r_\vartheta\rangle\,\langle r_\vartheta|\psi\rangle\, ds = \int \psi_r^{(\alpha)*}(s)e^{its}\psi_r(s) \tag{C3.18}$$

$$F\left[\langle\alpha|\,\hat{D}\left(te^{i\delta}/\sqrt{2}\right)|\psi\rangle\right](\omega) = \sqrt{2\pi}\psi_r^{(\alpha)*}(\omega)\psi_r(\omega) \tag{C3.19}$$

An alternative choice is $\vartheta = \delta$, for which the coherent state wavefunction is real in that representation; however, this option requires delicate experimental control of the phase in the orthogonal quadrature for displacement.

C3.2 Quantum mirror implementation

As shown in the main paper, the quantity measurable by quantum mirrors is $\langle\varphi|\, e^{i\pi\hat{n}}\hat{D}(\alpha)\rho\hat{D}(\alpha)\,|\varphi\rangle$. In order to reconstruct the wavefunction, it is necessary to measure the cross-correlation between a coherent state $|\gamma\rangle$ and the unknown pure state $|\psi\rangle$, namely

$$\langle\gamma|\,\hat{D}(\beta)\,|\psi\rangle\,, \tag{C3.20}$$

where β contains the variable dependencies, as discussed in the previous subsection. Therefore, the measurement procedure was performed in two stages.

We choose the probe state as the coherent state $|\beta/2\rangle$ and displace the unknown state by $\beta/2-\gamma$. The measurable quantity then becomes

$$\begin{aligned} Z_\beta &= \langle \beta/2| \, e^{i\pi\hat{n}}\hat{D}(\beta/2-\gamma)\,|\psi\rangle \, \langle\psi| \, \hat{D}^\dagger(\beta/2-\gamma)\,|\beta/2\rangle \\ &= \langle -\beta/2| \, \hat{D}(\beta/2-\gamma)\,|\psi\rangle \, \langle\psi|\gamma\rangle \\ &= \langle 0| \, \hat{D}(-\gamma)\hat{D}(\beta)\,|\psi\rangle \, \langle\psi|\gamma\rangle \\ &= \langle \gamma| \, \hat{D}(\beta)\,|\psi\rangle \, \langle\psi|\gamma\rangle \, . \end{aligned} \tag{C3.21}$$

In particular, $Z_0 = |\langle\psi|\gamma\rangle|^2$, which implies $\langle\psi|\gamma\rangle = \sqrt{Z_0}\, e^{i\phi_0}$. Therefore, the desired overlap can be extracted as

$$\langle\gamma| \, \hat{D}(\beta)\,|\psi\rangle = \frac{Z_\beta}{\sqrt{Z_0}} e^{-i\phi_0}. \tag{C3.22}$$

Finally, the wavefunction in the r-representation can be reconstructed according to

$$\sqrt{2\pi}\, \psi_r^{(\gamma)*}(\omega)\psi_r(\omega) = F\Big[\langle\gamma| \, \hat{D}(\beta)\,|\psi\rangle\Big] = \frac{e^{-i\phi_0}}{\sqrt{Z_0}} F[Z_\beta], \tag{C3.23}$$

where F denotes the Fourier transform. If a different quadrature representation is required, the corresponding fractional Fourier transform (FrFT) can be applied to the signal.

C4 Direct measurement of the Wigner function

The Wigner function of the state ρ can be measured by applying two QMs, as shown in Fig. C4.1. The corresponding unitary operator of this system is given by

$$\hat{U}_{QM} \cdot \hat{U}_{QM} = \hat{\pi}_g \otimes \mathbf{1} \otimes \mathbf{1} + \hat{\pi}_e \otimes \hat{U}_M^2. \tag{C4.1}$$

We now evaluate the action of this operator on two incoming field modes prepared in arbitrary states $|\psi\rangle$ and $|\varphi\rangle$, assuming that the atom is initially in the excited state $|e\rangle$:

$$\begin{aligned} \hat{U}_{QM} \cdot \hat{U}_{QM}\,|e\rangle\,|\psi\rangle\,|\varphi\rangle &= \hat{U}_{QM} \cdot \Big(|e\rangle \otimes e^{-i\phi\hat{n}_0}\hat{\Pi}_0\,|\varphi\rangle \otimes e^{-i\phi\hat{n}_1}\hat{\Pi}_1\,|\psi\rangle\Big) \\ &= |e\rangle \otimes e^{-2i\phi\hat{n}_0}\,|\psi\rangle \otimes e^{-2i\phi\hat{n}_1}\,|\varphi\rangle \, . \end{aligned} \tag{C4.2}$$

Thus, the action of the total operator reduces to the addition of a phase 2ϕ to

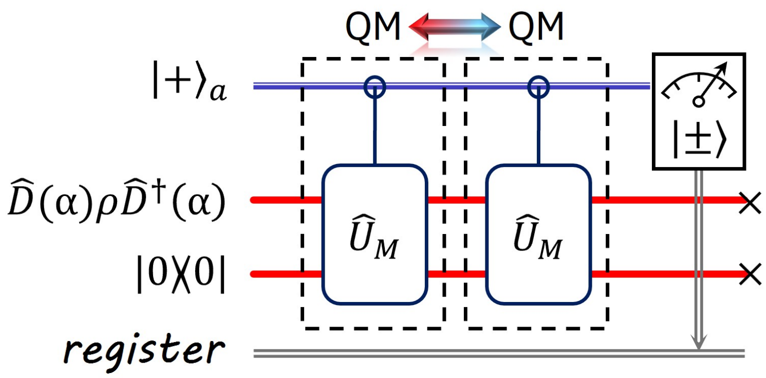

Figure C4.1: Direct measurement of the Wigner function of an unknown state ρ at phase space point α, represented as a quantum circuit. The setup incorporates a second QM, which may equivalently be realized by re-injecting the modes into the same QM.

each photonic mode when the atom is in the excited state.

Without making any assumption about the value of ϕ, the final density matrix of the system can be written as

$$\begin{aligned}\rho_{sys}^{(f)} &= \hat{U}_{QM}^{2}\,\rho_{sys}^{(i)}\,\hat{U}_{QM}^{\dagger 2}\\ &= \pi_{gg}\otimes\rho'\otimes|\varphi\rangle\langle\varphi| + \pi_{ge}\otimes\rho' e^{2i\phi\hat{n}_0}\otimes|\varphi\rangle\langle\varphi|\,e^{2i\phi\hat{n}_1}\\ &+ \pi_{eg}\otimes e^{-2i\phi\hat{n}_0}\rho'\otimes e^{-2i\phi\hat{n}_1}\,|\varphi\rangle\langle\varphi| + \pi_{ee}\otimes e^{-2i\phi\hat{n}_0}\rho' e^{2i\phi\hat{n}_0}\otimes e^{-2i\phi\hat{n}_1}\,|\varphi\rangle\langle\varphi|\,e^{2i\phi\hat{n}_1}\end{aligned} \tag{C4.3}$$

To obtain the probabilities, we measure the control atom. The diagonal contributions in the atomic basis yield unity due to the normalization of the states, whereas nontrivial contributions arise from the off-diagonal atomic terms. Imposing the vacuum condition for the second mode, $|\varphi\rangle = |0\rangle$, the probabilities reduce to

$$p_{\pm} = \frac{1}{2}\left(1 \pm \mathrm{Tr}[\rho' e^{-2i\phi\hat{n}}] \pm \mathrm{Tr}[e^{2i\phi\hat{n}}\rho']\right). \tag{C4.4}$$

For the specific choice $\phi = \pi/2$, the photon-number parity operator $\hat{\Pi} = e^{i\pi\hat{n}}$ naturally emerges. So, the probabilities take the simple form

$$p_{\pm} = \frac{1}{2}\Big(1 \pm \mathrm{Tr}[\hat{\Pi}\,\rho']\Big). \tag{C4.5}$$

Finally, writing the state as $\rho' = \hat{D}(\alpha)\rho\hat{D}^{\dagger}(\alpha)$ and using the definition of the

Wigner function introduced in Ref. [132], we obtain

$$W(\alpha) = \frac{2}{\pi}\big(p_+ - p_-\big) = \frac{2}{\pi}\langle\hat{\sigma}_x\rangle\,. \tag{C4.6}$$

This establishes a direct connection between the atomic measurement probabilities and the Wigner function of the field.

C5 Relative phase

In Eq. (C1.4), we establish the relation between the transmission and reflection coefficients for the beam splitter. Consequently, the two subspaces introduced in Eq. (C2.1), corresponding to the ground (g) and excited (e) states, can be described by this type of beam splitter. In each subspace, the coefficients satisfy the relation

$$t_k = r_k + e^{i\phi_k}, \tag{C5.1}$$

with $k = e, g$. From this expression, explicit forms of the coefficients in each subspace can be obtained. In particular, since $|r_g| \to 0$ when the atom is in the ground state and $|t_e| \to 0$ when the atom is in the excited state, we obtain

$$t_g = e^{i\phi_g} \quad (\text{for } |g\rangle), \tag{C5.2}$$

$$r_e = -e^{i\phi_e} \quad (\text{for } |e\rangle). \tag{C5.3}$$

The action of these coefficients in each subspace leads to the following transformations of the field operators:

$$(\hat{a}_0, \hat{a}_1) \xrightarrow{\hat{U}_g} (\hat{a}_0 e^{i\phi_g}, \hat{a}_1 e^{i\phi_g}), \tag{C5.4}$$

$$(\hat{a}_0, \hat{a}_1) \xrightarrow{\hat{U}_e} (-\hat{a}_1 e^{i\phi_e}, -\hat{a}_0 e^{i\phi_e}), \tag{C5.5}$$

this allows us to write a more general version of the QM operator, which can be written as

$$\hat{U}'_{QM} = \hat{\pi}_g \otimes \hat{U}_g + \hat{\pi}_e \otimes \hat{U}_e. \tag{C5.6}$$

Finally, the action of $\hat{U}'_{QM}$ on two incoming field modes prepared in arbitrary states $|\psi\rangle$ and $|\varphi\rangle$ and on the atomic state is given by

$$\begin{aligned}\hat{U}'_{QM}\,|g\rangle\,|\psi\rangle\,|\varphi\rangle &= |g\rangle\,\hat{U}_M^{(g)}\,|\psi\rangle\,|\varphi\rangle = |g\rangle\,e^{-i\phi_g\hat{n}_0}\,|\psi\rangle\,e^{-i\phi_g\hat{n}_1}\,|\varphi\rangle \\ &= (\mathbf{1}\otimes e^{-i\phi_g\hat{n}})\,|g\rangle\,|\psi\rangle\,|\varphi\rangle\end{aligned} \tag{C5.7}$$

$$\begin{aligned}\hat{U}'_{QM}\,|e\rangle\,|\psi\rangle\,|\varphi\rangle &= |e\rangle\,\hat{U}_M^{(e)}\,|\psi\rangle\,|\varphi\rangle = |e\rangle\,e^{-i\phi_e\hat{n}_0}\hat{\Pi}\,|\varphi\rangle\,e^{-i\phi_e\hat{n}_1}\hat{\Pi}\,|\psi\rangle \\ &= (\mathbf{1}\otimes e^{-i\phi_g\hat{n}})\,|e\rangle\,e^{-i(\phi_e-\phi_g)\hat{n}_0}\hat{\Pi}\,|\varphi\rangle\,e^{-i(\phi_e-\phi_g)\hat{n}_1}\hat{\Pi}\,|\psi\rangle\end{aligned} \tag{C5.8}$$

From these two expressions, we observe that the phase ϕ_g appears only as a global phase factor and is therefore physically irrelevant. Consequently, the physically relevant phase shift appearing in Eq. (C1.13) can be identified as the phase difference between the two internal states of the QM,

$$\phi = \phi_e - \phi_g. \tag{C5.9}$$

Appendix D: Additional Research

D1 Publications

This appendix presents additional publications produced during or shortly before my PhD studies that are not directly related to the main results of this thesis.

Shortly before beginning my doctoral studies, I had the pleasure to meet Dr. Carla Hermann-Avigliano and my current advisor, Dr. Pablo Solano. Our collaboration began with the study of the Dicke model and led to a protocol for the deterministic generation of large-photon-number states from an initial coherent state. The protocol does not require postselection and can reach photon numbers of $n \sim 100$ with optimal fidelities above 70% [37].

PHYSICAL REVIEW LETTERS **125,** 093603 (2020)

Deterministic Generation of Large Fock States

M. Uria,[1] P. Solano,[2,3] and C. Hermann-Avigliano[1,*]

[1]*Departamento de Física and Millennium Institute for Research in Optics (MIRO), Facultad de Ciencias Físicas y Matemáticas, Universidad de Chile, Santiago 8370448, Chile*

[2]*Department of Physics, MIT-Harvard Center for Ultracold Atoms, and Research Laboratory of Electronics, Massachusetts Institute of Technology, Cambridge, Massachusetts 02139, USA*

[3]*Departamento de Física, Facultad de Ciencias Fsicas y Matemticas, Universidad de Concepción, Concepción 160-C, Chile*

(Received 10 March 2020; accepted 4 August 2020; published 28 August 2020)

We present a protocol to deterministically prepare the electromagnetic field in a large photon number state. The field starts in a coherent state and, through resonant interaction with one or few two-level systems, it evolves into a coherently displaced Fock state without any postselection. We show the feasibility of the scheme under realistic parameters. The presented method opens a door to reach Fock states, with $n \sim 100$ and optimal fidelities above 70%, blurring the line between macroscopic and quantum states of the field.

DOI: 10.1103/PhysRevLett.125.093603

Similarly, at the beginning of my doctoral studies, I participated in the doctoral research of my former colleague, now Dr. David Ruelas, at the PUCP. Our work focused on the study of weak values beyond the regime of weak measurements. We extended a previous proposal to optical and quantum-computing platforms, demonstrating that weak values can be determined across a range of measurement strengths and that, for the model considered, strong measurements do not always outperform weak ones [135].

AVS Quantum Science
co-published with AIP Publishing

HOME BROWSE COLLECTIONS PUBLISH WITH US ABOUT

Volume 6, Issue 1
March 2024

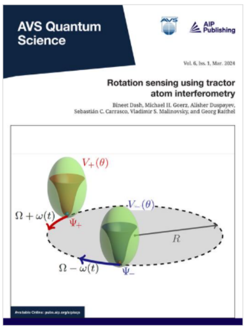

Previous Article Next Article

Article Contents

REFERENCES

RESEARCH ARTICLE | JANUARY 19 2024

Testing precision and accuracy of weak value measurements in an IBM quantum system

David R. A. Ruelas Paredes ; Mariano Uria ; Eduardo Massoni ; Francisco De Zela

Check for updates

+ Author & Article Information
AVS Quantum Sci. 6, 015001 (2024)
https://doi.org/10.1116/5.0184965 **Article history**

Share Tools

Historically, weak values have been associated with weak measurements performed on quantum systems. Over the past two decades, a series of works have shown that weak values can be determined via measurements of arbitrary strength. One such proposal by Denkmayr *et al.* [Phys. Rev. Lett. **118**, 010402 (2017)], carried out in neutron interferometry experiments, yielded better outcomes for strong than for weak measurements. We extend this scheme and explain how to implement it in an optical setting as well as in a quantum computational context. Our implementation in a quantum computing system provided by IBM confirms that weak values can be measured, with varying degrees of performance, over a range of measurement strengths. However, at least for this model, strong measurements do not always perform better than weak ones.

During my PhD, I also collaborated with Master's students Ignacio Salinas and Gerd Hartmann, as well as with the laboratory's recent acquisition, the postdoctoral researcher Dr. Victor Gondret. Our work focused on developing an experimentally accessible witness of nonclassicality for generalized coherent states. We showed that the intensity–field correlation function alone can reveal nonclassical behavior, providing a simple and low-complexity approach to detecting quantum signatures in non-Gaussian states [136].

PHYSICAL REVIEW RESEARCH **8**, 023118 (2026)

Characterization of generalized coherent states through intensity-field correlations

Ignacio Salinas Valdivieso,[1,*] Victor Gondret,[2,*] Gerd Hartmann S.,[2] Mariano Uria,[3]
Pablo Solano,[3] and Carla Hermann-Avigliano[1,2,†,‡]
[1]*Millennium Institute for Research in Optics—MIRO, Santiago, Chile*
[2]*Departamento de Física, Facultad de Ciencias Físicas y Matemáticas, Universidad de Chile, Santiago, Chile*
[3]*Departamento de Física, Facultad de Ciencias Físicas y Matemáticas, Universidad de Concepción, Concepción, Chile*

(Received 17 December 2025; accepted 25 March 2026; published 4 May 2026)

Non-Gaussian quantum states of light are essential resources for quantum information processing and precision metrology. Among them, generalized coherent states (GCSs), which naturally arise from the evolution of a coherent state with a nonlinear medium, exhibit useful quantum features such as Wigner negativity and metrological advantages [Phys. Rev. Res. 5, 013165 (2023)]. Because these states remain coherent to all orders, their nonclassical character cannot be revealed through standard intensity-intensity correlation measurements. Here, we demonstrate that the intensity-field correlation function alone provides a simple and experimentally accessible witness of nonclassicality. For GCSs, any deviation of this normalized correlation from unity signals nonclassical behavior. We derive analytical results for Kerr-generated states and extend the analysis to statistical mixtures of GCSs. The proposed approach enables real-time, low-complexity detection of quantum signatures in non-Gaussian states, offering a practical tool for experiments across a broad range of nonlinear regimes.

DOI: 10.1103/lykp-833h

We also explored an application of quantum mirrors in collaboration with Dr. Aldo Delgado. In this work, we proposed the use of quantum mirrors as nodes in quantum networks, where propagating coherent states mediate interactions between distant control qubits. This architecture enables quantum teleportation, quantum state transfer, and entanglement swapping, with both the success probability and average fidelity approaching unity as the mean photon number increases. We further showed that the teleportation protocol is robust against several realistic sources of error, providing a promising platform for long-distance quantum communication [103].

Alice and Bob through a quantum mirror

M. Uria,[1,*] C. Hermann-Avigliano,[2,3] P. Solano,[1] and A. Delgado[2,1,†]
[1]*Facultad de Ciencias Físicas y Matemáticas, Departamento de Física, Universidad de Concepción, Concepción, Chile*
[2]*ANID - Millenium Science Iniciative Program - Millenium Institute for Research in Optics*
[3]*Departamento de Física, Facultad de Ciencias Físicas y Matemáticas, Universidad de Chile, Santiago, Chile*

A quantum mirror is a device whose optical response, that is, transmission and reflection, can be controlled by a single qubit. Here, we propose the use of quantum mirrors as nodes in quantum networks. Propagating coherent states mediate the interaction between the control qubits of each quantum mirror. This allows implementing quantum teleportation, quantum state transfer, and entanglement swapping with success probability and average fidelity exponentially approaching unity as the average photon number increases. Furthermore, we show that quantum teleportation exhibits robustness against known sources of error, such as optical path phase difference, photon loss, and reduced quantum mirror reflectivity, presenting a promising alternative towards long-distance quantum communication.

Keywords: Quantum networks, quantum communication, metamaterial, quantum teleportation, quantum state transfer, entanglement swapping

Bibliography

[1] Anne E. B. Nielsen and Klaus Mølmer. Photon number states generated from a continuous-wave light source. *Phys. Rev. A*, 75:043801, Apr 2007.

[2] Hui Wang, Timothy C. Ralph, Jelmer J. Renema, Chao-Yang Lu, and Jian-Wei Pan. Scalable photonic quantum technologies. *Nature Materials*, 24(12):1883–1897, August 2025.

[3] Koen Alexander, Avishai Benyamini, Dylan Black, Damien Bonneau, Stanley Burgos, Ben Burridge, Hugo Cable, Geoff Campbell, Gabriel Catalano, Alejandro Ceballos, et al. A manufacturable platform for photonic quantum computing. *Nature*, 641(8064):876–883, 2025.

[4] Lars S. Madsen, Fabian Laudenbach, Mohsen Falamarzi. Askarani, Fabien Rortais, Trevor Vincent, Jacob F. F. Bulmer, Filippo M. Miatto, Leonhard Neuhaus, Lukas G. Helt, et al. Quantum computational advantage with a programmable photonic processor. *Nature*, 606(7912):75–81, 2022.

[5] Han-Sen Zhong, Hui Wang, Yu-Hao Deng, Ming-Cheng Chen, Li-Chao Peng, Yi-Han Luo, Jian Qin, Dian Wu, Xing Ding, Yi Hu, Peng Hu, et al. Quantum computational advantage using photons. *Science*, 370(6523):1460–1463, 2020.

[6] Francesco Anna Mele, Ludovico Lami, and Vittorio Giovannetti. Maximum tolerable excess noise in continuous-variable quantum key distribution and improved lower bound on two-way capacities. *Nature Photonics*, 19(3):329–334, 2025.

[7] J. Aasi, J. Abadie, B. P. Abbott, R. Abbott, T. D. Abbott, M. R. Abernathy, C. Adams, T. Adams, P. Addesso, et al. Enhanced sensitivity of the ligo gravitational wave detector by using squeezed states of light. *Nature Photonics*, 7(8):613–619, 2013.

[8] Samuel L. Braunstein and Peter van Loock. Quantum information with continuous variables. *Rev. Mod. Phys.*, 77:513–577, Jun 2005.

[9] U.L. Andersen, G. Leuchs, and C. Silberhorn. Continuous-variable quantum information processing. *Laser & Photonics Reviews*, 4(3):337–354, April 2010.

[10] Ulrik L. Andersen, Jonas S. Neergaard-Nielsen, Peter van Loock, and Akira

Furusawa. Hybrid discrete-and continuous-variable quantum-information. *Nature Physics*, 11(9):713–719, September 2015.

[11] Daniel Gottesman, Alexei Kitaev, and John Preskill. Encoding a qubit in an oscillator. *Physical Review A*, 64(1), June 2001.

[12] Jérémie Guillaud and Mazyar Mirrahimi. Repetition cat qubits for fault-tolerant quantum computation. *Physical Review X*, 9(4), December 2019.

[13] Carlton M. Caves. Quantum-mechanical noise in an interferometer. *Physical Review D*, 23(8):1693–1708, April 1981.

[14] B. M. Escher, R. L. de Matos Filho, and L. Davidovich. Quantum metrology for noisy systems. *Brazilian Journal of Physics*, 41(4–6):229–247, September 2011.

[15] Emanuele Polino, Mauro Valeri, Nicolò Spagnolo, and Fabio Sciarrino. Photonic quantum metrology. *AVS Quantum Science*, 2(2), June 2020.

[16] Vittorio Giovannetti, Seth Lloyd, and Lorenzo Maccone. Quantum metrology. *Physical Review Letters*, 96(1), January 2006.

[17] R. J. Glauber. The quantum theory of optical coherence. *Phys. Rev.*, 130:2529, Jun 1963.

[18] Kok Chuan Tan and Hyunseok Jeong. Nonclassical light and metrological power: An introductory review. *AVS Quantum Science*, 1(1), November 2019.

[19] Marlan O. Scully and Willis E. Lamb. Quantum theory of an optical maser. i. general theory. *Physical Review*, 159(2):208–226, July 1967.

[20] E. C. G. Sudarshan. Equivalence of semiclassical and quantum mechanical descriptions of statistical light beams. *Physical Review Letters*, 10(7):277–279, April 1963.

[21] L. Mandel. Sub-poissonian photon statistics in resonance fluorescence. *Opt. Lett.*, 4(7):205, Jul 1979.

[22] Mark Hillery. Nonclassical distance in quantum optics. *Physical Review A*, 35(2):725–732, January 1987.

[23] Michael A. Nielsen and Isaac L. Chuang. *Quantum Computation and Quantum Information: 10th Anniversary Edition*. Cambridge University Press, December 2010.

[24] János K. Asbóth, John Calsamiglia, and Helmut Ritsch. Computable measure of nonclassicality for light. *Phys. Rev. Lett.*, 94:173602, May 2005.

[25] M. S. Kim, W. Son, V. Bužek, and P. L. Knight. Entanglement by a beam splitter: Nonclassicality as a prerequisite for entanglement. *Phys. Rev. A*, 65:032323, Feb 2002.

[26] A. Kenfack and K. Życzkowski. Negativity of the wigner function as an indicator of non-classicality. *Journal of Optics B: Quantum and Semiclassical Optics*, 6(10):396, aug 2004.

[27] Samuel L. Braunstein and Peter van Loock. Quantum information with continuous variables. *Rev. Mod. Phys.*, 77:513–577, Jun 2005.

[28] D. Stoler, B.E.A. Saleh, and M.C. Teich. Binomial states of the quantized radiation field. *Optica Acta: International Journal of Optics*, 32(3):345–355, March 1985.

[29] Marios H. Michael, Matti Silveri, R. T. Brierley, Victor V. Albert, Juha Salmilehto, Liang Jiang, and S. M. Girvin. New class of quantum error-correcting codes for a bosonic mode. *Physical Review X*, 6(3), July 2016.

[30] Atharv Joshi, Kyungjoo Noh, and Yvonne Y Gao. Quantum information processing with bosonic qubits in circuit qed. *Quantum Science and Technology*, 6(3):033001, apr 2021.

[31] M. Uria, A. Maldonado-Trapp, C. Hermann-Avigliano, and P. Solano. Emergence of non-gaussian coherent states through nonlinear interactions. *Phys. Rev. Res.*, 5:013165, Mar 2023.

[32] Mariano Uria, Ricardo Gutiérrez-Jáuregui, Carla Hermann-Avigliano, and Pablo Solano. Post-selection free generation of multi-photon added coherent states, 2026.

[33] Mariano Uria, Amaru Moya, Carla Hermann-Avigliano, Pablo Solano, and Aldo Delgado. Continuous-variable quantum state tomography enabled by quantum mirrors, 2026.

[34] E.T. Jaynes and F.W. Cummings. Comparison of quantum and semiclassical radiation theories with application to the beam maser. *Proceedings of the IEEE*, 51(1):89–109, 1963.

[35] R. J. Glauber. Coherent and incoherent states of the radiation field. *Phys. Rev.*, 131:2766, Sep 1963.

[36] B. Hacker, S. Welte, S. Daiss, A. Shaukat, S. Ritter, L. Li, and G. Rempe. Deterministic creation of entangled atom-light schrödinger-cat states. *Nature Photonics*, 13(2):110, 2019.

[37] M. Uria, P. Solano, and C. Hermann-Avigliano. Deterministic generation of large fock states. *Phys. Rev. Lett.*, 125:093603, Aug 2020.

[38] F. Siyouri, M. El Baz, and Y. Hassouni. The negativity of wigner function as a measure of quantum correlations. *Quantum Information Processing*, 15(10):4237, 2016.

[39] S. L. Braunstein and C. M. Caves. Statistical distance and the geometry of quantum states. *Phys. Rev. Lett.*, 72:3439, May 1994.

[40] R. W. Boyd. *Nonlinear Optics.* Academic Press, 2003.

[41] J. Gea-Banacloche. Atom- and field-state evolution in the jaynes-cummings model for large initial fields. *Phys. Rev. A*, 44:5913, Nov 1991.

[42] S. M. Chumakov, A. B. Klimov, and J. J. Sanchez-Mondragon. General properties of quantum optical systems in a strong-field limit. *Phys. Rev. A*, 49:4972, Jun 1994.

[43] S. M. Chumakov, A. B. Klimov, and C. Saavedra. Competing interactions and quantum nonspreading wave packets. *Phys. Rev. A*, 52:3153, Oct 1995.

[44] C. Saavedra, A. B. Klimov, S. M. Chumakov, and J. C. Retamal. Dissipation in collective interactions. *Phys. Rev. A*, 58:4078, Nov 1998.

[45] S. Haroche and J. M. Raimond. *Exploring the Quantum: Atoms, Cavities, and Photons.* Oxford University Press, 2013.

[46] V. V. Dodonov and V. I. Man'ko. *Theory of Nonclassical States of Light.* CRC Press, 2003.

[47] U. M. Titulaer and R. J. Glauber. Density operators for coherent fields. *Phys. Rev.*, 145:1041, May 1966.

[48] Z. Bialynicka-Birula. Properties of the generalized coherent state. *Phys. Rev.*, 173:1207, Sep 1968.

[49] D. Stoler. Generalized coherent states. *Phys. Rev. D*, 4:2309–2312, Oct 1971.

[50] B. Yurke and D. Stoler. Generating quantum mechanical superpositions of macroscopically distinguishable states via amplitude dispersion. *Phys. Rev. Lett.*, 57:13, Jul 1986.

[51] G. S. Agarwal and K. Tara. Nonclassical character of states exhibiting no squeezing or sub-poissonian statistics. *Phys. Rev. A*, 46:485, Jul 1992.

[52] C. T. Lee. Higher-order criteria for nonclassical effects in photon statistics. *Phys. Rev. A*, 41:1721, Feb 1990.

[53] Y. Kim and T. H. Yoon. Higher order sub-poissonian photon statistics of light. *Optics Communications*, 212(1):107, 2002.

[54] U. M. Titulaer and R. J. Glauber. Correlation functions for coherent fields. *Phys. Rev.*, 140:B676, Nov 1965.

[55] K. E. Cahill and R. J. Glauber. Ordered expansions in boson amplitude operators. *Physical Review*, 177(5):1857–1881, January 1969.

[56] K. C. Tan and H. Jeong. Nonclassical light and metrological power: An introductory review. *AVS Quantum Science*, 1(1):014701, 2019.

[57] B. M. Escher, R. L. de Matos Filho, and L. Davidovich. Quantum metrology for noisy systems. *Braz. J. Phys.*, 41:229, 2011.

[58] M. Penasa, S. Gerlich, T. Rybarczyk, V. Métillon, M. Brune, J. M. Raimond, S. Haroche, L. Davidovich, and I. Dotsenko. Measurement of a microwave field amplitude beyond the standard quantum limit. *Phys. Rev. A*, 94:022313, Aug 2016.

[59] R. J. Lewis-Swan, D. Barberena, J. A. Muniz, J. R. K. Cline, D. Young, J. K. Thompson, and A. M. Rey. Protocol for precise field sensing in the optical domain with cold atoms in a cavity. *Phys. Rev. Lett.*, 124:193602, May 2020.

[60] H. Vahlbruch, M. Mehmet, K. Danzmann, and R. Schnabel. Detection of 15 db squeezed states of light and their application for the absolute calibration of photoelectric quantum efficiency. *Phys. Rev. Lett.*, 117:110801, Sep 2016.

[61] U. L. Andersen and T. Gehring and C. Marquardt and G. Leuchs. 30 years of squeezed light generation. *Physica Scripta*, 91:053001, 2016.

[62] R. F. Werner. Quantum states with einstein-podolsky-rosen correlations admitting a hidden-variable model. *Phys. Rev. A*, 40:4277, Oct 1989.

[63] M. M. Wilde. *Quantum Information Theory.* Cambridge University Press, 2 edition, 2017.

[64] B. Teklu, A. Ferraro, M. Paternostro, and M. G. A. Paris. Nonlinearity and nonclassicality in a nanomechanical resonator. *EPJ Quantum Technology*, 2:16, 2015.

[65] F. Albarelli, A. Ferraro, M. Paternostro, and M. G. A. Paris. Nonlinearity as a resource for nonclassicality in anharmonic systems. *Phys. Rev. A*, 93:032112, Mar 2016.

[66] G. S. Agarwal and K. Tara. Nonclassical properties of states generated by the excitations on a coherent state. *Phys. Rev. A*, 43:492–497, Jan 1991.

[67] Serge Haroche and Jean-Michel Raimond. *Exploring the Quantum: Atoms, Cavities, and Photons.* OUP Oxford, August 2006.

[68] K Laiho, M Avenhaus, K N Cassemiro, and Ch Silberhorn. Direct probing of the wigner function by time-multiplexed detection of photon statistics. *New Journal of Physics*, 11(4):043012, April 2009.

[69] Paulo Vinícius Pereira Pinheiro and Rubens Viana Ramos. Quantum communication with photon-added coherent states. *Quantum Information Processing*, 12(1):537–547, March 2012.

[70] Arpita Chatterjee, Kishore Thapliyal, and Anirban Pathak. Quantifying quantum correlation of quasi-werner state and probing its suitability for quantum teleportation. *Annalen der Physik*, 533(10), July 2021.

[71] Marina Kudra, Martin Jirlow, Mikael Kervinen, Axel M Eriksson, Fernando Quijandría, Per Delsing, Tahereh Abad, and Simone Gasparinetti. Experimental realization of deterministic and selective photon addition

in a bosonic mode assisted by an ancillary qubit. *Quantum Science and Technology*, 10(4):045037, September 2025.

[72] Alessandro Zavatta, Silvia Viciani, and Marco Bellini. Quantum-to-classical transition with single-photon-added coherent states of light. *Science*, 306(5696):660–662, 2004.

[73] Marco Barbieri, Nicolò Spagnolo, Marco G. Genoni, Franck Ferreyrol, Rémi Blandino, Matteo G. A. Paris, Philippe Grangier, and Rosa Tualle-Brouri. Non-gaussianity of quantum states: An experimental test on single-photon-added coherent states. *Phys. Rev. A*, 82:063833, Dec 2010.

[74] R. Kumar, E. Barrios, C. Kupchak, and A. I. Lvovsky. Experimental characterization of bosonic creation and annihilation operators. *Phys. Rev. Lett.*, 110:130403, Mar 2013.

[75] Jiří Fadrný, Michal Neset, Martin Bielak, Miroslav Ježek, Jan Bílek, and Jaromír Fiurášek. Experimental preparation of multiphoton-added coherent states of light. *npj Quantum Information*, 10(1), September 2024.

[76] Daisuke Iyama, Takahiko Kamiya, Shiori Fujii, Hiroto Mukai, Yu Zhou, Toshiaki Nagase, Akiyoshi Tomonaga, Rui Wang, Jiao-Jiao Xue, Shohei Watabe, Sangil Kwon, and Jaw-Shen Tsai. Observation and manipulation of quantum interference in a superconducting kerr parametric oscillator. *Nature Communications*, 15(1), January 2024.

[77] Girish S. Agarwal. *Quantum Optics*. Cambridge University Press, November 2012.

[78] S. Sivakumar. Truncated coherent states and photon-addition. *International Journal of Theoretical Physics*, 53(5), 2014.

[79] A. Imamoḡlu, H. Schmidt, G. Woods, and M. Deutsch. Strongly interacting photons in a nonlinear cavity. *Phys. Rev. Lett.*, 79:1467–1470, Aug 1997.

[80] A. J. Hoffman, S. J. Srinivasan, S. Schmidt, L. Spietz, J. Aumentado, H. E. Türeci, and A. A. Houck. Dispersive photon blockade in a superconducting circuit. *Phys. Rev. Lett.*, 107:053602, Jul 2011.

[81] P D Drummond and D F Walls. Quantum theory of optical bistability. i. nonlinear polarisability model. *Journal of Physics A: Mathematical and General*, 13(2):725, feb 1980.

[82] Adam Miranowicz, Małgorzata Paprzycka, Yu-xi Liu, Ji ří Bajer, and Franco Nori. Two-photon and three-photon blockades in driven nonlinear systems. *Phys. Rev. A*, 87:023809, Feb 2013.

[83] Evgeny V. Anikin, Natalya S. Maslova, Nikolay A. Gippius, and Igor M. Sokolov. Multiphoton resonance in a driven kerr oscillator in the presence of high-order nonlinearities. *Phys. Rev. A*, 104:053106, Nov 2021.

[84] Benjamin Yadin, Felix C. Binder, Jayne Thompson, Varun Narasimhachar, Mile Gu, and M. S. Kim. Operational resource theory of continuous-variable nonclassicality. *Physical Review X*, 8(4), December 2018.

[85] Mark Hillery. Total noise and nonclassical states. *Physical Review A*, 39(6):2994–3002, March 1989.

[86] J. M. Raimond, C. Sayrin, S. Gleyzes, I. Dotsenko, M. Brune, S. Haroche, P. Facchi, and S. Pascazio. Phase space tweezers for tailoring cavity fields by quantum zeno dynamics. *Physical Review Letters*, 105(21), November 2010.

[87] A. I. Lvovsky and M. G. Raymer. Continuous-variable optical quantum-state tomography. *Rev. Mod. Phys.*, 81:299–332, Mar 2009.

[88] Francesco A. Mele, Antonio A. Mele, Lennart Bittel, Jens Eisert, Vittorio Giovannetti, Ludovico Lami, Lorenzo Leone, and Salvatore F. E. Oliviero. Learning quantum states of continuous-variable systems. *Nature Physics*, 21(12):2002–2008, 2025.

[89] Ryan O'Donnell and John Wright. Efficient quantum tomography. In *Proceedings of the Forty-Eighth Annual ACM Symposium on Theory of Computing*, STOC '16, page 899–912, New York, NY, USA, 2016. Association for Computing Machinery.

[90] Jeongwan Haah, Aram W. Harrow, Zhengfeng Ji, Xiaodi Wu, and Nengkun Yu. Sample-optimal tomography of quantum states. *IEEE Transactions on Information Theory*, 63(9):5628–5641, 2017.

[91] U. Leonhardt. *Measuring the Quantum State of Light*. Cambridge Studies in Modern Optics. Cambridge University Press, 1997.

[92] K. Vogel and H. Risken. Determination of quasiprobability distributions in terms of probability distributions for the rotated quadrature phase. *Physical Review A*, 40(5):2847–2849, September 1989.

[93] Ingrid Strandberg. Simple, reliable, and noise-resilient continuous-variable quantum state tomography with convex optimization. *Physical Review Applied*, 18(4), October 2022.

[94] Shahnawaz Ahmed, Carlos Sánchez Muñoz, Franco Nori, and Anton Frisk Kockum. Classification and reconstruction of optical quantum states with deep neural networks. *Physical Review Research*, 3(3), September 2021.

[95] L. G. Lutterbach and L. Davidovich. Method for direct measurement of the wigner function in cavity qed and ion traps. *Physical Review Letters*, 78(13):2547–2550, March 1997.

[96] Chao Shen, Reinier W. Heeres, Philip Reinhold, Luyao Jiang, Yi-Kai Liu, Robert J. Schoelkopf, and Liang Jiang. Optimized tomography of

continuous variable systems using excitation counting. *Physical Review A*, 94(5), November 2016.

[97] C. J. Villas-Bôas, G. A. Prataviera, and M. H. Y. Moussa. Direct measurement of the wigner distribution of a traveling field. *Physical Review A*, 64(6), November 2001.

[98] E. Solano. Selective interactions in trapped ions: State reconstruction and quantum logic. *Physical Review A*, 71(1), January 2005.

[99] D. Leibfried, D. M. Meekhof, B. E. King, C. Monroe, W. M. Itano, and D. J. Wineland. Experimental determination of the motional quantum state of a trapped atom. *Physical Review Letters*, 77(21):4281–4285, November 1996.

[100] Jeff S. Lundeen, Brandon Sutherland, Aabid Patel, Corey Stewart, and Charles Bamber. Direct measurement of the quantum wavefunction. *Nature*, 474(7350):188–191, June 2011.

[101] R. Bekenstein, I. Pikovski, H. Pichler, E. Shahmoon, S. F. Yelin, and M. D. Lukin. Quantum metasurfaces with atom arrays. *Nature Physics*, 16(6):676–681, March 2020.

[102] Richard A. Campos, Bahaa E. A. Saleh, and Malvin C. Teich. Quantum-mechanical lossless beam splitter: Su(2) symmetry and photon statistics. *Physical Review A*, 40(3):1371–1384, August 1989.

[103] M. Uria, C. Hermann-Avigliano, P. Solano, and A. Delgado. Alice and bob through a quantum mirror, March 2026.

[104] Gerhard Kirchmair, Brian Vlastakis, Zaki Leghtas, Simon E. Nigg, Hanhee Paik, Eran Ginossar, Mazyar Mirrahimi, Luigi Frunzio, S. M. Girvin, and R. J. Schoelkopf. Observation of quantum state collapse and revival due to the single-photon kerr effect. *Nature*, 495(7440):205–209, 2013.

[105] U. Leonhardt and H. Paul. Phase measurement and q function. *Phys. Rev. A*, 47:R2460–R2463, Apr 1993.

[106] Harry Buhrman, Richard Cleve, John Watrous, and Ronald de Wolf. Quantum fingerprinting. *Physical Review Letters*, 87(16), September 2001.

[107] Juan Carlos Garcia-Escartin and Pedro Chamorro-Posada. swap test and hong-ou-mandel effect are equivalent. *Physical Review A*, 87(5), May 2013.

[108] T. J. Volkoff and Yiğit Subaşı. Ancilla-free continuous-variable SWAP test. *Quantum*, 6:800, September 2022.

[109] C. L. Mehta. Diagonal coherent-state representation of quantum operators. *Physical Review Letters*, 18(18):752–754, May 1967.

[110] A A Semenov, D Yu Vasylyev, and B I Lev. Nonclassicality of noisy quantum states. *Journal of Physics B: Atomic, Molecular and Optical Physics*, 39(4):905–916, January 2006.

[111] Th. Richter. A new view on the peřina-mišta form of the glauber-sudershanpfunction. *Journal of Modern Optics*, 48(12):1881–1886, October 2001.

[112] T. Kiesel, W. Vogel, V. Parigi, A. Zavatta, and M. Bellini. Experimental determination of a nonclassical glauber-sudarshanpfunction. *Physical Review A*, 78(2), August 2008.

[113] See Supplemental Material at URL-will-be-inserted-by-publisher for more details.

[114] Kurt Bernardo Wolf. *Integral Transforms in Science and Engineering*. Springer US, Boston, MA, 1979.

[115] Victor Namias. The fractional order fourier transform and its application to quantum mechanics. *IMA Journal of Applied Mathematics*, 25(3):241–265, 1980.

[116] Héctor Moya-Cessa and Peter L. Knight. Series representation of quantum-field quasiprobabilities. *Physical Review A*, 48(3):2479–2481, September 1993.

[117] K. Banaszek, C. Radzewicz, K. Wódkiewicz, and J. S. Krasiński. Direct measurement of the wigner function by photon counting. *Physical Review A*, 60(1):674–677, July 1999.

[118] Kritsana Srakaew, Pascal Weckesser, Simon Hollerith, David Wei, Daniel Adler, Immanuel Bloch, and Johannes Zeiher. A subwavelength atomic array switched by a single rydberg atom. *Nature Physics*, 19(5):714–719, May 2023.

[119] Ephraim Shahmoon, Dominik S. Wild, Mikhail D. Lukin, and Susanne F. Yelin. Cooperative resonances in light scattering from two-dimensional atomic arrays. *Physical Review Letters*, 118(11):113601, March 2017.

[120] Kyle E. Ballantine and Janne Ruostekoski. Cooperative optical wavefront engineering with atomic arrays. *Nanophotonics*, 10(7):1901–1909, May 2021.

[121] C. D. Parmee and J. Ruostekoski. Bistable optical transmission through arrays of atoms in free space. *Physical Review A*, 103(3), March 2021.

[122] K. E. Ballantine, D. Wilkowski, and J. Ruostekoski. Optical magnetism and wavefront control by arrays of strontium atoms. *Physical Review Research*, 4(3), September 2022.

[123] Roni Ben-Maimon, Yakov Solomons, Nir Davidson, Ofer Firstenberg, and Ephraim Shahmoon. Quantum interfaces with multilayered superwavelength atomic arrays. *Physical Review Letters*, 135(3), July 2025.

[124] Shiwen Sun, Yi-Xin Wang, Xiao Liu, and Yan Zhang. Tunable dual-band atomic mirror based on subwavelength atomic arrays under electromagnetically induced transparency, 2025.

[125] Julien Vaneecloo, Sébastien Garcia, and Alexei Ourjoumtsev. Intracavity rydberg superatom for optical quantum engineering: Coherent control, single-shot detection, and optical π phase shift. *Physical Review X*, 12(2), May 2022.

[126] Kanu Sinha, Jennifer Parra-Contreras, Annyun Das, and Pablo Solano. Spontaneous emission in the presence of quantum mirrors. *New Journal of Physics*, 27(5):054101, May 2025.

[127] D E Chang, L Jiang, A V Gorshkov, and H J Kimble. Cavity qed with atomic mirrors. *New Journal of Physics*, 14(6):063003, June 2012.

[128] Darrick E. Chang, Anders S. Sørensen, Eugene A. Demler, and Mikhail D. Lukin. A single-photon transistor using nanoscale surface plasmons. *Nature Physics*, 3(11):807–812, November 2007.

[129] G. Hétet, L. Slodička, M. Hennrich, and R. Blatt. Single atom as a mirror of an optical cavity. *Physical Review Letters*, 107(13):133002, September 2011.

[130] Andreas Reiserer, Stephan Ritter, and Gerhard Rempe. Nondestructive detection of an optical photon. *Science*, 342(6164):1349–1351, December 2013.

[131] Zhang Su-Zhen, Xie Xiao-Tao, and Yang Wen-Xing. Scheme for direct measurement of wigner characteristic function for motion of a single trapped ion. *Communications in Theoretical Physics*, 46(2):306–308, August 2006.

[132] Konrad Banaszek and Kryzysztof Wódkiewicz. Direct probing of quantum phase space by photon counting. *Physical Review Letters*, 76(23):4344–4347, June 1996.

[133] N. W. M. Ritchie, J. G. Story, and Randall G. Hulet. Realization of a measurement of a “weak value”. *Physical Review Letters*, 66(9):1107–1110, March 1991.

[134] A.B. Klimov and S.M. Chumakov. *A Group-Theoretical Approach to Quantum Optics: Models of Atom-Field Interactions*. Wiley, 2009.

[135] David R. A. Ruelas Paredes, Mariano Uria, Eduardo Massoni, and Francisco De Zela. Testing precision and accuracy of weak value measurements in an ibm quantum system. *AVS Quantum Science*, 6(1), January 2024.

[136] Ignacio Salinas Valdivieso, Victor Gondret, Gerd Hartmann S., Mariano Uria, Pablo Solano, and Carla Hermann-Avigliano. Characterization of generalized coherent states through intensity-field correlations. *Phys. Rev. Res.*, 8:023118, May 2026.